

Politecnico di Torino

ScuDo
Scuola di Dottorato ~ Doctoral School
WHAT YOU ARE, TAKES YOU FAR

Doctoral Dissertation
Doctoral Program in Energy Engineering (35^{th}cycle)

Enhanced Multiscale Modeling of Wetting Phenomena on Surfaces with Tailored Properties for Energy Devices

By

Francesco Maria Bellussi

******

Supervisor(s):
Prof. Pietro Asinari, Supervisor
Prof. Matteo Fasano, Co-Supervisor

Doctoral Examination Committee:
Prof. Subramanian Sankaranarayanan, Referee, University of Illinois at Chicago
Prof. Mario Orsi, Referee, University of the West of England
Prof. Manfredo Gherardo Guilizzoni, Politecnico di Milano
Prof. Daniele Marchisio, Politecnico di Torino
Prof. Eliodoro Chiavazzo, Politecnico di Torino

Politecnico di Torino
2023

Declaration

I hereby declare that, the contents and organization of this dissertation constitute my own original work and does not compromise in any way the rights of third parties, including those relating to the security of personal data.

Francesco Maria Bellussi
2023

* This dissertation is presented in partial fulfillment of the requirements for **Ph.D. degree** in the Graduate School of Politecnico di Torino (ScuDo).

To Marghe and Vanni

That was one good thing about Stradlater
You didn't have to explain every goddam little thing with him

J.D. Salinger
The Catcher in the Rye

Acknowledgements

This thesis represents the culmination of my Ph.D. journey at the Department of Energy at Politecnico di Torino. Many people have been a crucial part of this journey, providing both scientific and personal support.

First of all, I would like to extend my gratitude to my supervisors for their indispensable contributions to my academic growth, for their vision, and for having defined the path of this adventure. In particular, Pietro Asinari, who gave me the opportunity to start this Ph.D. with the Small group and supported me in navigating the challenging international academic scene. Matteo Fasano for his patient guidance, balanced teaching approach, and equipping me with the skills to address various academic challenges that arise during a Ph.D. program. Finally, I want to express my gratitude to Eliodoro Chiavazzo for his precious advice and suggestions over the years.

A special acknowledgment is reserved for my mentor, Otello Maria Roscioni, who generously shared his scientific wisdom and his vision of science and research as a social benefit. I am deeply grateful to my silent mentor, friend, and flatmate, Matteo Morciano, who always gave me the right advice, often without saying much, and for all the crazy adventures we have had over the years.

I'm also grateful to all the current and former members of the Small group I had the privilege and pleasure of working with. Special mentions to Paolo De Angelis for our awesome discussions about science, arts, culture, and life, and to Annalisa Cardellini for always being right and having the perfect solution. To Gabriele Falciani for all the calls we have had over the past years, during which we discussed our Ph.D. challenges. I would also like to acknowledge Marina Provenzano and Alessandro Casto, two of the best students I have had the privilege to supervise during their M.Sc. thesis.

During my Ph.D., I had the privilege of working on the European project Oyster[1], which provided me with the valuable opportunity to collaborate with various international groups. A special thanks goes to Prof. Marco Sebastiani and Edoardo Rossi at LIME of the Roma Tre University, Thomas Straub and Mario Schleyer at Fraunhofer Institute for Mechanics of Materials IWM, and Prof. Gleb Sukhorukov and Valeriya Kudryavtseva at the School of Engineering and Materials Science of Queen Mary University of London for their significant contributions to part of the experimental activity aimed at validating the numerical models developed in this thesis.

During my third year, I had the opportunity to spend a significant amount of time at the University of Illinois in Chicago. For my time there I would first like to extend my gratitude to Prof. Constantine M. Megaridis for hosting me at the MNFTL group. His vision and the chance to work in an international environment alongside researchers from various disciplines were invaluable to my development. I would also like to thank Harshad Sanjay Gaikwad for our time together in the lab and exploring the city, and Sreya Sarkar for her contributions to part of the experimental validation activity and for the discussions we had to bridge the gap between experiments and simulations.

During my time there, I had the pleasure of meeting many wonderful people who enriched my experience in the US. Thanks to Giggio, for introducing me to the Italian student community in Chicago, and for our exotic experiences at the 606 while listening to "No Dice" and at Oak Street Beach. Thank you for making me feel like a mentor. To the regaz, for all our climbing adventures: Gimmy, the lover, Andre, the coach, and Matti, the caleb. To the climbing co-op in Marquette for opening the doors of their wonderful house to us. My flatmate Will, with whom I had some unforgettable parties and who shared his interesting view of the US and Europe, and his unique egg-cooking skills. To Tayler, for giving me a taste of real Chicagoan life.

All of this would not have happened without the support from the Fellowship of the Ring, friends of an entire life. Thanks to Cansa, Grad, Bruno, Carletto, Don Fa', Meux, Iacopo, Capoccia, Pier, and Reddino for the enthusiasm we've shared on our journeys, for all the everyday stories, and for inspiring each other to make everything a little bit better. To Silvia B. for her spirit of adventure and for being there during the nerve-wracking first submission of this thesis.

[1]Grant agreement No. 760827

And none of this would have been possible without the patience of my extended family. Thanks for giving me the freedom to find my own path and for trusting me.

And finally, thanks to Clara, who inspired - or maybe tricked - me into embarking on this journey. Thank you for bearing with me throughout this adventure. Thank you for all the things we would not have done without each other. I love you.

Abstract

A challenging topic in surface engineering is predicting the wetting properties of soft interfaces and 2D materials with different liquids. Surfaces with tailored properties find practical applications in the energy sector, including the design of materials for optronic devices, drag reduction for boats, anti-icing for aircraft wings, self-cleaning for solar and photovoltaic panels, and desalination membranes. The ability to predict and control wetting behavior in these materials will enable the development of more efficient and effective surfaces, leading to improvements in energy production, storage, consumption, and thus environmental sustainability. However, a robust and fast computational protocol suitable for predicting wettability with molecular precision is still lacking.

In this thesis, a workflow based on molecular dynamics simulations to predict the wettability of soft surfaces and 2D materials is proposed and tested against the experimental contact angle of several polar and non-polar liquids. The study cases addressed here focus on polymers as soft surfaces and on graphene as 2D material, but the proposed experimental-modeling protocols may have broader fields of application. Structural properties and surface roughness of numerical substrates have been analyzed through microscopy measurements and compared with chemically equivalent experimental samples. Then, the contact angle and interface tension were evaluated reproducing numerically the sessile droplet method, or via a thermodynamics approach, namely the free energy perturbation. The results were finally validated against standardized characterization tests, reaching a good agreement with experimental evidence, and providing insights on possible effects of roughness at the nanoscale, experimental conditions, and graphene wetting semi-transparency.

Overall, this work represents the initial steps towards an integrated multi-scale framework for predicting the wettability of more complex interfaces, which will

eventually take into account the effect of surface topology at higher scales and synergically be employed with experimental characterization techniques.

With this in mind, a coarse-grained model for water and polymers with atomistic accuracy to speed up mesoscopic simulations is proposed. Such a model will be useful to describe interfaces with characteristic dimensions typically larger than the ones exploitable with classical molecular dynamics. Indeed, atomistic simulations are constrained by the feasible computational capacity but calibrated coarse-grained (CG) models can go beyond these limits. First, three popular atomistic water models are compared with their corresponding CG models built using finite-size particles such as ellipsoids.

Similarly, the coarse-grained model of PLGA is compared with its corresponding atomistic model, where every polymer residual is described by only one bead. Differently from previous approaches, short-range interactions are accounted for with the generalized Gay-Berne potential, while electrostatics and long-range interactions are computed from virtual charges inside the ellipsoids. Such an approach leads to a quantitative agreement between the original atomistic models and their CG counterparts. Results show that a timestep up to 10 fs can be achieved to integrate the equations of motion without significant degradation of the physical observables extracted from the computed trajectories, thus unlocking a significant acceleration (up to six times with respect to the atomistic counterparts) of mesoscopic simulations at given accuracy.

Still, in the context of a multiscale framework, this study demonstrates how the outcomes derived from atomistic and mesoscopic simulations can be effectively utilized in multiphase numerical experiments that rely on finite element simulations.

Publications

Part of the work contained in this dissertation was also previously published in the following articles:

1. Bellussi, F. M., Roscioni, O. M., Ricci, M., & Fasano, M. (2021). Anisotropic electrostatic interactions in coarse-grained water models to enhance the accuracy and speed-up factor of mesoscopic simulations. *The Journal of Physical Chemistry B*, 125(43), 12020-12027.

2. Bellussi, F. M., Roscioni, O. M., Rossi, E., Cardellini, A., Provenzano, M., Persichetti, L., Kudryavtseva, V., Sukhorukov, G., Asinari, P., Sebastiani, and M. Fasano, M. (2022). Wettability of soft PLGA surfaces predicted by experimentally augmented atomistic models. *MRS Bulletin*, 48:108–117, 2022

The following articles were published as part of the Ph.D. activity but were not included in this dissertation:

1. Nejad, S. M., Srivastava, R., Bellussi, F. M., Thielemann, H. C., Asinari, P., and Fasano, M. (2021). Nanoscale thermal properties of carbon nanotubes/epoxy composites by atomistic simulations. *International Journal of Thermal Sciences*, 159, 106588.

2. Bellussi, F. M., Sáenz Ezquerro, C., Laspalas, M., & Chiminelli, A. (2021). Effects of graphene oxidation on interaction energy and interfacial thermal conductivity of polymer nanocomposite: A molecular dynamics approach. *Nanomaterials*, 11(7), 1709.

3. Cardellini, A., Bellussi, F. M., Rossi, E., Chiavarini, L., Becker, C., Cant, D., Asinari, P., and Sebastiani, M. (2021). Integrated molecular dynamics

and experimental approach to characterize low-free-energy perfluoro-decyl-acrylate (PFDA) coated silicon. *Materials & Design*, 208, 109902.

4. Diego, M., Gandolfi, M., Casto, A., Bellussi, F. M., Vialla, F., Crut, A., Roddaro, S., Fasano, M., Vallée, F., Del Fatti, N., Maioli, P., and Banfi, F. (2022). Ultrafast nano generation of acoustic waves in water via a single carbon nanotube. *Photoacoustics*, 28, 100407.

5. Sarkar, S., Gukeh, M. J., Roy, T., Gaikwad, H., Bellussi, F. M., Moitra, S., and Megaridis, C. M. (2023). A new methodology for measuring solid/liquid interfacial energy. *Journal of Colloid and Interface Science*, 633, 800-807.

6. Casto, A., Bellussi, F. M., Diego, M., Del Fatti, N., Banfi, F., Maioli, P., and Fasano, M. (2023). Water filling in carbon nanotubes with different wettability and implications on nanotube/water heat transfer via atomistic simulations. *International Journal of Heat and Mass Transfer*, 205, 123868.

7. Provenzano, M., Bellussi, F, M., Morciano, M., Rossi, E., Schleyer, M., Asinari, P., Straub, T., Sebastiani, M., and Fasano, M. (2023). Experimentally validated phase-field model to design the wettability of micro-structured surfaces. *Materials & Design*, 112042, 2023.

Contents

1 Introduction **1**

1.1 Why wetting 1

1.2 Context 4

1.2.1 Atomistic simulations of interfaces 5

1.2.2 Mesoscopic simulations: coarse-graining models of water and PLGA 9

1.3 Purpose and structure of this thesis 12

2 Theoretical background **17**

2.1 Physics of wetting 17

2.1.1 Interface tension 17

2.1.2 Young-Laplace equation 18

2.1.3 Contact angle 19

2.1.4 Capillary length 21

2.1.5 Wetting on rough surfaces 21

2.2 Experimental approaches for surface design and characterization . . 23

2.2.1 Surface structure and composition 24

2.2.2 Wetting experiments 25

2.3 Numerical approaches for surface design and characterization . . . 27

2.3.1 Molecular dynamics 28

2.3.2 Force field . . . 28
2.3.3 Ensemble . . . 32
2.3.4 Time integration . . . 33
2.3.5 Free energy perturbation methods for interface properties . . 34
2.3.6 Irving-Kirkwood relation for interface tension . . . 36
2.3.7 Coarse-grained molecular dynamics . . . 37

3 Experimentally-augmented atomistic models for PLGA surfaces 43
3.1 Materials and methods . . . 44
3.1.1 Model building . . . 44
3.1.2 Sample preparation . . . 48
3.1.3 Experimental characterisation . . . 48
3.2 Results and discussion . . . 49
3.2.1 Validation of the force field . . . 50
3.2.2 Surface topography characterization . . . 51
3.2.3 Wettability of PLGA surfaces . . . 54
3.2.4 Discussion . . . 64
3.3 Further perspectives . . . 65

4 Wettability of graphene surfaces predicted by the free energy perturbation 67
4.1 Materials and methods . . . 68
4.1.1 Model building . . . 68
4.1.2 Evaluation of the water surface tension γ_{lv} and solid-liquid interface tension γ_{sl} . . . 71
4.1.3 Evaluation of work of adhesion (W_{ad}) . . . 72
4.1.4 Friction coefficient and slip length . . . 72
4.2 Results and discussion . . . 74

4.2.1 Surface tension of water 74
4.2.2 Single-layer graphene 75
4.2.3 Multi-layer graphene and experimental validation 78
4.2.4 Friction coefficient 82
4.3 Further perspectives 82

5 Coarse-grained water models with enhanced accuracy and speed-up factor 85

5.1 Computational methods 86
5.1.1 Model building 87
5.1.2 Dynamic viscosity 90
5.1.3 Self-diffusion coefficient 90
5.1.4 Surface tension 91
5.1.5 Enthalpy of vaporisation 91
5.2 Results and discussion 92
5.2.1 System structure 92
5.2.2 Self-diffusion coefficient, dynamic viscosity, and surface free energy 92
5.2.3 Timestep effect 98
5.2.4 Enthalpy of vaporisation 100
5.2.5 Wall time ration and speed-up factor 100
5.3 Further perspectives 102

6 Coarse-grained polymers models: the case study of PLGA 105

6.1 Computational methods 107
6.1.1 Model building 107
6.1.2 Evaluation of the PLGA thermal conductivity 110
6.1.3 Evaluation of the PLGA elastic properties 111

6.2 Results and discussion . . . 113
6.2.1 Density and glass transition temperature . . . 113
6.2.2 Thermal conductivity . . . 114
6.2.3 Elastic properties . . . 117
6.3 Coupled water/PLGA CG model . . . 118
6.4 Further perspectives . . . 118

7 Conclusion and perspectives **123**

Appendix A LAMMPS codes **129**
A.1 Experimentally-augmented atomistic models for PLGA surfaces . . 130
A.1.1 MD PLGA/water sessile experiment . . . 130
A.2 Wettability of graphene surfaces predicted by the free energy perturbation . . . 133
A.2.1 Interface tension γ_{sl} . . . 133
A.2.2 Work of adhesion W_{ad} . . . 138
A.3 Coarse-grained water models with enhanced accuracy and speed-up factor . . . 140
A.3.1 Typical CG run with MOLC . . . 140
A.4 Coarse-grained polymers models: the case study of PLGA . . . 145
A.4.1 Thermal conductivity . . . 145
A.4.2 Elastic properties . . . 152

Nomenclature **155**

List of Figures **159**

List of Tables **163**

References **165**

Chapter 1

Introduction[1]

1.1 Why wetting

The physical process that describes the capability of a surface to either attract or repel liquids is known as wettability. Controlling the wetting properties of certain materials would enable the development of more efficient and effective surfaces, leading to improvements in energy production and storage, healthcare, and environmental sustainability. Specific applications in the energy sector include the design of materials for optronic devices [3], drag reduction for boats [4], anti-icing for aircraft wings [5], self-cleaning for solar and photovoltaic panels [6], medical membranes [7], and desalination membranes [8].

Given the significant industry interest, scientists and engineers design materials with specific wettability characteristics by manipulating their chemical and physical properties. The design process is generally inspired by nature, which provides a wide variety of adaptive surfaces to achieve specific wetting properties [9, 10]. One of the most cited examples is represented by the lotus effect observed in the leaves of the lotus plant, which possesses superhydrophobic properties [11, 12]. The surface of the lotus leaves is covered with micro- and nano-structures that create a rough surface, reducing the contact area between water droplets and the surface. This results in a high contact angle and low contact angle hysteresis, causing water droplets to roll off the surface, carrying away dirt and debris. Various approaches investigate how to reproduce the lotus effect to optimize the surface structure of materials

[1] Part of the work included in this chapter was previously published by Bellussi *et al.* in [1, 2]

through experimental and numerical methods [13, 14]. Potential applications of self-cleaning surfaces involve also the energy transition. For example, the efficiency of photovoltaic solar systems depends on the cleanness of their panels, and thus a self-cleaning surface would improve their energetic performance [15, 16]. Similar to lotus leaves, other plant leaves, animal skins, insect legs, or wings exhibit peculiar wetting behaviors. For example, the rose petal effect refers to the ability of rose petals to resist water because of their surface nano-roughness, which prevents water droplets from sticking to the surface. This effect has inspired the development of anti-fog and anti-icing coatings for various applications, such as car windshields and airplane wings [17]. The gecko effect refers to the ability of geckos to adhere to surfaces through van der Waals forces. Geckos possess a hierarchical structure on the undersides of their feet, which enables them to attach to surfaces by maximizing the contact area for adhesion. This phenomenon has served as inspiration for the creation of novel adhesives intended for applications in robotics and medical devices. [18, 19]. The shark skin effect is the ability of shark skin to reduce drag in the water. The skin of sharks is covered by micro-structures called denticles, which reduce turbulence and drag as water flows over the surface [20]. This effect has inspired the development of new types of coatings for boats and submarines, with the potential to reduce fuel consumption and increase speed.

When it comes to creating surfaces with tailored properties, scientists consider molecular structure and surface morphology. For example, thin polymeric films can be adopted to tune the wetting properties of materials, or to create bio-degradable membranes [21, 22]. Instead, a common practice to create super-hydrophobic materials is to adopt a hierarchical structure onto the surface [14]. This approach is also employed to design hydrophobic surfaces using inherently hydrophilic materials [23]. Structured surfaces can also be used to induce or enhance the hydrophilicity of some materials like in wastewater remediation [24], water harvesting [25], dropwise condensation [26] or distillation processes [27]. In other cases, 2D materials like graphene or graphene oxide are being recently implemented as desalination membranes, due to their specific molecular structure and electronic distribution [28–31].

However, the surface structure and topography of structured materials, soft polymers, and 2D materials can be highly irregular, and the mechanical properties of the surface can vary widely, leading to non-uniform wetting behavior. Consequently, predicting the wetting properties of these materials is a complex and challenging task

that requires the definition of a multi-scale numerical model to assist experiments and guide the materials' prototyping and development, but a standardized and rational protocol has not been implemented yet.

At the theoretical level, the commonly adopted Young equation [32, 33], which describes the macroscopic contact angle as a function of surface energies of surface and liquid phases in contact, is valid exclusively for uniform flat materials. In these cases, the surface energies depend only on the chemistry of materials. However, real surfaces can present irregularities and non-uniformity that can affect their response to liquids. Such irregularities can arise from different length scales, due to non-uniform morphologies at the nano-, micro-, and macro-scale, as the previously cited examples in nature demonstrate. As a consequence, micro- and nano-scale behaviors of surfaces can sensibly affect the overall estimation of wetting phenomena at the macro-scale, i.e., contact angle and fluid flow on the surface. Such peculiar characteristics of wetting phenomena led researchers to develop materials with nano- and micro-scale, or hierarchical structures [13, 14].

The widely used analytical theories for the hydrophilic and hydrophobic regimes, namely Wenzel [34] and Cassie-Baxter [35], cannot describe a wide range of intermediate and metastable states, so a thorough understanding of the combined chemical and morphological effect on surface wettability remains unresolved. Numerical models for predicting the wetting behavior of soft polymers and 2D materials are often oversimplified and lack the necessary detail to provide accurate predictions. Polymer surfaces are often treated as rigid substrates, thereby neglecting possible deformations of the interface [36–38]. In the case of graphene, the characterization of its interface with water is typically limited to the evaluation of a single parameter (i.e., work of adhesion or interface tension), while relying on other experimental data that may be influenced by experimental conditions [39, 40]. More detailed approaches, instead, such as density functional theory (DFT), can be computationally expensive, imposing limitations on the number of atoms that can be included in the simulation setup, typically to a few thousand atoms [41]. This constraint makes them impractical for use in a design setting.

Consequently, the combination of all of these factors generally leads to adopting protocols based on a trial-and-error experimental approach. Furthermore, due to the nature of these phenomena that involve different scales, there is a significant

need for an enhanced multi-scale model that can provide accurate predictions while remaining computationally feasible.

1.2 Context

The aim of this Ph.D. thesis is to develop an enhanced multi-scale model to provide a detailed and comprehensive picture of wetting phenomena, guiding a rational process for designing surfaces with tailored properties. This section introduces the constitutive parts of the multi-scale model proposed, highlighting also how it can enhance the quality and the speed of the numerical simulations adopted to predict wetting phenomena on soft surfaces and 2D materials.

Specifically, in section 1.2.1 we introduce the works developed at the atomistic level through molecular dynamics simulations to evaluate the wettability and interface properties of liquid-solid interfaces, that represent the first steps of the multi-scale framework object of this thesis. In this perspective, the results of the associated works, which will be presented and discussed in Chapters 3 and 4, in terms of static contact angle, work of adhesion, interface tension, and friction coefficient, not only provide a characterization of the interfaces studied, but can also be adopted to guide the development of mesoscopic models, or as boundary conditions for continuum models.

In section 1.2.2, we introduce the works developed for the definition and validation of a mesoscopic model based on coarse-grained molecular dynamics. The results of these activities, presented and discussed in Chapters 5 and 6, are used to validate the model proposed in terms of bulk and interface properties of each solid and liquid phase proposed. On one hand, this validation is required to test the reliability of the models presented. On the other hand, the properties of each single phase can affect the interface characteristics of the two phases in contact. As an example, it is possible to mention the surface tension of the probe liquid and the elastic stiffness of the wetted substrate. At the end of Chapter 6 we will report some initial results obtained by coupling the two coarse-grained models developed, in terms of wettability properties. Finally in Chapter 7, we recall also some perspectives for the implementation of continuum simulations that can take molecular dynamics results as input boundary conditions.

1.2.1 Atomistic simulations of interfaces

In this subsection, we first discuss the significance of atomistic simulations in describing soft polymer interfaces, emphasizing their importance in achieving a comprehensive understanding of their properties. Next, we address the relevance of these simulations in characterizing graphene-water interfaces, considering the challenges faced by the scientific community in studying such interfaces. Finally, we highlight the capability of these simulations to guide the development of mesoscopic models and to provide a comprehensive set of boundary conditions for continuum problems aimed at describing the wettability properties of structured surfaces or dynamic fluid flows.

Soft interfaces

The study of soft interfaces is an attractive topic for scientists and engineers due to the broad range of industrial applications dependent on surface properties, such as energy-savings films [42], anti-bacterial coatings [43], biodegradable scaffolding for tissue regeneration [7, 44], rheological and mechanical control [45, 46], phase-separation membranes and interfaces [47–49], and polymer sensors [50].

From an experimental standpoint, different techniques have been used to characterize soft surfaces, giving an insight into their chemical, physical, structural, and topological properties. Spectroscopy analysis is commonly used to highlight the molecular composition [51, 52], electronic microscopy [53] and scanning probe microscopy [54] to analyze the topology, while contact angle (CA) measurement [55] to quantify the surface free energy (SFE, using Girifalco or Owens-Wendt models [56–58]). Moreover, recent developments in contact-mechanics-based protocols have been proposed as an alternative means to investigate SFE at the micro-scale via the Johnson-Kendall-Roberts (JKR) or Dergiaguin-Muller-Toporov (DMT) models [59]. However, the principal limitation of experimental characterization alone is the lengthy trial-and-error approach, which involves looping over the cycle of materials design, production, and analysis, thus extending the time of prototyping and, consequently, commercialization [60]. In this scenario, computational experiments can help to predict the role played by the chemical and topological characteristics on the effective properties of soft interfaces across multiple scales, therefore providing a rational design of their composition and structure according to the required target

performance [61, 62]. Given the time and space scales involved in wetting phenomena [63], the adopted computational methods must include a combination of models spanning from the continuum to the atomistic scale.

Since the pioneering study of Young [32], several continuum models have been proposed to describe the dependence of the static contact angle and dynamical wetting process with surface morphology. Generally, the CA of a liquid on a surface can be correlated to the surface tension components solid/gas (γ_{sg}), solid/liquid (γ_{sl}), and liquid/gas (γ_{lg}), through the Young equation [33]:

$$\gamma_{\mathrm{sg}} = \gamma_{\mathrm{sl}} + \gamma_{\mathrm{lg}} \cos\theta_{\mathrm{Y}}, \tag{1.1}$$

where θ_Y is the Young CA, which depends only on the chemistry of the liquid and solid phases. Despite its simplicity, this relation is valid only for ideal flat surfaces. The CA obtained experimentally corresponds to the apparent CA, which depends also on the surface roughness and morphology. According to the Wenzel and Cassie-Baxter models of static contact angle on rough surfaces [34, 35, 33], the Young or local contact angle can be included in continuum models as a boundary condition on the wetted wall. This value depends on the surface chemistry of the material, and it can be provided by experiments performed on a perfectly flat surface or – as highlighted in the work of Johansson *et al.* [64, 65] – by molecular dynamics (MD) simulations.

At the atomistic level, an increasing number of studies have focused on wettability. Leroy *et al.* used the free energy perturbation approach (FEP) [66, 67] to evaluate the CA of water on graphene and, consequently, to calibrate their interaction parameters. Similarly, Zhang *et al.* [68] employed the FEP to parametrize the interaction of water with fresh and aged molybdenum disulfide (MoS_2) surfaces, while Rajan *et al.* [69] used the FEP and the Green-Kubo relation to evaluate the work of adhesion and friction coefficient of water and other solvents on a hexagonal boron nitride surface. In our work [70], we highlighted that a synergistic use of MD simulations and experiments allows discriminating how surface chemistry and topology of a hydrophobic coating contribute to increasing the contact angle of water. The CA assessment by MD can be carried out also *via* the droplet method, where a liquid drop is positioned above the tested surface and then left to relax until equilibrium conditions are reached. Using this method, Yaghoubi *et al.* and Koishi *et al.* [71–73] studied the effect of roughness on the wettability of graphite surfaces, while Sresht *et*

al. assessed MoS_2 surfaces [74]. In such simulations, the solid substrate is typically modeled as a rigid crystal, thus neglecting deformation effects at the solid-liquid interface. Similarly, Liu *et al.* [36], Zhu *et al.* [37] and Etha *et al.* [38] applied the droplet method to soft surfaces, keeping the substrate rigid to preserve the planar configuration of the interface. However, in the case of soft surfaces such as polymers, the interfacial deformation of the solid substrate and its effect on wettability cannot be neglected to accurately reproduce the actual experimental conditions. Hence, the characteristic deformable boundary of soft interfaces requires new (and validated) 3D simulations and post-processing protocols for the CA measurement by MD, especially for the definition of the mean plane where the contact angle is evaluated.

Graphene/water interface

During the last two decades after its discovery [75, 76], graphene has attracted the interest of universities and industries due to its peculiar mechanical, thermal, and electronic properties [77]. Due to these characteristics, graphene finds applications in several industrial sectors, adopted as semi-conductor in electronic transistors [78, 79], reinforcement in polymer-based nanocomposites [80, 81], or in the specific energy sector as solar energy conversion and electrochemical energy storage [82, 83]. Graphene layers have also been studied and adopted as membranes for reverse osmosis processes for water desalination [28–31], a phenomenon which is also intensively investigated through MD simulations [84–86].

Water transport phenomena in nano-channels strongly depend on the wetting properties of the surfaces involved. However, despite the efforts spent both at the experimental and numerical level to characterize graphene surfaces, its wetting properties still constitute a strong debate in the scientific community [87, 88], mainly due to the difficulty of handling 2D materials. Furthermore, several environmental conditions or sample preparation procedures can affect the final measure of water CA on graphene, which has been reported in the range 45° - 127° [87].

Generally, at the experimental level, graphene is deposited onto solid substrates. In this case, it is usually mentioned as supported graphene [87, 89]. These experimental campaigns highlighted the possible non-transparency of graphene with respect to the substrate [89–91], which has been also investigated with numerical approaches [90, 92]. On the other hand, other studies demonstrated a negligible effect of the substrate with respect to the surface properties of graphene [93, 94]. Other recent

experiments adopted free-standing graphene to avoid possible effects of the substrate on surface properties. In this other case, the material is commonly tested through the captive bubble method [95] to investigate the water contact angle. However, graphene wettability results to be strongly sensitive to the ambient atmosphere, attracting airborne contaminants that may affect the final measurement of contact angle through the sessile droplet experiment [96].

MD simulations have been commonly adopted to predict the static contact angle of water and to help and assist experiments when nano-structured solid-liquid interfaces are involved. In the work of Werder *et al.* [97], the authors explore several interatomic potentials, trying to find the best representation of the sessile droplet experiment on graphene, ranging from hydrophilic (CA around 40°) to hydrophobic (CA around 130°) configurations. Yaghoubi *et al.* [72] adopted again the sessile droplet numerical experiment to investigate the effects of nanoroughness on graphene surfaces. In their seminal paper, instead, Leroy *et al.* proposed to investigate the work of adhesion W_{ad} through the free energy perturbation approach [67]. Such a method resulted to be less sensitive than the droplet method to the water model adopted, making the W_{ad} a good candidate to be compared with the experimental results. More recently, Dreher *et al.* [39] adopted again the free energy perturbation approach to quantify the solid-liquid interface tension between water and graphene. Similarly, Chiricotto *et al.* [40] evaluated the water/graphene interface tension using the mechanical route, namely the Irvine-Kirkwood relation. However, the characterization of graphene/water is typically limited to the evaluation of a single parameter (i.e., work of adhesion or interface tension), while relying on other experimental data that may be influenced by experimental conditions. Therefore, despite the intense efforts spent, the problem of graphene wettability remains unresolved, and a validated MD model to characterize the wetting properties of graphene, that can be integrated with continuum simulations, is still lacking.

Transition to higher scales

In the context of an enhanced integrated multi-scale model, the quantification of both W_{ad} and γ_{sl} between two phases in contact, as well as certain bulk and interface properties such as γ_{lg} for probe liquids, thermal conductivity, and elastic moduli for substrates, can be valuable for the development of coarse-graining and continuum models. In the former case, such results can aid in the validation and eventually the

refinement of the model parametrization. In the latter, W_{ad} and γ_{sl} can be adopted as boundary conditions within a multi-phase model [98–101]. Indeed, these quantities are related to the static and dynamic contact angle (CA) through the Young-Duprée and Makkonen relations [102, 103]. MD simulations can also be used to estimate the friction coefficient and, consequently, the slip length. The slip length is a crucial parameter for defining the generalized Navier boundary conditions (GNBC) [104, 105], that, together W_{ad} and γ_{sl}, contribute to establishing a comprehensive set of boundary conditions.

1.2.2 Mesoscopic simulations: coarse-graining models of water and PLGA

In this second subsection, we discuss the importance of the development of a mesoscopic model able to characterize interface properties with good accuracy while limiting the computational cost. The relevance of such an approach is justified considering the multi-scale nature of interface phenomena, that depend on both the chemistry and the presence of roughness or structures. For this reason, on one hand, it is required a high level of chemical detail than can be provided by atomistic simulations, as already discussed in the previous subsection 1.2.1; on the other hand, enhanced and accelerated simulations are required to implement larger models that allow the study of possible effects of structures or roughness, as well as link directly discrete and continuum description of interfaces. In this perspective, we discuss the relevance of implementing an enhanced coarse-graining model, taking as a study case the PLGA-water interface.

However, due to the large number of atoms involved, polymer modeling at the atomistic level can be challenging and computationally expensive. Despite the accuracy of atomistic MD simulations, and the computational power available nowadays, the typical simulation cell computationally feasible can reach at most a few tens of nm, remaining lower than the typical polymer chain length experimentally observable. Furthermore, atomistic MD simulations are constrained in terms of timescale up to hundreds of nanoseconds, still shorter than the characteristic timescale for several structural and dynamic properties of polymers materials, e.g., polymer diffusion or stress relaxation [106, 107].

In the case of wetting properties evaluation, MD simulations limit the dimension of the free surface and thus the dimension of the droplet which remains confined at the nano level. An elegant way to partly overcome this limitation is to adopt a pseudo-2D model, as previously done by Johansson *et al.* [64] in their numerical work, where they coupled the continuum and atomistic scale of droplet dynamics phenomena. However, in a pseudo-2D model, the spherical shape of a droplet would be replaced by a periodic cylinder, still limiting the accuracy of the protocol. Furthermore, the limited time scales exploitable with MD simulations, at most of the hundreds of ns, would not guarantee to be out of possible metastable states.

In the last few years, Coarse-grained (CG) molecular dynamics (MD) has become increasingly popular in materials science [106, 107] and computational biology [108]. CG simulations offer an efficient way to study the most diverse systems at the mesoscopic scale, with applications ranging from biochemistry [109, 110] to material science [111–113]. The basic idea behind CG is to decrease the number of interacting sites describing individual molecules. By reducing the model resolution, the computational cost and the configuration space of the system decrease, thus enabling the modeling of larger and more complex systems compared to atomistic simulations. For some phenomena, such as the conformation change of enzymes and functional proteins [114, 115], the limiting factor of all-atoms (AA) simulations is the timescale needed to witness a specific process. In this regard, CG models enable longer timesteps and thus accessible simulation times, by suppressing the high-frequency motions characteristic of light atoms and/or averaging out some intra-molecular degrees of freedom.

During the last two decades, several CG models have been proposed to perform accelerated MD simulations. Differences between models generally depend on the methods adopted for the parameterization process, like bottom-up or top-down methods, when properties of higher resolution models (e.g., atomistic models) are used to parametrize CG models or experimental data observed on larger scales are used to tune CG parameters, respectively [107, 116, 117]. One of the most cited and adopted examples of a CG model that uses a hybrid bottom-up and top-down approach is the Martini force field [118], originally developed for lipids [119] and proteins [120], water [121], and then generally extended to materials science [122]. Further models for water [123–125] and polymers [126–129] have been developed for specific study cases. More recently, further efforts have been spent in the field of machine learning coarse graining force fields [127]. Several groups developed

methods to parameterize CG potentials [130, 131] applied to water [132], materials science, and biological systems [127, 133].

However, current CG models often do not provide an adequate description of inter-molecular interactions due to the lack of many-body contributions, which are particularly important for the accurate description of, for example, water properties [134], and interface properties.

Thanks to the recent implementations in software like LAMMPS [135, 136] also assisted by software like Moltemplate [137], aspherical finite-size particles are being used for mesoscopic simulations [138–140]. In this context, and thanks to its internal structure and properties, the CG model named MOLC [138] represents a good candidate for the development of a CG representation of liquids and polymers with atomistic-like accuracy. In the MOLC model, particles can represent single small molecules, like in the case of liquids, or portions of molecules, like polymer residues.

In the specific case of water, for instance, we use one site to represent the whole molecule, but with the possibility to host an arbitrary number of virtual charges to account for realistic electrostatic interactions. Other one-site water models were described in the literature, e.g., using a Stillinger-Weber potential to mimic the effect of anisotropic hydrogen-bonding interactions [141], projecting the many-body interactions into pairwise basis sets [142], or accounting for electrostatic interactions with a point dipole [123], even if significant discrepancies with AA models have been shown. However, many biological processes such as electropore formation in membranes are governed by electrostatic interactions, and thus more detailed modeling of electrostatics is required to capture the dynamic behavior of water [143]. The solution provided by the MOLC model, instead, is to adopt CG beads governed by the generalized Gay-Berne potential [144] and decorated with massless point charges. In detail, each water molecule - and more in general each liquid molecule or polymer residue - explicitly includes three virtual charges, having a 1-to-1 correspondence between the CG model and the source AA model. Hence, the first aim of such an approach is to test that atomistic models of water can be rewritten in terms of finite-size spheres or ellipsoids (thus taking advantage of the longer timesteps allowed by the Richardson iteration method [145]), without significant losing the accuracy of all-atoms description for structural and dynamical properties of liquids. Similarly, in the following Chapter 6, we will test if AA models of

polymers, like the one proposed in Chapter 3, can be rewritten in terms of chains of CG bead.

In addition, the intrinsic characteristics of the model not only provide an effective description of molecules, yielding accurate predictions of properties but also enables the mapping of the coarse-grained (CG) trajectory back to the corresponding AA representation. Consequently, it offers the flexibility to transition between CG and AA representations and vice-versa, depending on the desired level of simulation detail.

1.3 Purpose and structure of this thesis

The model proposed in this thesis is based on the integration between atomistic, coarse-grained, and continuum simulations. In Fig. 1.1 we describe the workflow followed to implement the multi-scale model, as well as the structure of this thesis. The atomistic model takes experimental parameters, such as material composition and surface structures, as inputs and uses them to predict wetting parameters such as contact angle, surface free energy, and interface free energy as outputs. The resulting parameters can then be used to guide the development of mesoscopic models based on coarse-grained molecular simulations or as boundary conditions for continuum simulations. Coarse-grained simulations can enhance the speed of molecular simulations and eventually evaluate the possible effects of nano- or micro-roughness on surfaces. Similarly, continuum simulations can assist in the design of structured surfaces with tuned properties. The proposed model will be finally validated using experimental data to ensure its accuracy and reliability. Overall, this work makes a significant contribution to the field of surface science proposing a more accurate model that provides a detailed and comprehensive picture of wetting phenomena, while still being computationally feasible for use in a design setting.

Part of the research activity carried out has received funding from the European project Oyster[2], which aims to bridge adhesion data at multiple length scales and connect interfacial adhesion with physicochemical properties. It also seeks to inte-

[2]Union's Horizon Research and Innovation Programme under grant agreement No. 760827 (OYSTER: Open characterization and modeling environment to drive innovation in advanced nano-architectured and bio-inspired hard/soft interfaces)

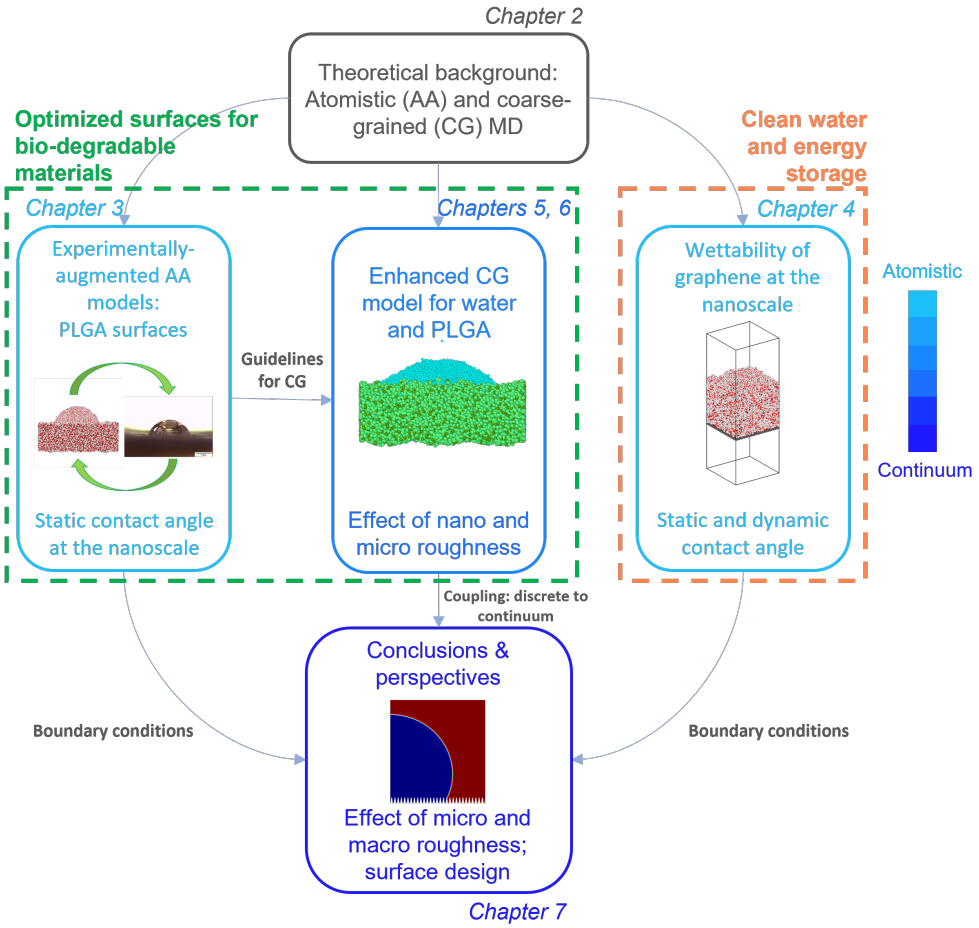

Fig. 1.1 Flowchart representing the organization of this thesis, highlighting the workflow followed to develop the multi-scale model, potential industrial applications, and the main outcomes obtained throughout the thesis.

grate modeling, experimental characterization, and manufacturing within the broader context of industrial exploitation.

The thesis is organized as follows:

- **Chapter 1** - In this Chapter, we explore the motivation behind the development of an integrated multi-scale framework presented in this thesis. Specifically, we examine wetting phenomena in nature and explain how the optimized design of surfaces can facilitate the creation of materials with customized properties for various industrial applications, such as energy, environmental, and biomedical sectors. Additionally, we address the limitations associated

with current surface characterization methods and discuss how our numerical methodology can be seamlessly integrated with experimental approaches.

- **Chapter 2** - In this Chapter, we provide an overview of the theoretical background behind the methods employed for experimental and numerical implementation. Firstly, we delve into the physics of wetting, describing the fundamental principles involved. Following that, we present the experimental methodologies employed to validate the numerical model developed in this thesis. Lastly, we describe the molecular dynamics simulations utilized, encompassing both the AA and CG levels.

- **Chapter 3** - In this chapter, we outline the atomistic model developed to characterize soft polymeric PLGA surfaces. Our focus lies in proposing a numerical protocol that enables the evaluation of the static contact angle, taking into account deformations at the fluid-solid interface. To validate our model, we compare the obtained results with experimental data.

- **Chapter 4** - In this chapter, we present the atomistic model developed for the characterization of graphene-water interfaces. Specifically, we present a numerical protocol, based on thermodynamics principles, that enables the evaluation of adhesion and interface properties, including static and dynamic contact angles. To validate our model, we compare the obtained results with experimental data.

- **Chapter 5** - In this chapter, we outline the development of a new CG representation for classical AA water models, aimed at improving both accuracy and computational efficiency in mesoscopic simulations. The model is extensively tested, evaluating various bulk properties such as density, viscosity, and self-diffusion coefficient of water. Furthermore, we investigate the model's capability to accurately capture interfacial properties, specifically interface tension, which is crucial for describing wetting phenomena at surfaces.

- **Chapter 6** - In this chapter, we present the development of a new CG polymer model designed to be coupled with the aforementioned CG water model. The focus is on investigating bulk properties, such as elastic and thermal properties, of PLGA that are relevant for describing wetting phenomena at surfaces. Additionally, we demonstrate how the CG models of PLGA and water can be

effectively combined to reproduce sessile droplet experiments, significantly accelerating molecular simulations.

- **Chapter 7** - In this chapter, we provide a summary of the main findings from our research, highlighting their significance. Additionally, we outline potential future directions for further investigation to expand upon the current work. We also discuss the possible implications of our research in relevant fields. As a perspective, we present results obtained through continuum simulations, which utilize the results from both AA and CG simulations as boundary conditions.

- **Appendix** - In this Appendix, we present several examples of the codes developed for MD simulations. These codes have been or will be made accessible on Zenodo repositories, ensuring their availability and for simulations reproducibility[3].

[3]Simulations of Chapter 3: https://doi.org/10.5281/zenodo.6629427; simulations of Chapter 5: https://doi.org/10.5281/zenodo.5552351. Simulations of Chapters 4 and 6: all the data will be available after publication of the associated papers.

Chapter 2

Theoretical background[1]

This Chapter provides the theoretical background for the works proposed and developed in this thesis. Firstly, fundamental concepts in the physics of wetting, as well as commonly used experimental and computational techniques for quantifying parameters relevant to wetting phenomena are reviewed. Subsequently, the numerical methods employed in the development of the multi-scale model object of this thesis are discussed.

2.1 Physics of wetting

The pioneering work of Young [32] laid the foundation for contemporary investigations on wettability, establishing a correlation between the shape of a liquid droplet on a solid substrate and the interface energies of the two materials. In the following subsections, we outline some basic concepts useful to describe the physics of wetting.

2.1.1 Interface tension

When dealing with two immiscible phases that are in contact - whether they are solids, fluids, or gases - the interface tension (γ) is the first fundamental concept to consider. Interface tension measures the cohesive force between molecules at

[1] Part of the work included in this chapter was previously published by Bellussi *et al.* in [1, 2]

the boundary of a phase in contact with another phase, reflecting intermolecular interactions. In the case of a liquid phase in contact with a gas or vapor, the interface tension is commonly referred to as surface tension (γ_{lg} or γ_{lv}, respectively), while for solid-gas or solid-vapor contact, it is commonly referred to as surface free energy (γ_{sg} or γ_{sv}, respectively).

From an energetic standpoint, interface tension (γ) represents the excess energy stored at the interface. It can be defined in terms of Helmotz free energy variation (∂F) due to the variation of the interface area (∂A) while maintaining constant volume (V), temperature (T), and the number of particles (N):

$$\gamma = \left(\frac{\partial F}{\partial A}\right)_{NVT}. \tag{2.1}$$

Similarly, it can be defined considering the Gibbs free energy variation (∂G) due to the variation of the interface area, while maintaining constant pressure (P), temperature, and number of particles:

$$\gamma = \left(\frac{\partial G}{\partial A}\right)_{NPT}. \tag{2.2}$$

From a mechanical perspective, interface tension (γ) represents a force per unit length that acts parallel to the boundary between two phases. The molecules at the interface experience an energetically unfavorable condition compared to molecules in the bulk due to the presence of fewer neighboring molecules of the same species at the boundary. In the case of a liquid-gas interface, for instance, the formation of a spherical droplet or bubble is due to the minimization of the interface area between the two species to minimize the excess of energy.

2.1.2 Young-Laplace equation

The pressure difference resulting from the presence of an interface can be expressed by the Young-Laplace equation [146, 147]. Let us consider an infinitesimal portion of the interface, denoted by the interface area $A = \delta x \delta y$, and an infinitesimal dilatation of the interface along the normal direction, denoted by δz. The local radii of curvature R_i ($i = 1,2$) and A increase by δz, and $\delta A \approx (\frac{\delta z}{R_1} + \frac{\delta z}{R_2})A$, respectively. Neglecting the influence of gravity, the free energy variation δG associated with the deformation is

solely due to the variation of A and the pressure-volume energy and can be expressed as:

$$\begin{aligned} \delta G = \gamma \delta A + \Delta P \delta V = \\ = \gamma \left(\frac{\delta z}{R_1} + \frac{\delta z}{R_2} \right) A - \Delta P A \delta z = 0. \end{aligned} \tag{2.3}$$

Consequently, the pressure difference at the interface results to be:

$$\Delta P = \gamma \left(\frac{1}{R_1} + \frac{1}{R_2} \right), \tag{2.4}$$

where $\left(\frac{1}{R_1} + \frac{1}{R_2} \right)$ is identified as the mean curvature of the interface.

2.1.3 Contact angle

In the case of solid, liquid, and gas phases in contact, it is possible to identify the contact angle (CA) that acts at the contact line between them (see Fig. 2.1a). Let us consider an infinitesimal displacement δx of the contact line, as shown in Fig. 2.1b. The free energy variation associated with the displacement per unit of contact line (w) is given by:

$$\frac{\delta G}{w} = \gamma_{sl} \delta x + \gamma_{lg} \delta x \cos\theta - \gamma_{sg} \delta x = 0, \tag{2.5}$$

thus the CA can be expressed using the Young equation:

$$\cos\theta_Y = \frac{\gamma_{sg} - \gamma_{sl}}{\gamma_{lg}}, \tag{2.6}$$

where γ_{sg} is the surface free energy of the solid substrate, γ_{sl} the solid/liquid interface tension, and γ_{lg} the liquid/gas surface tension. θ_Y indicates the Young or intrinsic contact angle, meaning that it depends only on the interface's chemical properties; for this reason, the Young equation is valid only for homogeneous flat surfaces. Depending on the value assumed by θ_Y it is possible to identify different conditions. If $\theta_Y = 0^\circ$ the liquid phase spreads indefinitely over the surface; this condition is also defined as complete wetting. If $0^\circ < \theta_Y < 90^\circ$ the surface is defined as "philic", while if $\theta_Y > 90^\circ$ the surface is said "phobic" to the probe liquid. When $\theta_Y > 150^\circ$ the surface is defined as "super-phobic". For the sake of simplicity, and unless otherwise specified, we will consider water as the probe liquid. Therefore, we will refer to surfaces as "hydrophilic", "hydrophobic", or "super-hydrophobic".

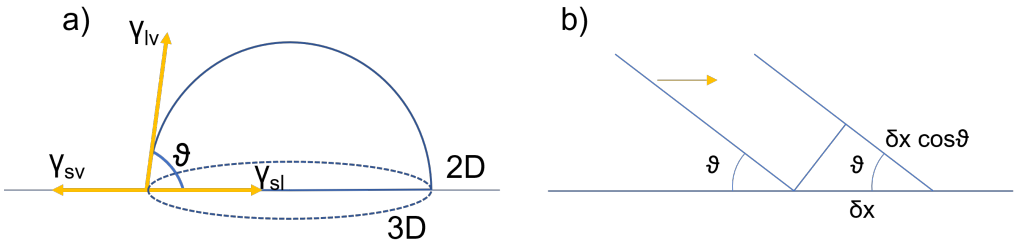

Fig. 2.1 Basic concepts of wetting. (a) Force balance at the contact line between interface tensions and definition of contact angle (CA = θ). (b) Displacement of the contact line on a solid smooth surface.

From an energetic standpoint, the phenomenon of different phases in contact can be explained in terms of adhesion. This can be expressed by considering the free energy change associated with the creation of new interfaces when separating two phases in contact, as described by the Dupré equation [148, 149]:

$$\Delta F = W_{ad} = \gamma_{lg} + \gamma_{\mathrm{sg}} - \gamma_{sl}, \tag{2.7}$$

where W_{ad} is the work of adhesion, that is reversible work required to separate a unit area of interface between two phases (i.e., liquid and solid) in a surrounding phase (gas). By combining equations 2.6 and 2.7 it is possible to express the CA using the Young-Dupré equation:

$$\cos\theta = \frac{W_{ad}}{\gamma_{lg}} - 1. \tag{2.8}$$

Up until now, only the static condition has been discussed. When the droplet moves over the surface - due to tilting or inflating/deflating - the static CA no longer represents the wetting phenomenon accurately. Indeed, real surfaces are not atomically flat, and roughness or defects can hinder motion. When the substrate is tilted, for example, the contact line is pinned and two angles appear, namely the advancing CA (θ_A) and the receding CA (θ_R) (see Fig. 2.2a). The difference between (θ_A) and (θ_R) is known as contact angle hysteresis. Therefore, an interface is fully characterized only when both the static and dynamic CA can be defined. The combination of the static and hysteresis CA is essential for surfaces designed for self-cleaning applications. In such cases, the surface requires to be super-hydrophobic with low hysteresis.

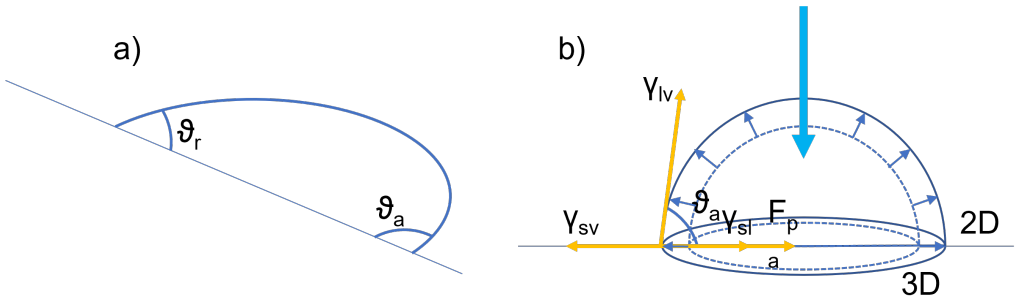

Fig. 2.2 Evaluation of the advancing CA. (a) Identification of advancing and receding CAs with the tilted method; (b) identification of the advancing CA with the needle method.

2.1.4 Capillary length

In the description given so far, the effect of external forces such as gravity was neglected. However, its action can affect the shape of the droplet deposited on a surface. By equating Eq. 2.4 to the hydrostatic pressure, it is possible to identify the characteristic length commonly known as the capillary length (R_c) above which the effect of gravity overrides capillarity:

$$\Delta P = \gamma \left(\frac{1}{R_c} + \frac{1}{R_c} \right) = \rho g h = 2\rho g R_c, \tag{2.9}$$

where ρ is the density of the liquid phase, g the gravity acceleration, and $h = 2R_c$ is the height of the droplet. Therefore, the capillary length is:

$$R_c = \sqrt{\frac{\gamma}{\rho g}}. \tag{2.10}$$

2.1.5 Wetting on rough surfaces

The wettability of non-flat surfaces differs from that of flat surfaces due to the presence of roughness or designed structures that perturb the interface. Surface morphology can either enhance or reduce wettability, depending on the chemistry of the interface and the contact angle θ_Y. Two main analytical theories have been developed to describe the two corresponding states of non-flat surfaces: the Wenzel state [34] and the Cassie-Baxter (CB) state [35].

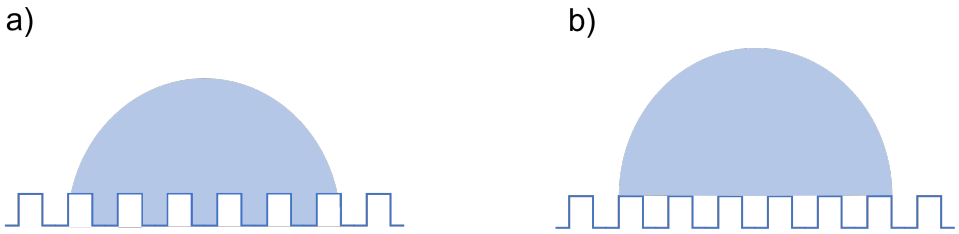

Fig. 2.3 Wetting on rough surfaces: (a) Wenzel state and (b) Cassie-Baxter states.

Wenzel state

Both intrinsically hydrophilic and hydrophobic surfaces can access the Wenzel state. This state represents a liquid that completely fills the profile of a rough surface while presenting a finite contact angle (CA). The effective wet surface (A_{eff}) is higher than the projected one (A_{proj}) underneath the droplet (see Fig. 2.3a). Considering the free energy variation per unit length associated with an infinitesimal displacement of the contact line:

$$\frac{\delta G}{w} = (\gamma_{sl} - \gamma_{sg}) R_f \delta x + \gamma_{lg} \delta x \cos\theta = 0, \tag{2.11}$$

where $R_f = \frac{A_{eff}}{A_{proj}}$ is defined as the Wenzel roughness factor. The Wenzel CA (θ_W) results:

$$\cos\theta_W = r \cos\theta_Y. \tag{2.12}$$

From Eq. 2.12, it is easy to deduce that the Wenzel state amplifies the intrinsic wetting behavior of the surface: if the surface is intrinsically hydrophilic, θ_W will result in a lower value than θ_Y; on the contrary, if the surface is intrinsically hydrophobic, θ_W will result in a higher value than θ_Y. Finally, it is worth mentioning that despite the possibility of achieving high CAs, even comparable to super-hydrophobic conditions, interfaces in the Wenzel state usually exhibit high hysteresis, impeding easy removal of the liquid from the surface, as also described by the rose petal effect [17].

Cassie-Baxter state

In the CB state, the liquid does not completely fill the surface profile, resulting in the presence of air pockets between the liquid and solid surface (see Fig. 2.3b). The overall contact angle is a mean value between the intrinsic θ_Y and $\theta_{air} = 180°$. Once again, considering the free energy variation due to an infinitesimal displacement of

the contact line:

$$\frac{\delta G}{w} = (\gamma_{sl} - \gamma_{sg})\, f_{sl}\delta x + \gamma_{lg} f_{lg}\delta x + \gamma_{lg}\delta x \cos\theta = 0, \tag{2.13}$$

where f_{sl} and f_{lg} indicate the liquid fraction in contact with the solid substrate and trapped air, respectively. Consequently, the CA associated with the CB (θ_{CB}) state is:

$$\cos\theta_{CB} = f_{sl}\,(1 + \cos\theta_Y) - 1. \tag{2.14}$$

By comparing the interfacial energies of the Wenzel and Cassie-Baxter states, it is possible to determine the transition between the two states, which is associated with a critical CA value θ_c. The CB state is favorable if the energy difference δE_{CB} between the CB state and the Wenzel state is lower than δE_W. Therefore, the CB state is favourable if $\delta E_{CB} < \delta E_W$ and thus:

$$(\gamma_{sl} - \gamma_{sg})\, f_{sl}\delta x + \gamma_{lg} f_{lg}\delta x + \gamma_{lg}\delta x \cos\theta_{CB} < (\gamma_{sl} - \gamma_{sg}) r\delta x + \gamma_{lg}\delta x \cos\theta_W. \tag{2.15}$$

The critical CA results:

$$\theta_c = -\frac{f_{lg}}{r - f_{sl}}. \tag{2.16}$$

2.2 Experimental approaches for surface design and characterization

Experimental techniques have been employed to characterize surfaces and gain insights into their chemical, physical, structural, and topological properties. Various methods, such as optical, electronic, or scanning probe microscopy, spectroscopy analysis, and 3D profilometry are commonly used to study the physical and chemical properties of surfaces, their frequency modes, and structures [150, 151]. To evaluate the wettability properties of materials, a commonly used methodology involves the sessile droplet experiment to measure static contact angles, and the "tilting" or "syringe" methods to evaluate dynamic contact angles [152–155].

In this section, we provide a brief description of the experimental methods adopted to assist and validate the numerical protocol objective of this thesis, both

in terms of surface composition and structure and wettability properties[2]. For a more comprehensive discussion of available techniques, we refer readers to specific textbooks and lectures on experimental surface characterization [150, 151, 153].

2.2.1 Surface structure and composition

This subsection outlines the experimental techniques used to acquire specific structural and chemical parameters assumed as input values for MD simulations.

Atomic force microscopy

Atomic-force microscopy (AFM) is a versatile and powerful imaging technique that can visualize a wide variety of surfaces, including polymers, ceramics, composites, glass, and biological samples. To perform AFM, a sharp tip, typically 10-20 nm in diameter, is attached to a free-end cantilever. The tip responds to interactions with the surface, and this movement is recorded by focusing a laser beam on the tip with a photodiode [156]. AFM can be operated in two basic modes: contact and tapping. In the contact mode, the tip remains in continuous contact with the surface, while in the tapping mode, the cantilever is vibrated above the sample surface so that the tip intermittently contacts the surface. Tapping mode is more commonly used for imaging because it reduces shear forces associated with tip movement, while the contact mode is reserved for specialized applications such as force measurements. Compared to electron microscopy, which provides a two-dimensional projection or image of a sample, AFM provides a true three-dimensional surface profile. Moreover, AFM can operate in ambient air, whereas electron microscopy requires an expensive vacuum environment. However, AFM's disadvantage is its smaller imaging size, with a maximum scanning area of about 150 by 150 micrometers and a maximum height of only a few micrometers.

[2]Experiments related to Chapter 3 have been performed in collaboration with the Inter-Departmental Laboratory of Electron Microscopy (LIME) of Roma Tre University for the Oyster project (Grant Agreement No. 760827). Experiments related to Chapter 5 have been performed at the MNFTL and BRL groups of University of Illinois at Chicago (Sreya Sarkar, personal communication, 2023)

Raman spectroscopy

Raman spectroscopy [157] is a technique for studying the vibrational modes of molecules and determining the chemical composition of a material's surface. When laser light interacts with molecular vibrations, phonons, or other excitations of the sample surface, some of the photons are scattered elastically (Rayleigh scattering), while others are scattered inelastically (Raman scattering). The wavelength of the scattered light is specific to the chemical components present in the sample, allowing the chemical composition of the surface to be determined. A spectrometer collects and analyzes dispersed light by separating different wavelengths of light and measuring their intensities. The resulting Raman spectrum provides a unique fingerprint of the sample's chemical composition, allowing distinct molecular species to be identified.

2.2.2 Wetting experiments

This subsection outlines the experimental techniques used to acquire contact angle and wetting behaviors of surfaces and thus validate the numerical model proposed.

Sessile droplet experiment

The sessile droplet experiment represents one of the most commonly used techniques for characterizing solid surfaces by evaluating their wettability and surface free energy. This method involves placing a probe liquid droplet onto the surface and directly measuring the contact angle (CA). To ensure that the measured CA is not affected by gravity and reflects only capillary forces, the diameter of the droplet must be smaller than its capillary length. For water, this value is approximately 2.7 mm.

The Owens-Wendt interpolation method [56] can be used to estimate the surface free energy (SFE). This method is based on the hypothesis that the solid-liquid interface tension is derived from the geometric mean of two relevant components of energy: the disperse (γ_S^D and γ_L^D) and polar (γ_S^P and γ_L^P) surface free energies of the solid substrate and liquids used, respectively. To apply this method, a linear interpolation of the following equation is required, considering at least two different

liquids:

$$\frac{(1/2)(1+\cos\theta)\gamma_l}{(\gamma_l^P)^{1/2}} = \left(\frac{\gamma_l^D}{\gamma_l^P}\right)^{1/2} \cdot \left(\gamma_S^D\right)^{\frac{1}{2}} + \left(\gamma_S^P\right)^{\frac{1}{2}}, \tag{2.17}$$

which is obtained as a combination of the Young equation (2.6) with the Good-Girifalco definition of interfacial tension [58]:

$$\gamma_{sl} = \gamma_{sg} + \gamma_{lg} - 2\left(\sqrt{\gamma_{sg}^D \cdot \gamma_{lg}^D} + \sqrt{\gamma_{sg}^P \cdot \gamma_{lg}^P}\right). \tag{2.18}$$

Since $\gamma_l = \gamma_l^P + \gamma_l^D$ is typically known for probe liquids at given thermodynamic conditions, θ measures can be fitted by Eq. 2.17 and the optimal slope $\left(\gamma_S^D\right)^{\frac{1}{2}}$ and intercept $\left(\gamma_S^P\right)^{\frac{1}{2}}$ identified. The overall SFE of the solid surface is ultimately obtained as the sum of its disperse and polar components, namely $\gamma_S = \gamma_S^P + \gamma_S^D$.

Dynamic contact angle experiment

The dynamic CA can be evaluated by observing the change in the shape of a liquid droplet when it begins to move. There are different methods to evaluate the dynamic CA, including the tilting and needle methods [152]. In the former, a droplet is placed onto the surface (similar to the sessile droplet experiment) which is tilted until the droplet begins to move. The advancing CA corresponds to the angle measured at the front of the advancing droplet, while the receding CA refers to the one observed at the back of the droplet (see Fig. 2.2a). In the latter, a needle pumps or extracts liquid from the droplet, and the advancing and receding CAs are evaluated when the contact line starts to move (see Fig. 2.2b).

The dynamic CA is useful in determining the hysteresis and roll-off properties of surfaces, such as those used in self-cleaning applications. Additionally, the advancing CA has recently been used to evaluate the solid-liquid interfacial tension. Based on the work of Makkonen [103], the frictional tension experienced at the contact line due to the advancement of the droplet corresponds to the solid-liquid interfacial tension. Considering a displacement dx of the contact line, a new solid-liquid interface is created, and the associated work is given by [154]:

$$dW = F_a dx = \gamma_{sl} dA = \gamma_{sl} 2\pi r_c dx, \tag{2.19}$$

where F_a is the resisting force and dA is the new portion of the interface, and r_c is the radius of the contact line. Therefore:

$$F_{pa} = \frac{F_a}{2\pi r_c} = \gamma_{sl}, \tag{2.20}$$

where F_{pa} is the resisting force per unit of the contact line. This relation can be extended to rough surfaces in the hydrophilic regime by assuming the Wenzel roughness factor r:

$$F_{pa} = r\gamma_{sl}. \tag{2.21}$$

According to the equation proposed by Adam and Jessop [158], which was extended for rough surfaces by Good [159], the resisting force per unit of the contact line is related to the advancing and static CAs as follows:

$$r(\gamma_{sg} - \gamma_{sl}) = \gamma_{lg}\cos\theta_a + F_{pa}, \tag{2.22}$$

where θ_a is the advancing CA. Finally, considering again the Young equation 2.6:

$$F_{pa} = \gamma_{lg}(r\cos\theta - \cos\theta_a). \tag{2.23}$$

2.3 Numerical approaches for surface design and characterization

Numerical techniques are being recently used to characterize and assist the design of surfaces, thanks mainly to the increment in computational resources available nowadays. Specifically for wetting behaviors of surfaces, various methods are generally adopted, such as the reproduction of the sessile experiments with MD simulations or phase-field continuum models, or free energy perturbation in atomistic simulations.

In this section, we provide a description of the numerical methods used to develop the numerical protocol objective of this thesis.

2.3.1 Molecular dynamics

Molecular dynamics (MD) is a field of study that focuses on examining the movements and interactions of particles, atoms, and molecules within systems. Through this analysis, it is possible to determine various properties and characteristics of these systems. This approach utilizes Newton's laws of motion to describe molecular systems. According to the Born-Hoppenheimer approximation, each atom is treated as a single-point particle with designated interaction properties. A force field is utilized to describe the parameters of interaction between particles, with bonds being generally represented as springs. Forces are then calculated by deriving the potential energy function, which is obtained empirically and is also referred to as the force field (FF):

$$\mathbf{F}(\mathbf{r}_i) = -\frac{\partial U(\mathbf{r}_i)}{\partial \mathbf{r}_i} = m_i \frac{\partial \mathbf{r}_i}{\partial t}, \tag{2.24}$$

where $\mathbf{F}_b$ indicates the force acting on the i-th particle U_b indicates the potential energy and $\mathbf{r}_i$ indicates the position and m_i the mass of the i-th particle. To solve the differential problem in molecular dynamics, initial conditions for both position and velocity must be specified, and an appropriate integration algorithm must be selected. The potential energy function utilized should account for various factors, including interactions between bonded atoms, valence angles (between three atoms), torsional potential due to bond rotation, and non-bonded interactions such as Coulombic and van der Waals forces. A common form for this function is:

$$U\left(\mathbf{r}^N\right) = U_{bonds} + U_{angles} + U_{torsions} + U_{vdW} + U_{Coulomb}, \tag{2.25}$$

where U_{bonds}, U_{angles}, and $U_{torsions}$ indicate the linear bond interaction between two atoms (1-2 interaction), valence angle between three atoms (1-3 interaction), and torsional potential between 4 atoms (1-4 interaction), respectively. The last two contributions, U_{vdW} and $U_{Coulomb}$, represent the non-bonded van der Waals and electrostatic interaction terms between two atoms, which are generally modeled with the Lennard-Jones (LJ) and Coulomb potentials, respectively.

2.3.2 Force field

The potential energy of the system is formulated as a function of the atomic coordinates using a series of energy functions and parameters, collectively referred to as

force fields. These force fields' parameters are typically derived through ab initio or quantum mechanical simulations or are adjusted to align with experimental data [160]. Various force field models have been developed for molecular dynamics (MD) simulations, contingent on the methodology of parameterization and the intended simulation type.

Force fields can be broadly classified based on how they define the potential's components. In Class I force fields, for example, bonds, angles, torsional angles, and out-of-plane terms are represented using harmonic functions. However, a significant limitation of this class stems from the reliance on harmonic functions, which accurately depict dynamics only in the vicinity of equilibrium positions.

Conversely, Class II force fields incorporate cubic and quartic terms alongside the harmonic components to account for bonds, angles, torsional angles, and out-of-plane effects. Moreover, Class II force fields encompass cross-term interactions that capture the interplay between adjacent bonds, angles, and dihedrals. However, an inherent challenge of Class II force fields is the complexity of optimizing the larger set of parameters involved in simulations.

Finally, Class III force fields introduce additional terms to account for special effects like molecular polarization.

As a result, the selection of the appropriate force field typically hinges on the intended application of the molecular dynamics (MD) simulation and the subsequent fine-tuning of its parameters. Among the most frequently utilized force fields, Charmm [161], Gromos [162], and Amber [163] are commonly employed for biomolecular simulations, while OPLS [164] and Compass [165] find usage in the study of liquids and condensed matter systems. The decision regarding the suitable force field also takes into account the complexity of the molecules under investigation, along with the availability of specific elements within the force field. For instance, the Universal Force Field (UFF) [166] and Dreiding [167] are illustrative examples, as they encompass all elements present in the periodic table, facilitating the simulation of intricate molecular structures.

In this thesis, the OPLS-AA force field model has been employed for all atomistic simulations, primarily chosen for its exceptional capability in representing soft matter interactions within aqueous environments. The efficacy of OPLS-AA, in comparison to alternative force fields designed for soft matter, is further validated by

D. Shivakumar *et al.*, who conducted calculations of solvation-free energy through the Free Energy Perturbation (FEP) method [168].

Below, the form of the OPLS-AA force field [164] is described, being the most adopted in this thesis.

Bonded interactions

Generally, four types of interaction participate in bonded terms: linear bonds, angles, proper dihedrals, and improper dihedrals.

Linear bonds. Linear bonds are described using an harmonic form, modeled on the Hooke's law:

$$U_{bonds}(l) = \frac{k}{2}(r - r_0)^2, \tag{2.26}$$

where k is the elastic constant (J/m^2), r is the relative distance between bonded atoms and r_0 is the equilibrium distance.

Angle bending. As already done for the linear bonds, the deviation of angles from their equilibrium state can be described with a harmonic potential:

$$U_{angles}(\theta) = \frac{l}{2}(\theta - \theta_0)^2, \tag{2.27}$$

where l is the elastic constant (J/rad^2), θ is the angle centered between three atoms, and θ_0 is the equilibrium angle.

Torsional terms (proper dihedral). The potential form for torsional terms is given by:

$$\begin{aligned} U_{dihedrals}(\omega) = \frac{m_1}{2}[1 + cos(\omega)] + \frac{m_2}{2}[1 - cos(2\omega)] \\ \frac{m_3}{2}[1 + cos(3\omega)] + \frac{m_4}{2}[1 - cos(4\omega)], \end{aligned} \tag{2.28}$$

where ω is the torsion angle, K_i with $i = 1, ..., 4$ can be considered as the height barrier giving information about the opposition to rotation. f_i instead is the phase factor and defines where the angle passes through its minimum.

Improper torsion (improper dihedral). This term is referred to the *out-of-plane* bending contribute. The potential follows a harmonic form:

$$U_{improper}(\chi) = \frac{n}{2}(\chi - \chi_0)^2, \tag{2.29}$$

where n is the elastic constant and χ is the angle between the plane of the first three atoms of the molecule and the other atom, and χ_0 is the equilibrium improper angle.

Non-bonded interaction

Non-bonded terms include electrostatic and van der Waals interactions.

Electrostatic interaction The electrostatic interaction between two particles or two molecules is described by Coulomb's law:

$$U_C(r) = \sum_{i=1}^{N_A}\sum_{j=1}^{N_B}\frac{q_i q_j}{4\pi\varepsilon_0\varepsilon_r r_{ij}}, \tag{2.30}$$

where N_A and N_B are the numbers of point charges in the molecules, q_i and q_j are the charge values of the point charges, ε_0 is the vacuum dielectric constant and ε_r is the relative dielectric constant of medium (if the simulation is performed in vacuum, this value is set to one) and r_{ij} is the distance between the molecules or atoms.

Van der Waals interaction Van der Waals potential is modeled by the 12-6 Lennard-Jones potential:

$$U_{LJ}(r_{ij}) = 4\varepsilon_{ij}\left[\left(\frac{\sigma_{ij}}{r_{ij}}\right)^{12} - \left(\frac{\sigma_{ij}}{r_{ij}}\right)^{6}\right], \tag{2.31}$$

where σ is the separation for which the interaction energy is zero, called collision diameter, and ε is the well depth. Generally, the LJ parameters for like pair atoms σ_{ii} and ε_{ii} are specified, while for unlike pair they are computed using mixing rules. As an example, σ_{ij} and ε_{ij} can be evaluated through the geometric mixing rule [164]:

$$\varepsilon_{ij} = \sqrt{\varepsilon_i \varepsilon_j}, \tag{2.32}$$

$$\sigma_{ij} = \sqrt{\sigma_i \sigma_j}. \tag{2.33}$$

2.3.3 Ensemble

The purpose of MD simulations is to assess the macroscopic properties of a system by starting from its microscopic configuration. This is achieved by utilizing the concept of an ensemble, which is based on the idea that the macroscopic characteristics of a system are not sensitive to its exact microscopic details.

In statistical mechanics, an ensemble refers to a theoretical construct that allows us to study the behavior of a large number of microscopic systems that share the same macroscopic properties. For example, we may be interested in the behavior of a large number of gas molecules that are at a certain temperature and pressure, but it is not practical to study each molecule. Instead, we can use an ensemble of similar gas systems that share the same macroscopic properties to make predictions about the statistical behavior of the system. Ensemble methods involve using probability theory to calculate the average properties of the system over all possible microstates that are consistent with the macroscopic properties of the ensemble.

Once the ensemble is defined, the macroscopic properties are computed as averages across the entire system. Typically, MD simulations are carried out in three main ensembles:

1. Microcanonical ensemble (NVE) where the number of particles N, the volume V, and the total energy E of the system are maintained constants.

2. Canonical ensemble (NVT) where the number of particles N, the volume, and the Temperature of the system are kept constants. It is useful for example when it is necessary to determine the changes in the behaviors of a system with temperature.

3. Isothermal-isobaric ensemble (NPT) where the number of particles N, the pressure, and the temperature are constants. Many experimental data are obtained under this condition in the laboratory, and for that these simulations are useful for comparison.

4. Grand canonical ensemble (μVT) where fluctuations in the particle number are permitted at a constant chemical potential μ, volume, and temperature.

This ensemble is particularly useful for describing physical phenomena that involve systems in which the number of particles can vary.

2.3.4 Time integration

When using a realistic model, the force acting on each particle will vary as the particle moves to a new position. In such situations, the model is subject to a continuous potential, as discussed in the previous section. To solve the equations of motion under these conditions, a finite difference method is employed. This involves breaking down the integration into multiple small stages, each separated by a fixed time interval δt.

1. At each time step, the force acting on each particle is computed by taking the vector sum of all of its interactions with other particles, based on the potential.
2. Using the force, it is possible to calculate the acceleration of each particle. By combining the acceleration with the particle's position and velocity at the current time step, the velocity, and position of the particle at the next time step can be computed.
3. The force at the new position is then evaluated, and the process can be repeated to calculate the particle's subsequent positions using the same method.

The finite difference algorithms are all based on the assumption that the position, velocity, acceleration, and other dynamic properties can be approximated using a Taylor expansion:

$$\begin{cases} \mathbf{r}(t+\delta t) = \mathbf{r}(t) + \delta t \mathbf{v}(t) + \frac{1}{2}\delta t^2 \mathbf{a}(t) + \frac{1}{6}\delta t^3 \mathbf{b}(t) + \frac{1}{24}\delta t^4 \mathbf{c}(t) + ... \\ \mathbf{v}(t+\delta t) = \mathbf{v}(t) + \delta t \mathbf{a}(t) + \frac{1}{2}\delta t^2 \mathbf{b}(t) + \frac{1}{6}\delta t^3 \mathbf{c}(t) + ... \\ \mathbf{a}(t+\delta t) = \mathbf{a}(t) + \delta t \mathbf{b}(t) + \frac{1}{2}\delta t^2 \mathbf{c}(t) + ..., \end{cases} \tag{2.34}$$

where **r**, **v**, and **a** denote the position, velocity, and acceleration of the atom, respectively, while **b** represents the third derivative and so on. The Verlet algorithm, which is the most commonly used algorithm in molecular dynamics simulations and is also utilized in our work, employs the acceleration and position at time t, as well as the

position at time *t-1*, to compute the position at time *t+1*:

$$\mathbf{r}(t+\delta t) = \mathbf{r}(t) + \delta t \mathbf{v}(t) + \frac{1}{2}\delta t^2 \mathbf{a} + ..., \tag{2.35}$$

$$\mathbf{r}(t-\delta t) = \mathbf{r}(t) - \delta t \mathbf{v}(t) + \frac{1}{2}\delta t^2 \mathbf{a} - ..., \tag{2.36}$$

and summing these two equations:

$$\mathbf{r}(t+\delta t) = 2\mathbf{r}(t) - \mathbf{r}(t-\delta t) + \delta t^2 \mathbf{a}. \tag{2.37}$$

The velocity does not appear explicitly in the Verlet scheme, but it can be simply evaluated as follow:

$$\mathbf{v} = \frac{\mathbf{r}(t+\delta t) - \mathbf{r}(t-\delta t)}{2\delta t}. \tag{2.38}$$

2.3.5 Free energy perturbation methods for interface properties

Considering the definition given in Eqs. 2.1, the value of γ can be evaluated using the free energy perturbation (FEP) approach. Let us consider two thermodynamic states, denoted by 0 and 1, which are characterized by potential energy functions $U_0(r_i)$ and $U_1(r_i)$ with $i = 1, ..., N$, where N is the total number of particles in the system. The Helmholtz free energy difference between states 0 and 1 is given by $\Delta F_{01} = F_1 - F_0$. This value can be calculated using the Zwanzig equation [169]:

$$\Delta F_{01} = -k_B T \ln \left\langle \exp\left(-\frac{U_1 - U_0}{k_B T}\right) \right\rangle_0, \tag{2.39}$$

where k_B represents the Boltzmann constant, T represents the absolute temperature, and $\langle ... \rangle_0$ indicates an average taken with respect to the canonical configurational distribution of state 0. The FEP approach is valid only when state 1 represents a small perturbation to state 0. In the case of γ for example, the state 1 is a small perturbation of the state 0 due to a small variation $\Delta A = A(1) - A(0)$ of the interface area A. The value of γ can be expressed as:

$$\gamma = \lim_{\Delta A \to 0} \left(\frac{\Delta F}{\Delta A}\right)_{NVT} = \lim_{\Delta A \to 0} -\frac{k_B T}{\Delta A} \ln \left\langle \exp\left(-\frac{U_1 - U_0}{k_B T}\right) \right\rangle_0. \tag{2.40}$$

When 1 is not a small perturbation to 0, the FEP approach can still be applied by introducing a set of $L-2$ intermediate states with potentials $U_l(r_1,...,r_N)$, where $l = 1,...,L$. Here, $l = 1$ corresponds to state $\mathscr{A}$, and $l = L$ corresponds to state $\mathscr{B}$. The system is then transformed following a path through each of the intermediate states from 0 to 1, and the average $\Delta U_{l,l+1}$ is computed in each state l. Therefore, the free energy difference can be obtained as:

$$\Delta F_{01} = -k_B T \sum_{l=1}^{L} \ln \left\langle \exp\left(-\frac{\Delta U_{l,l+1}}{k_B T}\right)\right\rangle_l . \tag{2.41}$$

The evaluation of the W_{ad}, for instance, requires the introduction of intermediate states. According to the definition given in Section 2.1.3, as the work required to separate two phases in contact, the state 1, that corresponds to the two separated phases, does not represent a small perturbation of the state 0, that instead corresponds to the two phases in contact. In this case, a coupling parameter (λ) can be applied to the interaction potential between the two phases to connect the state 0 to the state 1 with intermediate states. Every intermediate state represents a small perturbation of the previous one, thus creating an ideal path between the state 0 and 1. Eq. 2.41 can be then expressed as follow:

$$\Delta F_{01} = -k_B T \sum_{l=1}^{L} \ln \left\langle \exp\left(-\frac{U(\lambda_{l+1}) - U(\lambda_l)}{k_B T}\right)\right\rangle_{\lambda_l} . \tag{2.42}$$

To implement such a procedure in MD simulations, the adoption of a soft potential is required [170]. In their soft form, U_{LJ} and U_C potentials are expressed as function of λ as follow:

$$U_{LJ}(r,\lambda) = \lambda^n 4\varepsilon \left\{ \frac{1}{\left[\alpha_{LJ}(1-\lambda)^2 + \left(\frac{r_{ij}}{\sigma}\right)^6\right]^2} - \frac{1}{\left[\alpha_{LJ}(1-\lambda)^2 + \left(\frac{r_{ij}}{\sigma}\right)^6\right]} \right\}, \tag{2.43}$$

$$U_C(r,\lambda) = \lambda^n \frac{q_i q_j}{4\pi\varepsilon_0\varepsilon_r \left[\alpha_C(1-\lambda)^2 + r_{ij}^2\right]^{1/2}}, \tag{2.44}$$

where n is a positive integer, and α_{LJ} and α_C are positive constants. When $\lambda = 1$, the pair potential contributions are identical to the Lennard-Jones and Coulomb terms. When $\lambda = 0$, the interactions are deactivated. U_{LJ} and U_C are plotted in Figs. 2.4a–b for different values of λ.

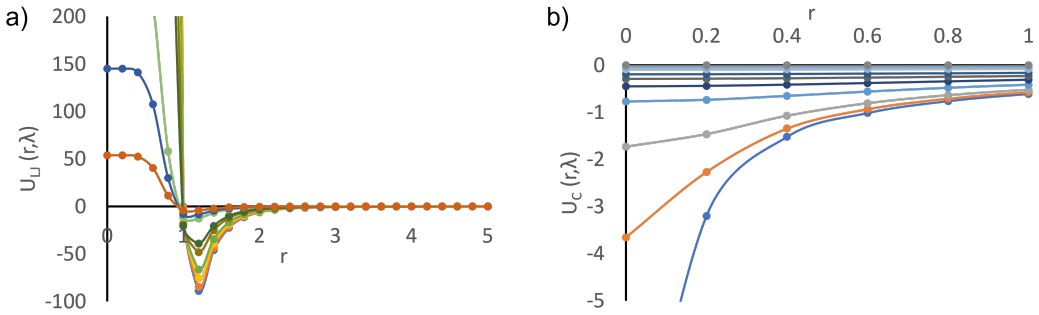

Fig. 2.4 Graphical representation of LJ (a) and Coulomb (b) potentials for different values of λ.

2.3.6 Irving-Kirkwood relation for interface tension

The Irving-Kirkwood relation provides a mechanical method for evaluating the tension at a liquid interface. This relation is derived from the principle of virtual work. Let us consider an element of fluid $dV = L_x L_y dz = Adz$, where A denotes the interface area. Now, let us suppose that there is a deformation of the fluid element which preserves its volume but increases the interface area. The deformation is described through a deformation tensor given by $\varepsilon_{xx} = \varepsilon_{yy} = (1+\varepsilon), \varepsilon_{zz} = \frac{1}{(\varepsilon_{xx}\varepsilon_{yy})}$, such that $\delta A = 2\varepsilon A$ and $\delta z = \frac{1}{\varepsilon^2} L_z$, with ε defined as a small perturbation factor. The work done by the system due to this deformation is given by:

$$\delta W = \varepsilon L_x L_y dz \left(P_x(z) + P_y(z) - 2P_z(z)\right). \tag{2.45}$$

Consequently, the free energy variation per unit area:

$$\frac{\delta F}{\delta A} = \delta z \left(P_N(z) - P_T(z)\right), \tag{2.46}$$

where, $P_N(z) = P_z(z)$ represents the pressure component perpendicular to the surface, and $P_T(z) = \frac{1}{2}\left[P_x(z) + P_y(z)\right]$ represents the average pressure component acting parallel to the interface. Finally, using the definition of interface tension given in Eq. 2.1, we can write:

$$\gamma = \int_{-\infty}^{\infty} \left(P_N(z) - P_T(z)\right) dz. \tag{2.47}$$

2.3.7 Coarse-grained molecular dynamics

Atomistic simulations describe the interactions and motions of individual atoms, providing detailed and accurate predictions of the physical properties of a system. However, these simulations are computationally expensive and are typically only applicable to small systems, up to a few tens of nm, or short timeframes, up to hundreds of nanoseconds. In contrast, coarse-grained (CG) simulations represent groups of atoms or molecules as single particles and model the interactions between these particles at a less detailed level. This results in a significant reduction in computational cost, enabling simulations of larger systems or longer timeframes. However, the accuracy of the predictions may be lower than that of atomistic simulations.

For the development of the CG systems proposed in this work, we chose the MOLC model [138]. In the MOLC model, groups of atoms are replaced with anisotropic ellipsoids, which can eventually be reduced to spheres. In the case of small molecules like water, each molecule is replaced with a single rigid sphere. On the other hand, large molecules like polymers are divided into several ellipsoidal fragments connected by directional bonds. The parameterization of the MOLC model is based on a bottom-up approach, using the all-atom (AA) representation of the single molecule as a reference. Short-range repulsive and attractive interactions are described with the Gay-Berne potential [171–173], and point charges are assigned to each bead to account for electrostatic interactions. For each pair of bonded beads, the interaction is due to the bonded potential only.

The internal energy (U) of the CG system can be written as:

$$U(\mathbf{r},\mathbf{Q}) = \sum_{i<j}\left[U_{ij}^{GB} + U_{ij}^{Coulomb}\right] + \sum_{i<j} U_{ij}^{Flex}, \tag{2.48}$$

where U_{ij}^{GB} indicates the Gay-Berne contribution, $U_{ij}^{Coulomb}$ the electrostatic contribution and U_{ij}^{Flex} the bond contribution. $U(\mathbf{r},\mathbf{Q})$ is a function of the position $\mathbf{r}(\mathbf{r_1},\mathbf{r_2},...,\mathbf{r_n})$ and orientation expessed as a set of quaternions $\mathbf{Q}(\mathbf{q_1},\mathbf{q_2},...,\mathbf{q_n})$ of all the beads in the system.

Gay-Berne potential

U_{ij}^{GB} is expressed as:

$$U_{ij}^{GB} = 4\varepsilon_0 \varepsilon \left(\hat{r}_{ij}, \mathbf{q}_i, \mathbf{q}_j\right) \left[u^{12}\left(\mathbf{r}_{ij}, \mathbf{q}_i, \mathbf{q}_j\right) - u^{6}\left(\mathbf{r}_{ij}, \mathbf{q}_i, \mathbf{q}_j\right)\right], \tag{2.49}$$

where $\mathbf{r}_{ij}$ is the vector connecting the centers of mass of different beads, with the direction along the unit vector $\hat{r}_{ij}$, and ε_0 is the energy scale. The orientation of each bead is instead expressed with quaternions $\mathbf{q}_i$ and $\mathbf{q}_j$. The function $u\left(\mathbf{r}_{ij}, \mathbf{q}_i, \mathbf{q}_j\right)$ is expressed as:

$$u\left(\mathbf{r}_{ij}, \mathbf{q}_i, \mathbf{q}_j\right) = \frac{\sigma_c}{\left(\mathbf{r}_{ij} \cdot \sigma\left(\hat{\mathbf{r}}_{ij}, \mathbf{q}_i, \mathbf{q}_j\right) + \sigma_c\right)}, \tag{2.50}$$

which contains the anisotropic contact term $\sigma(\hat{\mathbf{r}}_{ij}, \mathbf{q}_i, \mathbf{q}_j)$, which approximates the contact distance between the ellipsoids. This function depends on the ellipsoid axis lengths σ_x, σ_y, and σ_z, as well as on σ_c, which controls the width of the potential well. Finally, $\varepsilon\left(\hat{\mathbf{r}}_{ij}, \mathbf{q}_i, \mathbf{q}_j\right)$ defines the depth of the potential well, and it depends on the orientations of the two particles, the inter-bead vector, and the interaction parameters ε_x, ε_y, and ε_z. The parameters for the Gay-Berne interaction between unlike beads are obtained through the Lorentz-Berthelot mixing rules:

$$\varepsilon_{ij} = \sqrt{\varepsilon_i \varepsilon_j}, \tag{2.51}$$

$$\sigma_{ij} = \frac{1}{2}(\sigma_i + \sigma_j). \tag{2.52}$$

Electrostatic interaction

The electrostatic interaction is taken into account by decorating each bead with massless point charges. The position and intensity of each charge are determined to reproduce the electrostatic potential of the corresponding AA representation. The charges are not generally placed at the center of the bead and are defined as off-center charges (OCC).

Electrostatic interactions in the MOLC model are computed by rewriting the usual Coulomb expression from the charge frame of reference to the ellipsoid frame

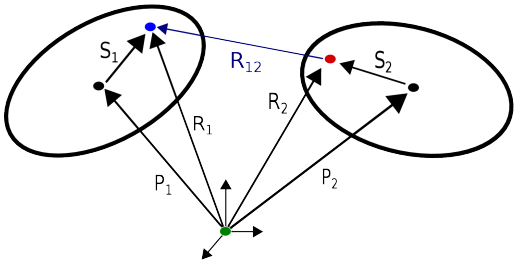

Fig. 2.5 Diagram showing two off–centre charges, in blue and red, defined for two ellipsoids. Fig. from Ref. [2]

of reference. The direct Coulomb potential in real space is given by:

$$U_{Coul} = C \cdot \frac{q_1\, q_2}{R_{12}} = C \cdot \frac{q_1\, q_2}{\sqrt{\mathbf{R}_{12} \cdot \mathbf{R}_{12}}}, \tag{2.53}$$

where C is an energy–conversion constant, q_1 and q_2 the virtual charges and the norm $R_{12} = \sqrt{\mathbf{R}_{12} \cdot \mathbf{R}_{12}}$ is the scalar distance. As shown in Fig. 2.5, the vector distance between the virtual charges is expressed as:

$$\mathbf{R}_{12} = \mathbf{R}_1 - \mathbf{R}_2 = \mathbf{P}_1 + \mathbf{S}_1 - (\mathbf{P}_2 + \mathbf{S}_2), \tag{2.54}$$

where $\mathbf{R}_i = \mathbf{P}_i + \mathbf{S}_i$ (i = 1, 2) is the position of the virtual charge, $\mathbf{P}_i$ the center of the ellipsoid, and $\mathbf{S}_i$ the relative position of the virtual charges in the ellipsoid system of reference. In this notation, $\mathbf{R}_i$ is obtained by rotating the charge position from the ellipsoid's frame to the frame of reference using the quaternion of the parent ellipsoid followed by a translation. The dot product in Equation 2.53 can be expanded as follows:

$$\begin{aligned} \mathbf{R}_{12} \cdot \mathbf{R}_{12} = {} & \mathbf{P}_1 \cdot \mathbf{P}_1 + \mathbf{S}_1 \cdot \mathbf{S}_1 + \mathbf{P}_2 \cdot \mathbf{P}_2 + \mathbf{S}_2 \cdot \mathbf{S}_2 + 2\,\mathbf{P}_1 \cdot \mathbf{S}_1 + 2\,\mathbf{P}_2 \cdot \mathbf{S}_2 \\ & - 2\,\mathbf{P}_1 \cdot \mathbf{P}_2 - 2\,\mathbf{S}_1 \cdot \mathbf{S}_2 - 2\,\mathbf{P}_1 \cdot \mathbf{S}_2 - 2\,\mathbf{P}_2 \cdot \mathbf{S}_1. \end{aligned} \tag{2.55}$$

The force that the virtual charge 1 exerts on its parent ellipsoid bead is computed from the gradient of the potential with respect to $\mathbf{P}_1$. The derivative $\partial(\mathbf{R}_{12} \cdot \mathbf{R}_{12})/\partial \mathbf{P}_1$ is calculated below:

$$\frac{\partial(\mathbf{R}_{12} \cdot \mathbf{R}_{12})}{\partial \mathbf{P}_1} = 2\,\mathbf{P}_1 + 0 + 0 + 0 + 2\,\mathbf{S}_1 + 0 - 2\,\mathbf{P}_2 - 0 - 2\,\mathbf{S}_2 - 0 = 2\,\mathbf{R}_{12}. \tag{2.56}$$

Hence the force becomes:

$$\begin{aligned}
\mathbf{F}_1 &= -\frac{\partial U_{Coul}}{\partial \mathbf{P}_1} = C \cdot \left[\frac{q_1\, q_2}{\sqrt{\mathbf{R}_{12} \cdot \mathbf{R}_{12}}} \right]'_{\mathbf{P}_1} \\
&= -C\, \frac{q_1\, q_2}{-2\, \sqrt{\mathbf{R}_{12} \cdot \mathbf{R}_{12}}\, (\mathbf{R}_{12} \cdot \mathbf{R}_{12})} [\mathbf{R}_{12} \cdot \mathbf{R}_{12}]'_{\mathbf{P}_1} \\
&= C\, \frac{q_1\, q_2}{2\, \sqrt{\mathbf{R}_{12} \cdot \mathbf{R}_{12}}\, (\mathbf{R}_{12} \cdot \mathbf{R}_{12})} \cdot 2\, \mathbf{R}_{12} \\
&= C\, \frac{q_1\, q_2}{(\mathbf{R}_{12} \cdot \mathbf{R}_{12})} \cdot \frac{\mathbf{R}_{12}}{\sqrt{\mathbf{R}_{12} \cdot \mathbf{R}_{12}}} \\
&= C\, \frac{q_1\, q_2}{(\mathbf{R}_{12} \cdot \mathbf{R}_{12})} \cdot \frac{\mathbf{R}_{12}}{R_{12}},
\end{aligned} \tag{2.57}$$

while the force on the virtual charge 2 is simply defined as $\mathbf{F}_2 = -\mathbf{F}_1$. The torque is defined as:

$$\tau_1 = \mathbf{S}_1 \times \mathbf{F}_1 = C\, \frac{q_1\, q_2}{(\mathbf{R}_{12} \cdot \mathbf{R}_{12})} \cdot \frac{\mathbf{S}_1 \times \mathbf{R}_{12}}{R_{12}}. \tag{2.58}$$

In this case the torque on the second particle can be written as:

$$\tau_2 = \mathbf{S}_2 \times \mathbf{F}_2 = -C\, \frac{q_1\, q_2}{(\mathbf{R}_{12} \cdot \mathbf{R}_{12})} \cdot \frac{\mathbf{S}_2 \times \mathbf{R}_{12}}{R_{12}}. \tag{2.59}$$

Outside the simulation cutoff, the electrostatic interaction is evaluated in reciprocal space by means of the PPPM algorithm [174]. The calculation of electrostatic interactions *via* virtual charges has been implemented in a user-defined package for the program LAMMPS [175, 176] and can be accessed via the keywords `pair_style coul/long/offcentre` and `kspace_style pppm/offcentre`. The code is freely available on GitHub [177].

Bond interaction

The bond interaction potential U_{ij}^{Flex} controls the distance and relative orientation between bonded ellipsoids. If two ellipsoidal beads are directly connected, they interact only through U_{ij}^{Flex}, while non-bonded interaction terms are switched off. In the case of 1–3- and 1–4-connected ellipsoids, non-bonded interactions are computed without any scaling factor. The bond interactions between beads depend on the orientation of beads i and j (unit vectors $\hat{a}_i$ and $\hat{b}_j$, respectively), as well as on the

orientation and length of the bond between beads ($\mathbf{r}_{ij}$):

$$U_{ij}^{Flex} = U_d\left(r_{ij}\right) + \sum_{mn}\left(U_0\left(\hat{a}_i \cdot \hat{b}_j\right) + U_p\left(\hat{r}_{ij} \cdot \hat{a}_i\right) + U_q\left(\hat{r}_{ij} \cdot \hat{b}_j\right)\right), \tag{2.60}$$

where $m,n = x,y,z$ express the Cartesian axes of each bead. U_d corresponds to the contribution due to the relative distance between the beads and can assume a form similar to the one reported in Eq. 2.26. U_0 corresponds to the contribution due to the relative orientation between the beads and can assume a form similar to the ones reported in Eqs. 2.26 and 2.28. Finally, U_p and U_q correspond to the contributions due to the orientation of beads i and j with respect to the bond direction $\hat{r}_{ij}$, and they can assume a form similar to Eq. 2.26. The MOLC model also allows for overlapping connected beads to provide an accurate representation of the volume occupied by the entire molecule.

Chapter 3

Experimentally-augmented atomistic models for PLGA surfaces[1]

This Chapter deals with the development and validation of a new atomistic MD model, for assessing the wettability of soft polymer surfaces through the reproduction of the sessile droplet experiment. The proposed protocol is employed to study the wettability of Poly(Lactic-co-Glycolic Acid) (PLGA) surfaces with water, formamide, toluene, and hexane (see Fig. 3.1). PLGA is a copolymer formed by repeating units of lactic acid (LA) and glycolic acid (GA). PLGA is a relevant case study because its wetting properties determine its biocompatibility and biodegradability in many biomedical applications [178–180].

In detail in this Chapter we:

1. Validate the force field by computing the density and glass transition temperature of a soft material (a polymer), the density and surface tension of the probe liquids, and comparing the computed values with the experimental data available.

2. Create an MD sample whose surface matches the experimental topology of the soft material.

3. Simulate the 3D sessile droplet experiment by evaluating the apparent contact angle from the MD trajectory.

[1]Part of the work included in this chapter was previously published by Bellussi *et al.* in Ref. [1]

Beyond the specific study case addressed here, this model can be transferred to flat, rough, or structured surfaces of both soft and hard surfaces, providing a promising synergistic potential with respect to experimental characterization techniques. Furthermore, in the perspective of a multi-scale framework to assess solid-fluid interface properties and thus guide a rational design of surfaces, the work presented in this Chapter represents the first stage. In detail, the results obtained here can be used as a first set of input parameters for the development of a mesoscopic model based on coarse-grained molecular dynamics, as well as boundary conditions for continuum simulations.

3.1 Materials and methods

3.1.1 Model building

The experimental length of PLGA chains is typically comprised of between 240 and 390 repeating units, a size that is computationally inaccessible for practical applications based on atomistic simulations. Literature works on PLGA have reported MD simulations with a polymer length between 10 and 90 monomers [181–184]. In this work, we used PLGA chains composed of 48 monomers, corresponding to 12 repetitions of 3 LA monomers and 1 GA monomer, thus keeping the 75:25 LA to GA ratio of the experimental samples.

The structure of a single PLGA chain was built with Avogadro [185, 186], while the condensed PLGA phase was generated starting from a randomly sparse configuration of chains in a simulation box with periodic boundary conditions in the three orthogonal directions (see Figs. 3.1a–b). An initial guess composed of 90 polymer chains in a cubic box with a side of 900 Å was created with Moltemplate [137], while the MD simulations were carried out with LAMMPS [176, 175]. The OPLS-AA force field [164] was used to describe the interaction potentials of PLGA, thanks to its exceptional capability in representing soft matter interactions within aqueous and liquid environments [70, 168]. The wettability of PLGA was evaluated with four liquids: water (both Tip4P-05 [187] and SPC-E [188] models), formamide, toluene, and hexane, which were modeled with the OPLS-AA force field (Figs. 3.1c–f). A cutoff of 1.3 nm was used for nonbonded interactions, with cross-term

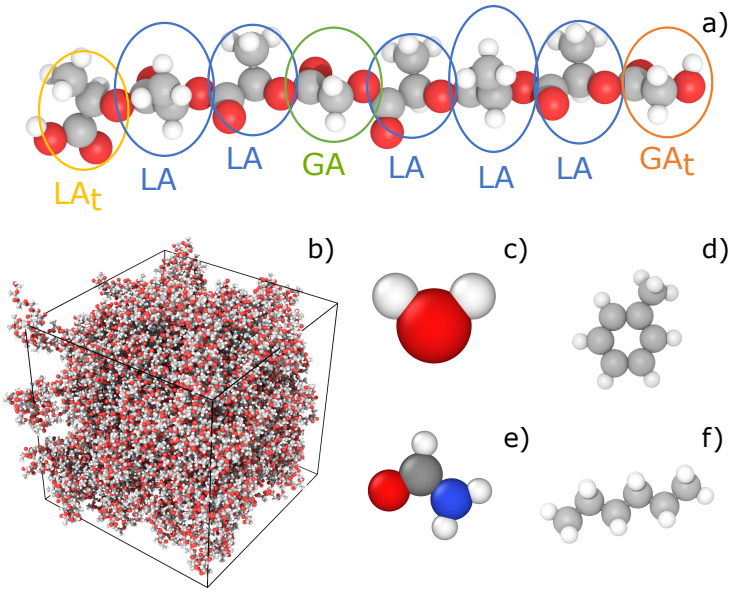

Fig. 3.1 Materials considered in the molecular dynamics simulations. (a) Olygomer of PLGA with the lactic (LA and LA_t) and glycolic (GA and GA_t) monomers highlighted. The subscript t indicates the terminal residuals. (b) Condensed sample of bulk PLGA (box dimension 73 Å). This equilibrated PLGA box was then replicated 3 times in the x and y directions to create a supercell for the CA modeling measurements. (c) Water (SPC-E, Tip4P-05), (d) toluene, (e) formamide, and (f) hexane molecules used in the simulations. Elements are represented by different colors: carbon in gray, oxygen in red, hydrogen in white, and nitrogen in blue. Fig. from Ref. [1].

Lennard-Jones parameters computed with geometric mixing rules. Long-range interactions were computed with the PPPM method [174] with 10^{-4} accuracy.

The equilibration of PLGA samples began with a controlled multi-step compression at 1 K, in which the volume of the simulation box was progressively reduced by 15% in each step for 49 steps. The electrostatic interactions were switched off during this process to emulate the screening induced by a virtual solvent. Then, the bulk sample was relaxed in the isobaric-isothermal ensemble (NPT) at 300 K and 1 atm for 2 ns, with nominal electrostatic interactions. Surfaces of PLGA were created by removing the periodic boundary in the z-direction, turning the bulk into a slab geometry. The system was then equilibrated in the canonical ensemble (NVT) at 300 K to allow surface reconstruction for approximately 4 ns. A correction term for systems with slab geometry was added to the long-range electrostatic interactions [189]. The equilibrated surface was then replicated three times in the x and y direc-

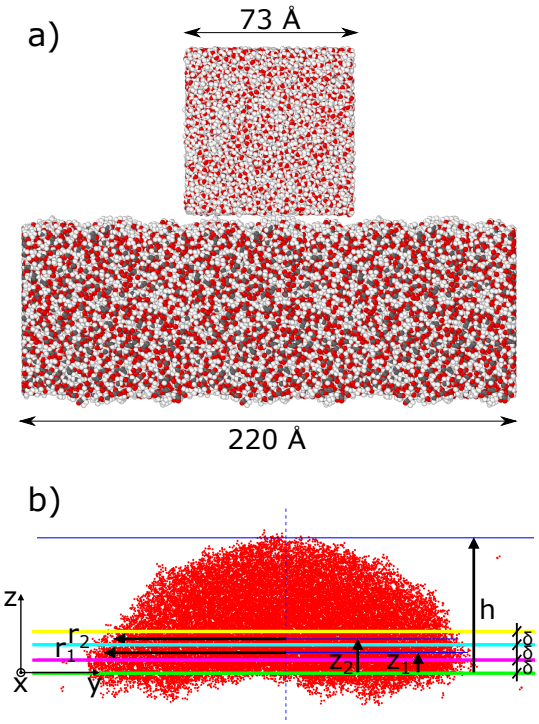

Fig. 3.2 (a) Snapshot of the initial configuration of a water/PLGA sample for MD simulations, detailing the domain size. (b) Schematic view of the process for evaluating the contact angle from the MD trajectory. The dashed blue vertical line identifies the droplet axis; the blue horizontal line is the droplet height limit (h); the green line is the mean plane between the liquid and soft surface. The liquid slabs s_1 and s_2 are defined between the magenta and cyan lines, and the cyan and the yellow lines, respectively. δ indicates the thickness of s_1 and s_2, while z_1 and z_2 the mean line of s_1 and s_2, respectively. Fig. from Ref. [1].

tions, yielding a square surface with a lateral dimension of approximately 220 Å, so that the lateral size of the supercell is approximately two orders of magnitude bigger than the experimental surface roughness. This supercell was used for CA simulations, as its larger size help to avoid finite-size effects, which could affect the wetting properties of the soft interface [71, 72].

The topological characterization of PLGA surfaces is based on the solvent accessible surface (SAS) of the slab, computed with the program Jmol [190] on the final configuration of the NVT simulation. The resulting SAS was exported as a triangular mesh and edited with Meshlab [191] to remove the boundary walls. Then, the surface roughness of PLGA was computed with Gwyddion [192], taking the meshed SAS as input, and compared with the experimentally determined one.

The density and surface tension of the four liquids were used to gauge the accuracy of the force field, by comparing the computed values with the experimental ones. The density was measured on samples made of 1,000 molecules in a periodic box reproducing bulk conditions. Each sample was equilibrated in the NPT ensemble at 300 K and 1 atm for 2 ns with coupling constants of 0.1 and 1 ps for temperature and pressure, respectively. The surface tension was calculated on a slab geometry according to the Kirkwood-Buff relation [193]:

$$\gamma_l = \frac{L_z}{2}\left[\langle P_z\rangle - \frac{\langle P_x\rangle + \langle P_y\rangle}{2}\right], \tag{3.1}$$

where P_z is the liquid pressure in the direction orthogonal to the surface, P_x and P_y are the pressures in the transverse directions, and L_z is the length of the simulation box in the orthogonal direction to the surface, while brackets indicate an NVT ensemble average. A production run of 5 ns was used for data acquisition after the slab was equilibrated for 5 ns.

The apparent contact angle of the different liquids on the PLGA slab was computed with numerical experiments following the droplet method. The initial guess of each droplet was a cube of equilibrated liquid with box edges of approximately 73 Å (see Fig. 3.2a). The droplet was equilibrated on top of the PLGA slab until the potential energy and the evaluated CA reached a stable value with time. The total number of atoms of the slab/solvent systems was approximately 350'000. An example of a LAMMPS script for the numerical sessile droplet experiment is provided in Appendix A.1.1.

The contact angle was calculated from the MD trajectory using a post-processing code developed for this purpose (see the Zenodo archive associated with this work https://doi.org/10.5281/zenodo.6629427). We initially define a mean plane representative of the interface, comparing the positions of liquid and polymer surface atoms. The droplet axis was identified from the average position of all the droplet atoms, and the droplet height h from the interface plane. Then, we consider two contiguous liquid slabs (s_1 and s_2) of height δ at a distance δ from the interface plane. We evaluate the radial density profile of the liquid in s_1 and s_2 to estimate the droplet radius r_1 (at z_1, that is the mean z coordinate of s_1) and r_2 (at z_2, that is the mean z coordinate of s_2) in the $x-y$ plane. We measure the radius at the liquid-air interface, defined as the point where the density falls in a range below 50% of the bulk value (see the code available at Ref. [194] for details). Finally, the CA is

evaluated as $\theta = \arctan(\Delta z/\Delta r)$, where $\Delta r = r_1 - r_2$ and $\Delta z = z_2 - z_1$ (see Fig. 3.2b). This procedure is subject to the choice of δ for the evaluation of r_1 and r_2. Then, we replicate the procedure with different values of δ, expressed as a percentage of the drop height (within 7% and 10%), and average the CA final value from these results.

3.1.2 Sample preparation

Typical commercial proportions of LA:GA in PLGA samples range from 50:50 to 85:15, being 50:50 and 75:25 the most common ones [195]. The presence of CH_3 side groups makes LA more hydrophobic than GA. Therefore, a copolymer with higher LA content absorbs less water and then degrades more slowly, being the 50:50 ratio the one showing the fastest degradation rate [178, 196].

In this work, we focus on 75:25 copolymers (i.e., 66'000–107'000 g/mol molecular weight) to achieve a good balance between durability and hydrophilicity. The PLGA solution was prepared in a mixture of chloroform (Fisher Chemical, USA) with a concentration of 5% in weight. The solution rested for a homogenization time of 12 hours. Then, 2 ml of solution was poured into a dry Petri dish with a diameter of 12 cm and finally dried until the solvent was fully evaporated and the flat slab of PLGA was obtained.

3.1.3 Experimental characterisation

The topological characterization of the PLGA samples was performed in terms of the surface root mean square roughness, evaluated using a Bruker atomic force microscope (AFM Dimension Icon, Bruker) operating in standard tapping mode at a scan rate of 0.996 Hz. The AFM is equipped with a TESP-SS Bruker silicon probe featuring a nominal cantilever elastic constant of $42\,\mathrm{N/m}$ and a tip with a nominal radius of 2 nm. The selection of the AFM operating mode and tip radius value is based and cross-validated considering the relative errors (from the true value of RMS roughness theoretically approachable using an infinitely sharp tip) arising from eventual convolution effects on surface topography, as elucidated by Sedin *et al.* [197]. Indeed, for small lateral scans ($\leq 500\,\mathrm{nm}$), the image root mean square roughness decreases as tip size increases: in the case of the investigations performed, it has been evaluated an error for a tip radius of 2 nm lesser than 3%, eventually falling

within the experimental error associated with surface morphology repeatability. Each measurement was performed on a scan area of 100 nm × 100 nm or 500 nm × 500 nm, where two sensor images were recorded simultaneously (corresponding to forward and backward scans). Images were then analyzed and processed with the software Gwyddion [192].

The solid-liquid interaction between PLGA and the different fluids was validated by sessile droplet contact angle measurements, employing normative-compliant equipment (UNI EN 828, UNI 9752, ASTM D-5725-99). CA testing was conducted at room temperature (20 °C) and relative humidity between 40% and 50%. A minimum of six droplets (with a volume of 3 µL each) of water, formamide (polar solvents), toluene, or hexane (non-polar hydrocarbons) were deposited on the sample surface to measure the apparent contact angle and then estimate the overall surface free energy (SFE) of the PLGA samples. After 60 seconds of stabilization, images of the liquid drops were captured (LAS-EZ software, Leica Camera AG) and subsequently elaborated (ImageJ software) using a spherical approximation of the droplet shape. This method allows assessing the angle formed between the two tangents of the fitted sphere with the straight line corresponding to the sample surface, thus obtaining the CA value (θ).

3.2 Results and discussion

The characterization protocol discussed in this Chapter employs MD simulations to predict the wetting properties of soft interfaces. In this section, we first report the preliminary results obtained to validate the force field adopted, including the density and glass transition temperature (T_g) of PLGA, as well as the density and surface tension of the fluids used in the simulations. Secondly, we present the results of the surface topography characterization, including the root mean square roughness and Wenzel roughness factor. Finally, we discuss the wettability results of PLGA surfaces obtained by numerically reproducing the sessile droplet experiment. All of the results are compared against experiments or results available in the literature to validate the proposed model.

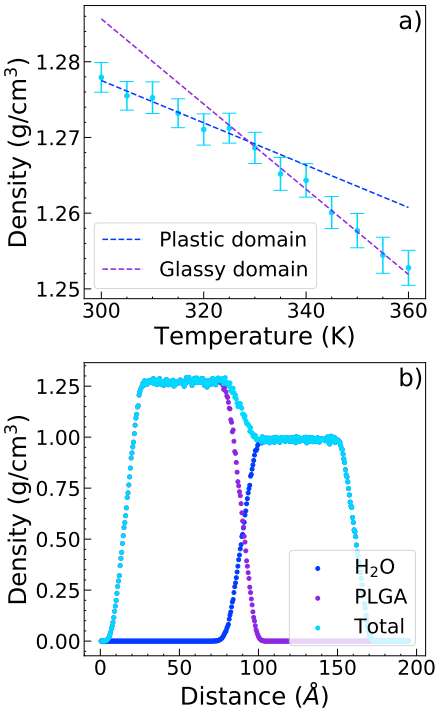

Fig. 3.3 (a) Evaluation of the glass transition temperature of the simulated PLGA sample, obtained from the interpolation of the plastic (in blue) and glassy (in violet) branches. (b) Simulated density profile at the water/PLGA interface, measured on a water film approximately 70 Å thick onto the polymer slab. Fig. from Ref. [1].

3.2.1 Validation of the force field

The wetting properties of PLGA surfaces are assessed after carefully evaluating the bulk properties of the polymer slab and the probe liquids. We evaluate the density and T_g of the simulated PLGA bulk. The density of PLGA computed at 300 K during the equilibrated MD trajectory is equal to 1.275 $\pm$ 0.025 g/cm^3 (the uncertainty was evaluated as the standard deviation of the data acquired along the trajectory), in excellent agreement with the experimental value (1.30 g/cm^3 [195, 198]). The T_g was evaluated by performing a scan in temperature and monitoring the variation of density [199]. In Fig. 3.3a, we report the density of PLGA against temperature, identifying the two distinct branches of the plastic and glassy states. These branches are interpolated with two linear regressions, intercepting at a temperature T_g = 328 K that accurately matches the experimental value of 320–330 K [195].

Similarly, we evaluate the density of the probe liquids at 300 K and 1 atm, finding an excellent agreement with the experimental evidence from the literature

(see Tab. 3.1). For the specific case of water in contact with the polymer substrate, we investigate the coupling of the two phases by considering a liquid film onto the polymer slab and evaluating the density profile along the normal direction to the polymer surface [200].

Results in Fig. 3.3b show an overlap between the two phases in the contact region due to the soft (polymer/water) interface, while the nominal densities of PLGA and pure water are eventually recovered after the interface. In Fig. 3.14a we report the calculated surface tension for the four liquids, finding that MD results are in good agreement with both experimental and other numerical results available in the literature [201–205] (see Tab. 3.1 for details). This evidence supports the reliability of the force field used to describe the PLGA and probe solvents, thus providing confidence for predicting the wetting properties of surfaces.

3.2.2 Surface topography characterization

We characterize the topography of the PLGA surface in terms of the root mean square (RMS) roughness of the MD sample, comparing this value with the value obtained by atomic force microscopy (AFM) measurements. The smallest viable experimental scans are of 100 nm $\times$ 100 nm, from which representative zoomed sections were extracted with a lateral dimension comparable to that of the MD samples (see Fig. 3.4). The RMS roughness of the numerical and experimental samples is 3.2 and 2.2 Å, respectively. According to the Wenzel model for hydrophilic surfaces [34, 206, 207] (i.e., $\cos\theta = R_f \cos\theta_Y$, where θ is the apparent CA, θ_Y the Young CA and $R_f = \frac{A_{eff}}{A_{proj}}$ the roughness factor, being A_{eff} the effective area of the polymer surface and A_{proj} the projected area on the acquisition window), we found the experimental roughness factor in the range of 1.0570–1.1078 depending on the scan size (see Tab. 3.2) and 1.5250 in the MD sample. Considering the non-periodicity of the PLGA surface features (as analyzed from 2D Fast Fourier Transform of AFM scans), the influence of surface topology on the measured CA is smaller than 5% for the conducted experimental tests, thus within the statistical uncertainty of the measure. Consequently, the CA obtained from experiments and simulations can be considered as the Young CA with good approximation ($\theta \approx \theta_Y$). The only notable exception is the case of formamide on PLGA, where the low value of θ leads to larger deviations from θ_Y (see Tab. 3.2).

Table 3.1 Density (ρ), surface tension (γ) and contact angle (θ) of the liquid studied by molecular dynamics simulations. The values in the brackets report the corresponding experimental value at similar testing conditions (298 K and 1 atm). The experimental CA values are the ones obtained by our experiments.

	ρ (g/cm^3)	γ (mN/m)	θ (°)
H_2O Tip4P-05	0.994±0.003 (0.997 [187])	63.1±1.5 (71.8 [204])	61.8±3.8 (65±4)
H_2O SPC-E	0.994±0.003 (0.997 [187])	59.0±1.1 (71.8 [204])	63.2±5.0 (65±4)
CH_3NO	1.117±0.005 (1.129 [201])	56.4±3.8 (57.0 [201])	27.3±5.5 (52±4)
C_7H_8	0.858±0.004 (0.86 [203])	23.8±3.6 (27.73 [202, 203])	0 (0)
C_6H_{14}	0.641±0.003 (0.65 [208])	14.1±3.6 (17.9 [205])	0 (0)

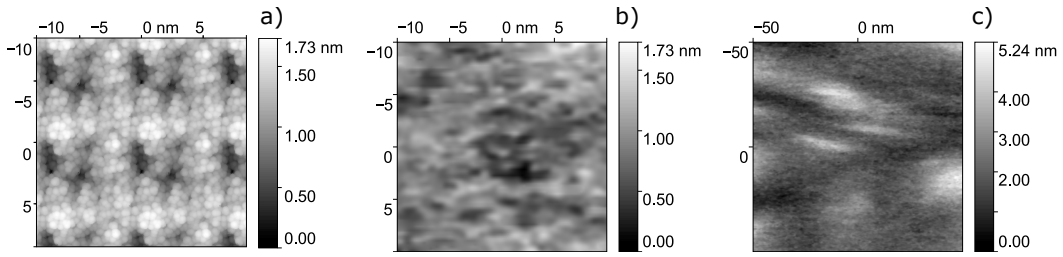

Fig. 3.4 (a) Surface topography analysis of the PLGA sample considered for the molecular dynamics simulations, obtained from a 3×3 supercell. (b) Experimental topography analysis of the PLGA specimen from AFM: representative 20 nm × 20 nm area extracted from the original (c) 100 nm × 100 nm scan. Fig. from Ref. [1].

Table 3.2 Apparent (θ) and Young (θ_Y) contact angles of water and formamide evaluated through the Wenzel theory [34] for different roughness factor (R_f), depending on the acquisition window of AFM analysis and MD surface. Notice that, due to the nonlinearity of the cosine function, the surface roughness does not affect sensibly the surface wetting properties except in the case of low θ, such as the modeled formamide case.

Scan (nm)	R_f	θ_{H2O} (°)	$\theta_{Y,H2O}$ (°)	θ_{CH_3NO} (°)	θ_{Y,CH_3NO} (°)
20 × 20	1.0925	65±4	67	52±4	56
100 × 100	1.1078	65±4	68	52±4	56
500 × 500	1.0570	65±4	66	52±4	54
MD model	1.5250	61.8±3.8	71.9	27.3±5.5	54.3

3.2.3 Wettability of PLGA surfaces

The CAs of the four liquids on the flat PLGA surface are computed and compared against the experimental measurements.

Water

In the case of water droplets, the CA of the SPC-E and the Tip4P-05 models was found to be $61.7° \pm 3.8°$ and $64.6° \pm 5.0°$, respectively, in excellent agreement with the experimental measure of $65° \pm 4°$ (see Figs. 3.5 and 3.6) and previous works from the literature [209]. The relevance of this result is further emphasized by the fact that CA is not a target for parameterization.

The evolution of a water droplet onto the PLGA surface is shown in Fig. 3.5a, where equilibrium conditions are reached after some 500 ps of simulation. The CA is measured during the last 2 ns of trajectory, where the CA oscillates around a stable mean value (see Fig. 3.5b, Tip4P-05 model). The error on the CA is computed by propagating the error on each snapshot due to different choices of δ (see Section 3.1.1). As reported in Fig. 3.6, the average CA obtained with the SPC-E water model and the standard deviation of each snapshot is similar to the Tip4P-05 model, proving the reliability of our numerical protocol regardless of the chosen water model.

The hydrophilic nature of the PLGA sample is also highlighted considering the surface free energy of $43 \pm 3\,\mathrm{mJ/m^2}$ evaluated through the Owen-Wendt method [56]. The experimental uncertainty associated with the contact angle measurements has been propagated through the interpolation terms to evaluate the uncertainty associated with the slope and the intercept of the regression model and, further on, determine the uncertainty of the unknown polar and disperse component of the solid surface. We considered water and formamide as polar probe liquids and diiodomethane as non-polar liquid since it has a finite contact angle on the PLGA surface. Results of this analysis are reported in Tab. 3.3.

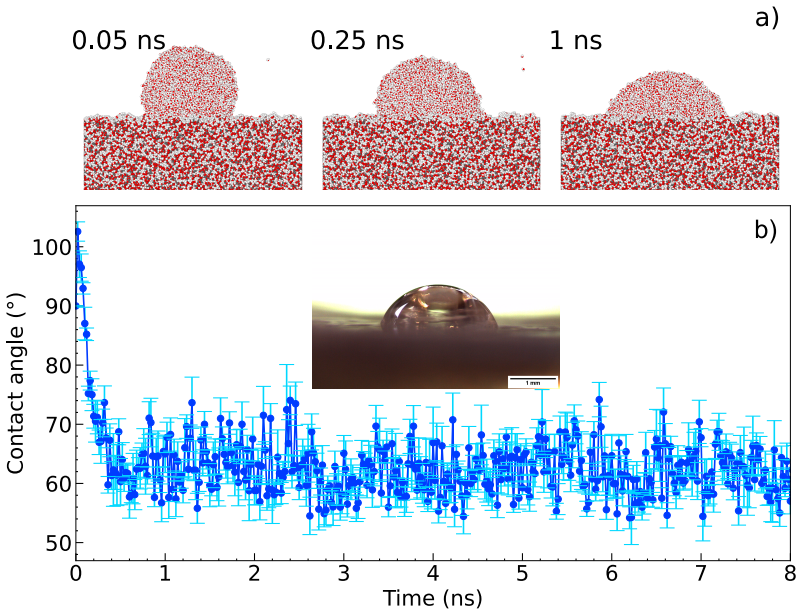

Fig. 3.5 (a) Pictorial view of the Tip4P-05 water droplet evolution during the simulated stabilization on the PLGA surface. (b) Variation of the apparent contact angle during the stabilization and acquisition trajectory. Data acquired over the last 2 ns. The error bars on CA values come from averaging over different values of δ. The inset in b) is the water droplet on the flat PLGA sample from which the experimental CA is evaluated. Fig. from Ref. [1].

Table 3.3 Contact angles and Surface Free Energy (SFE) of flat PLGA sample as obtained from experiments and the Owen-Wendt approach [56]: water (H_2O), formamide (CH_3NO), and diiodomethane (CH_2I_2) are reported as probe liquids. Notice that the measured SFE has a polar component of 12 ± 1 mJ/m^2, while a dispersive one of 31 ± 2 mJ/m^2.

Sample	H_2O (°)	CH_3NO (°)	CH_2I_2 (°)	SFE (mJ/m^2)
PLGA 75:25 (lactic:glycol)	65 ± 4	52 ± 4	50 ± 4	43 ± 3

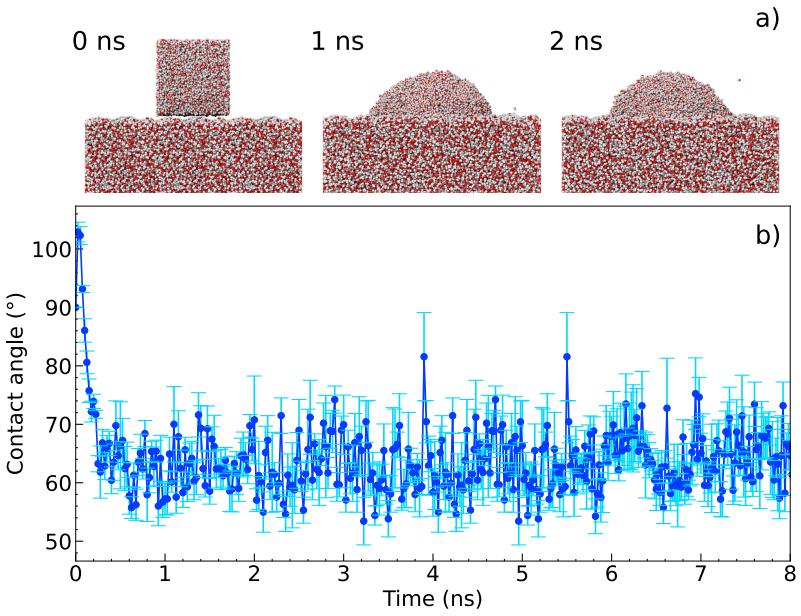

Fig. 3.6 (a) Pictorial view of the SPC-E water droplet evolution during the stabilization on the PLGA surface. (b) Variation of the contact angle during the stabilization and acquisition trajectory. Data acquired during the last 2 ns. Error bars indicate $\pm$ 1 s.d.. Fig. from Ref. [1].

Formamide

In the case of formamide, we observe a mismatch between the computed (27.3° ± 5.5°) and experimental (52° ± 4°, see Fig. 3.7) CA. Considering the Wenzel model, however, the measured apparent CA (27.3°) can be used to extract the Young CA (54.3°), which results in excellent agreement with the experimental value of θ_Y (see Tab. 3.2). Furthermore, given the good solubility of formamide in water, we can assume that atmospheric moisture in the testing environment could be absorbed in the formamide droplet during the experimental measurements. However, the perfectly anhydrous conditions in MD simulations can partially also explain the mismatch between numerical and experimental values of CA for formamide. We tested this hypothesis by performing additional simulations with droplets of formamide containing 10%wt and 20%wt of water, using the same computational procedure (see Fig. 3.8, 3.9 and 3.10). In the first case, we did not observe a significant variation in the evaluated CA, while in the second one, the CA reached its equilibrium at a higher CA value, namely 32° ± 9°.

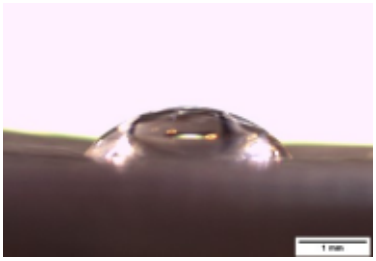

Fig. 3.7 Image of the experimental formamide droplet on the flat PLGA specimen. Fig. from Ref. [1].

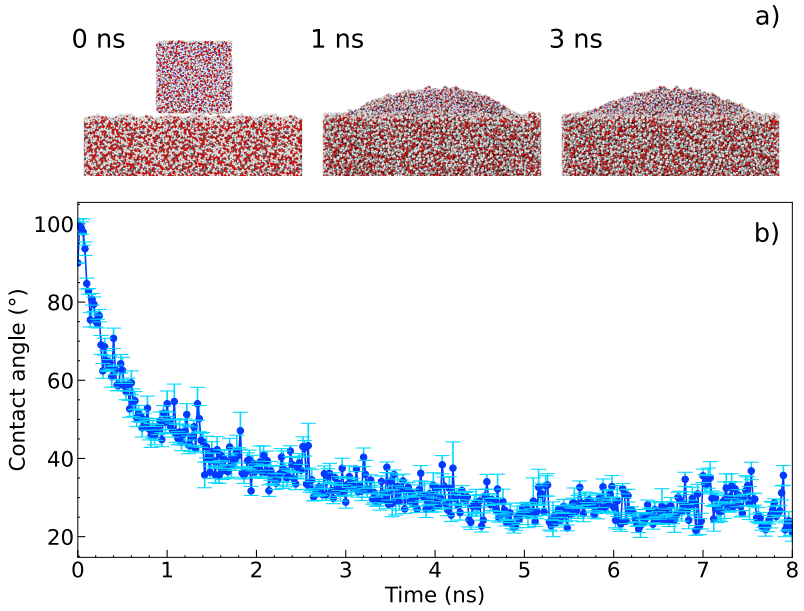

Fig. 3.8 (a) Pictorial view of the formamide droplet evolution during the stabilization on the PLGA surface. (b) Variation of the contact angle during the stabilization and acquisition trajectory. Data acquired during the last 2 ns. Error bars indicate $\pm$ 1 s.d.. Figure from Ref. [1].

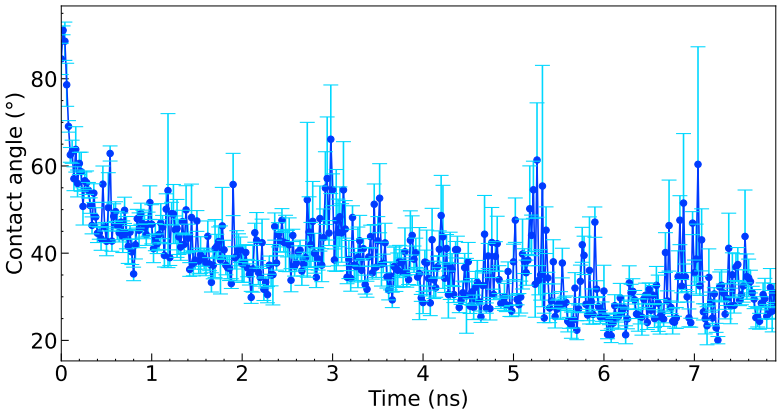

Fig. 3.9 Variation of the contact angle of the formamide droplet with 10 wt% of water during the stabilization and acquisition trajectory. Data acquired during the last 2 ns. Error bars indicate $\pm$ 1 s.d.. Note that the maximum concentration of formamide in water before phase separation is 90 wt% at 298 K and 1 bar. Figure from Ref. [1].

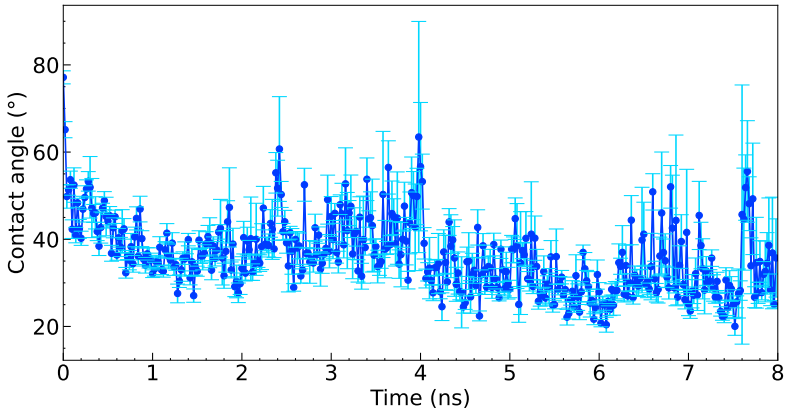

Fig. 3.10 Variation of the contact angle of the formamide droplet with 20 wt% of water during the stabilization and acquisition trajectory. Data acquired during the last 2 ns. Error bars indicate $\pm$ 1 s.d. Fig. from Ref. [1].

Toluene and hexane

In the case of non-polar hydrocarbon liquids, the simulations reproduce the high affinity with the PLGA surface observed experimentally with good accuracy. For toluene, during experiments, we observe a stable contact angle of $23^\circ \pm 5^\circ$ for approximately 15 s before a complete spreading (see Fig. 3.11). MD shows an initial metastable state of the droplet with a CA of $11^\circ \pm 2^\circ$ for approximately 500 ps before a complete spreading is eventually achieved (see Fig. 3.12). Indeed, it is worth noting that toluene is a good solvent of PLGA and that the size of the MD sample is orders of magnitude smaller than the experimental one. Hence a shorter timescale is expected for the interaction between the two phases. In the case of hexane, we observe a complete spreading of the droplet onto the PLGA surface (0°, see Fig. 3.13) after approximately 1.2 ns, yielding the formation of a uniform film. This behavior is confirmed experimentally, where an instantaneous spreading of the hexane droplet is observed. The overall comparison between the computed and experimental CA for the four fluids on PLGA is shown in Fig. 3.14b.

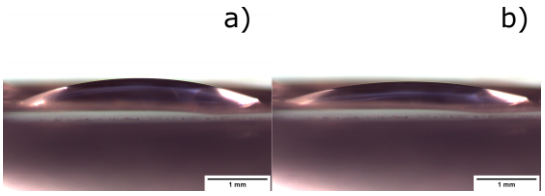

Fig. 3.11 Image of the experimental toluene droplet on the flat PLGA specimen after 6 s (a) and 15 s (b) from deposition. Fig. from Ref. [1].

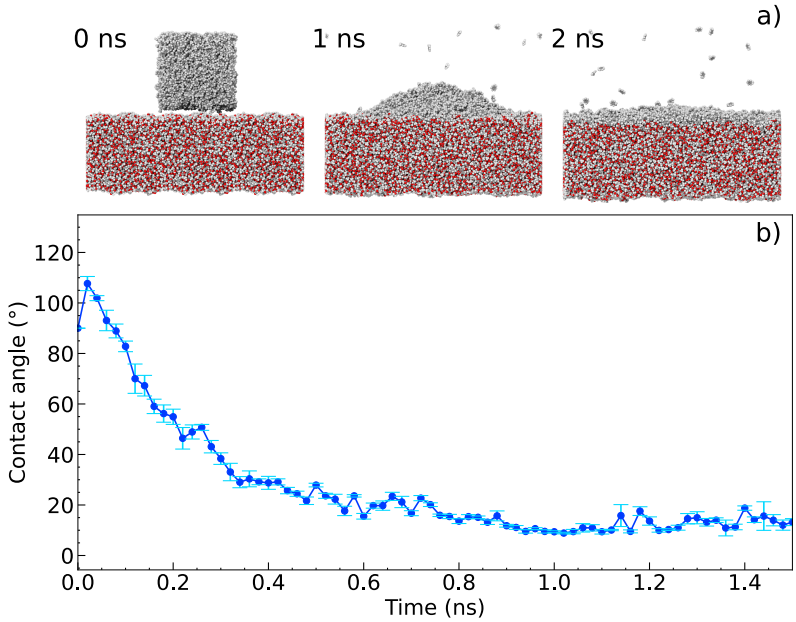

Fig. 3.12 (a) Pictorial view of the toluene droplet evolution during the stabilization on the PLGA surface. (b) Variation of the contact angle during the stabilization and acquisition trajectory. A metastable value of contact angle has been observed between 1000 and 1500 ps, while the complete spreading was achieved after 1500 ps. At such point, the computed CA diverges ($\Delta r = r_1 - r_2 = 0$ and $\theta = \arctan(\Delta z/\Delta r) \longrightarrow \infty$). Error bars indicate $\pm$ 1 s.d. Fig. from Ref. [1].

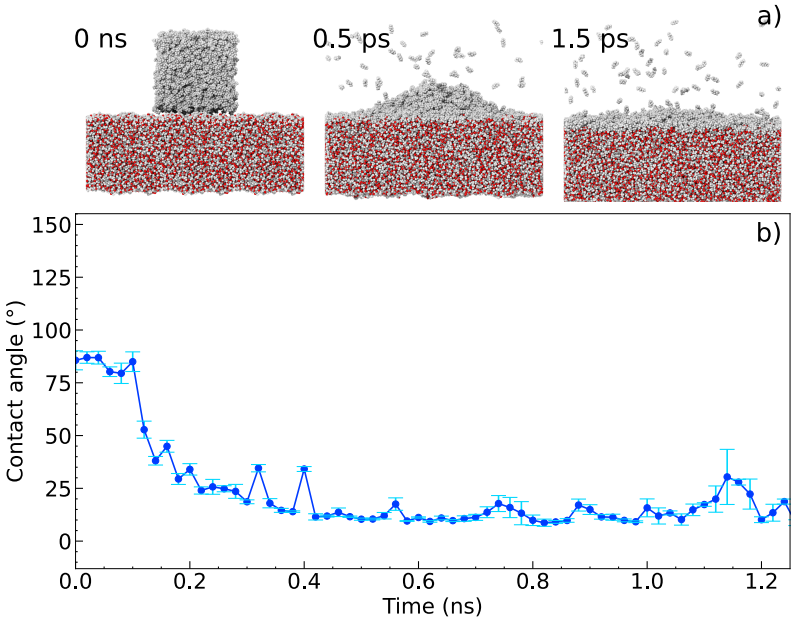

Fig. 3.13 (a) Pictorial view of the hexane droplet evolution during the stabilization on the PLGA surface. (b) Variation of the contact angle during the stabilization and acquisition trajectory. A metastable value of contact angle has been observed between 500 and 1200 ps, while the complete spreading achieved after 1200 ps. At such point the computed CA diverges ($\Delta r = r_1 - r_2 = 0$ and $\theta = \arctan(\Delta z/\Delta r) \longrightarrow \infty$). Error bars indicate $\pm$ 1 s.d.. Fig. from Ref. [1].

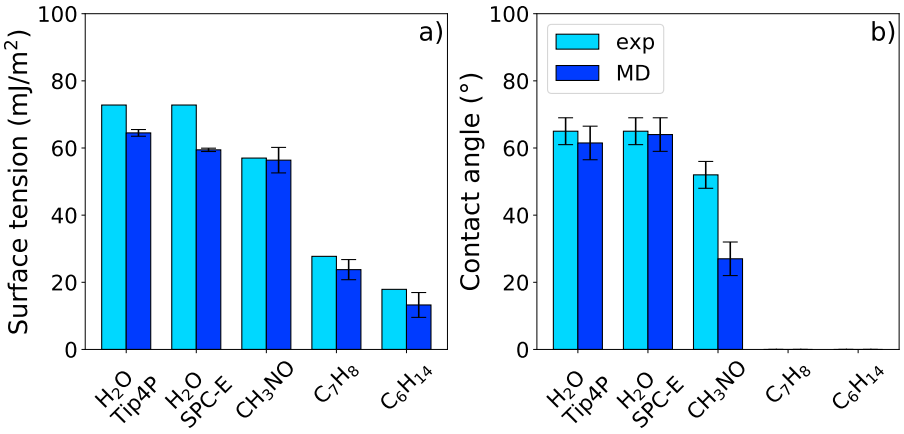

Fig. 3.14 Comparison between experimental and numerical wetting properties of the PLGA and probe fluids. (a) Surface tension of the probe fluids and (b) their apparent contact angles on PLGA. The experimental values of surface tension are taken from Refs. [204, 201–203, 205], while those of CA from measurements carried out in this work. The surface tension from numerical simulations was averaged over 5 ns of acquisition time. The experimental CA was averaged on at least 6 different droplets for each liquid, while the CA from numerical simulations was averaged over 2 ns and different values of δ (see Section 3.1). Fig. from Ref. [1].

3.2.4 Discussion

The main advantage of the numerical method proposed and validated here is to simplify and accelerate the initial stages of material surface design and prototyping, offering an integrated framework that allows predicting the wettability of a wide range of soft interfaces with good accuracy.

However, MD simulations can suffer from artifacts due to finite-size effects [210]. The size of the samples investigated in this work was capped at approximately 350'000 atoms to match the computational resources available. These constraints limit the size of the surface investigated, the maximum roughness that can be realistically modeled on a periodic surface, and of course, the size of the droplet, whose diameter should not exceed half the periodic box vectors. An elegant way of increasing the size of the droplets while keeping the computational cost at a manageable level is by adopting a pseudo-2D model, where the droplet is replaced by a periodic cylinder [64, 65].

Another significant limitation is the timescale accessible through MD simulations, here in the order of 10 ns per sample. With the parameters used in our MD simulations, most samples reach thermodynamic equilibrium within a few nanoseconds unless other phenomena with more long timescales are involved [211–213]. While it cannot be ruled out that the observed droplets were in a metastable state lasting longer than the simulated time, we have verified that the contact angle reaches a consistent equilibrium value for droplets of increasing size. In this work, we have used droplets containing approximately 13'000 molecules to limit finite-size effects and reduce the numerical noise of simulations.

A way to overcome the limitations of atomistic models is to decrease the resolution of the system and its internal degrees of freedom, a process known as coarse-graining. A recently developed coarse-grained model, which reproduces the morphology and density of organic semiconductors [138] and polymers [214], and the structural and dynamic properties of water [2] in quantitative agreement with atomistic MD simulations, will be discussed in the following Chapters 5 and 6. There, a CG model for water and PLGA will be implemented, validated, and finally applied to predict the wetting behavior of soft interfaces, addressing the known limitations of atomistic models but without compromising on the quality of the predicted properties.

This considered, the evaluation of water droplet size-dependent behavior on hydrophilic surfaces from literature data [215] reported that a remarkable effect of surface asperities, within the micro-state pinning behavior, is such that a narrowing of contact angle evaluated error from MD simulations occurs for a nano-scale roughened surface. This is in accordance with the authors' preliminary evaluations for the specific selection of the simulated sessile droplet volume (while roughness itself determines an increase in the CA mean value). As, however, in accordance with experimental data stated throughout this work, it is worth highlighting that our modeling activities reached the pinning state equilibrium.

3.3 Further perspectives

In this work, we reproduced sessile droplet experiments with molecular dynamics simulations, proposing a methodological procedure for predicting the wettability of soft interfaces. In detail, we studied Poly(Lactic-co-Glycolic Acid) surfaces wetted by polar and non-polar solvents (water, formamide, toluene, and hexane) and validated the obtained results with experiments.

We initially evaluated the surface topography of the MD and experimental samples through the solvent accessible surface and AFM, respectively. Both numerical and experimental surfaces present an RMS roughness smaller than 10 Å, while the roughness factor (R_f) is between 1.0570 and 1.1078 in the experimental samples and 1.5250 in the MD sample. According to the Wenzel theory, the local or Young contact angle can be assessed with droplet experiments under these conditions since negligible effects from surface topology are expected. For the numerical model, the surface topology may affect the measurement of liquids that present a low apparent contact angle, such as formamide. The glass transition temperature of bulk PLGA and the surface tension of the probe liquids computed from MD simulations were found to be in excellent agreement with the experimental evidence, thus validating the force field chosen to describe the materials in this study. Finally, we performed the sessile droplet experiment, leaving a droplet of solvent to relax onto the PLGA surface and then measuring the apparent contact angle by post-processing the MD trajectory. The results obtained agree with the experimental measures, therefore supporting the proposed protocol. In the case of water droplets, both the SPC-E and the Tip4P-05 models show excellent agreement with experiments. With the

formamide model, we observe a reduction of approximately 30% with respect to the experimental CA: we attributed this mismatch to the effects of the roughness factor (R_f) according to the Wenzel theory and the perfectly anhydrous conditions in the MD simulations of formamide droplets, differently from the testing environment. The MD simulations predict a strong affinity of non-polar solvents with the polymer surface, which was confirmed by the experimental measurements. Toluene spreads over the PLGA surface after a transient metastable state, whereas the hexane droplet spreads immediately.

This work is a relevant case study of convergence and synergy between digital and experimental measurements towards a new class of hybrid characterization standards (e.g., coupled MODA [216] and CHADA [217] workflows). In perspective, the proposed methodology will speed up the development of soft interfaces with controllable wetting properties. The protocol presented in this work has been shown to accurately predict the CA of polar and non-polar solvents on a soft polymeric surface. This information can be used as a boundary condition in continuum simulations able to assess the effect on wettability produced by modifications of the surface topology at the nano- and micro-scales, thus connecting the property of materials at the device level with their underlying molecular structure.

With this goal in mind, this work represents the first step towards the creation of a multi-scale model able to predict and optimize the wettability of micro-structured soft surfaces, for instance, by providing fast and accurate values of the local or Young contact angle, which in turn can be used as a boundary condition in multi-phase continuum models (e.g., finite-elements or finite-volume simulations).

Chapter 4

Wettability of graphene surfaces predicted by the free energy perturbation

In this Chapter, we present and validate an MD protocol for evaluating properties of the graphene/water interface, adopting the so called thermodynamics route based on the free energy perturbation (FEP) approach [218]. This method has been recently introduced and implemented in the popular materials modeling code LAMMPS [175, 176], demonstrating the growing interest of the MD community in interface wetting phenomena. In detail, we:

1. Evaluate the W_{ad} and interface tension (γ_{sl}) at the graphene/water interface for a single-layer graphene system.

2. Investigate the influence of different graphene/water interaction models on wetting properties, comparing and selecting the most suitable candidate based on existing literature.

3. Explore the wetting properties of multi-layer graphene, specifically three and five-layer configurations.

4. Compare and validate the proposed model with experiments conducted on single-layer and multi-layer graphene samples deposited onto SiO_2 substrate.

This approach can be extended beyond the specific study case discussed here to investigate wetting phenomena on different surfaces and in various liquid environments. Furthermore, the values of W_{ad} and γ_{sl} can be used as boundary conditions to describe both the static and dynamic behaviors of wetting phenomena at the continuum level. Hence, in perspective, the work discussed in this Chapter represents a second fundamental step of an integrated multi-scale model for wetting phenomena, that can couple the nano- to the macro-scale.

4.1 Materials and methods

In this section we describe the computational methods adopted for the evaluation of wettability properties of 2D materials such as graphene, following a thermodynamic route, namely the free energy perturbation approach (FEP).

4.1.1 Model building

We performed MD simulations using LAMMPS [175, 176] with a time step of 1 fs and the Verlet integration scheme. The graphene sheet was treated as a rigid layer of honeycomb-structured carbon atoms, and we employed the flexible three-point charge SPC/Fw model [219] to describe water molecules. The adoption of a flexible model is necessary for the implementation of the FEP/test area approach, according to the recently developed method in LAMMPS [218].

We used a cutoff distance of 1.2 nm to compute non-bonded interactions, and we employed the PPPM method with 10^{-6} accuracy for the long-range electrostatic interactions [174]. In accordance with the water model, we neglected intramolecular pair interactions and intermolecular hydrogen-hydrogen interactions, while accounting for intermolecular oxygen-oxygen interactions between different water molecules and oxygen-carbon interactions between water molecules and graphene using the Lennard-Jones potential:

$$U_{LJ}^{CO}(r) = 4\varepsilon_{CO}\left[\left(\frac{\sigma_{CO}}{r}\right)^{12} - \left(\frac{\sigma_{CO}}{r}\right)^{6}\right]. \tag{4.1}$$

We employed three different pairs of Lennard-Jones parameters, ε_{CO} and σ_{CO}, taken from Werder *et al.* [97], to investigate hydrophilic, neutral, and hydrophobic configurations of the graphene/water interface. Indeed, at the experimental level, the graphene CA has been reported in the range of 45°-127° [87] (see Section 1.2.1). Additionally, we adopted a potential obtained by applying the geometric mixing rule between the OPLS-AA [164] parameters for aromatic carbons and the SPC-Fw water model:

$$\varepsilon_{CO} = \sqrt{\varepsilon_C \varepsilon_O}, \tag{4.2}$$

$$\sigma_{CO} = \sqrt{\sigma_C \sigma_O}. \tag{4.3}$$

Lastly, for comparison with previous studies [39, 40], we used a model whose cross-interactions between graphene and water were calculated with the Lorentz-Berthelot mixing rule between the carbon parameters of Dreher *et al.* [39] and the SPC-Fw water model:

$$\varepsilon_{CO} = \sqrt{\varepsilon_C \varepsilon_O}, \tag{4.4}$$

$$\sigma_{CO} = \frac{1}{2}(\sigma_C + \sigma_O). \tag{4.5}$$

In Tab. 4.1 we reported a summary of the cross-interaction parameters adopted for the water-graphene interface.

We generated the initial graphene structure using VMD [220], while input LAMMPS data and files with Moltemplate [137]. We built a symmetric liquid-solid-liquid (LSL) and an asymmetric liquid-solid-vacuum (LSV) configuration to describe the graphene/water interface (see Figs. 4.1a–b for details). In the former case, the graphene sheet was placed at the center of the simulation box, with two reservoirs of water surrounding it in the z direction. In the latter case, only one water reservoir was placed above the graphene sheet, leaving vacuum slabs beneath the graphene layer and at the top of the water phase. In both cases, periodic boundary conditions were applied in all three directions. The cross-sectional area was defined as $A = L_x L_y$, where $L_x = L_y = 72$ Å, and the box lengths in the z direction were 210 Å and 140 Å for the LSV and LSL systems, respectively.

The LSL system was relaxed in the NPT ensemble at 298 K and 1 atm (with coupling constants of temperature and pressure set to 100 ps and 1000 ps, respectively) until equilibrium in energy and density was achieved, which typically took around 2 ns. The average density was then computed along a trajectory of 1 ns in the NPT ensemble, and a subsequent equilibration run of 1 ns was performed in the

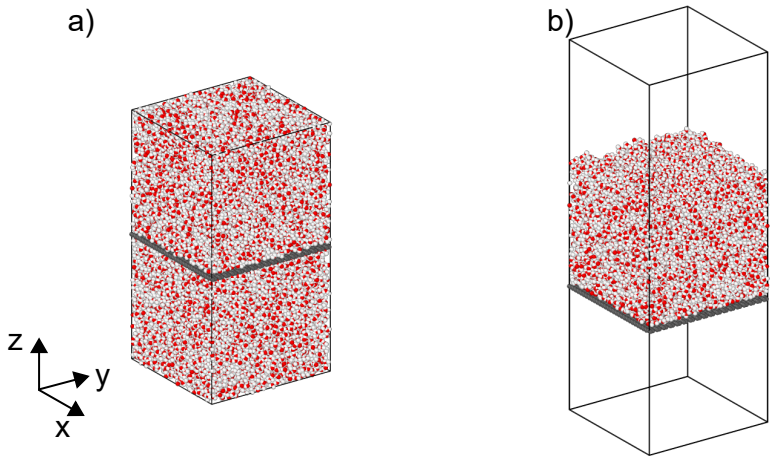

Fig. 4.1 (a) Asymmetric liquid-solid-vacuum (LSV) graphene/water interface model with box dimension 37x37x210 Å^3; (b) symmetric liquid-solid-liquid (LSL) graphene/water interface model with box dimension 37x37x140 Å^3.

Table 4.1 Water/graphene models studied with different LJ cross-interaction (ε_{CO} and σ_{CO}) parameters between the two phases. Evaluated work of adhesion (W_{ad}), interface tension (γ_{sl}) and friction coefficient (f) for monolayer graphene systems

Model	$\varepsilon_{CO}(kcal/mol)$	σ_{CO} (Å)	W_{ad} (mN/m)	γ_{sl} (mN/m)	$f(mPa \cdot s/m)$
1[a]	0.1199	3.19	91.2±0.1	93.6±1.1	73972.8
2[b]	0.1155	3.28	96.3±0.3	93.2±2.4	56039.2
3[a]	0.1049	3.19	75.9±0.7	89.4±1.8	51511.2
4[c]	0.1043	3.35	90.0±0.3	90.3±3.7	43805.4
5[a]	0.0937	3.19	64.7±0.4	86.4±1.3	45140.8
6[a]	0.0749	3.19	46.8±1.1	82.1±3.3	27508.1

[a] Parameters from the work of Werder *et al.* [97]

[b] Lorentz-Berthelot mixing rule between SPC-Fw water model and aromatic carbon atoms from Dreher *et al.* [39]

[c] Geometric mixing rule between SPC-Fw water model and OPLS [164] aromatic carbon atoms

NVT ensemble. The LSV system, on the other hand, was relaxed directly in the NVT ensemble at 298 K until equilibrium, which typically required 2 ns.

4.1.2 Evaluation of the water surface tension γ_{lv} and solid-liquid interface tension γ_{sl}

We applied the FEP approach to evaluate the surface tension of water and the solid-liquid interface tension, γ_{sl}. γ_{sl} represents the excess free energy due to the formation of an interface. According to the FEP approach, it can be calculated in numerical simulations as the free energy variation resulting from a small perturbation of the cross-sectional area of the interface by changing the simulation box dimensions at constant volume. For this reason, this method is also known as the test area (TA) method. The value of the interface tension can be calculated with Eq. 2.40 [221, 222]:

A more accurate evaluation of the interface tension is obtained by calculating the average value after applying both positive and negative perturbations [221] (see Fig. 4.2a) as follows:

$$\begin{aligned}\gamma_{sl} = &\frac{-k_B T}{\Delta A} \ln \left\langle \exp\left(-\frac{U_{tot(1)} - U_{tot(0)}}{k_B T}\right)\right\rangle_0 - \\ &\frac{-k_B T}{\Delta A} \ln \left\langle \exp\left(-\frac{U_{tot(-1)} - U_{tot(0)}}{k_B T}\right)\right\rangle_0 .\end{aligned} \tag{4.6}$$

Here $U_{tot(1)}$ and $U_{tot(-1)}$ are the configurational energies associated with the positive and negative perturbed states, respectively. We implemented the TA method by multiplying both the box dimensions along axes of the interface area (i.e., x and y) by a scale factor of $\alpha^{1/2}$ and dividing dimension along the remaining dimension (i.e., z) by α to preserve the total volume of the simulation box. We chose $\alpha = 1 \pm \xi$, with $\xi = 0.0001$ [221]. As observed by Müller *et al.* [223], perturbations that are too small induce changes in energy that are of the order of machine precision, while perturbations that are too large produce overlaps among the molecules and a deviation from the expected linear regime. As a general rule, α is assumed to be in the range of 10^{-7} to 10^{-2} [223]. An example of a LAMMPS script for computing the γ_{sl} is provided in Appendix A.2.1.

The surface tension of water (γ_{lv}), instead, was computed applying both positive and negative perturbations every 1 ps over a trajectory of 10 ns. We considered a system composed of 1000 water molecules placed in a box with dimensions of 30 x 30 x 90 Å^3 in the x, y, and z directions, respectively, ensuring a vacuum on the top and bottom of the water phase (see Fig. 4.3a for details).

4.1.3 Evaluation of work of adhesion (W_{ad})

The work of adhesion (W_{ad}) was evaluated using the free energy perturbation (FEP) approach [67, 224]. W_{ad} corresponds to the energy required to separate two phases in contact. According to the FEP approach, W_{ad} can be evaluated in numerical simulations as the work required to convert the solid-liquid interface into a non-attractive interface by progressively reducing the cross-interaction potential (see Fig. 4.2b), as expressed by Eq. 2.41. We implemented the FEP approach by reducing the solid-liquid interaction potential within $n = 20$ steps along a trajectory of 16 ns in the NVT ensemble. During each step, 500 ps were devoted to relaxing the system and 300 ps to acquiring the average potential energy. The coupling parameter λ (see Eq. 2.42) is varied with intervals of $\delta\lambda = 0.5$ from 1 (full solid-liquid interaction) to 0 (non-attractive interaction). To this end, we adopted a soft potential to describe the interactions between graphene and water (see Section 2.3.5 for further details). We evaluated the W_{ad} only for the LSV model. An example of a LAMMPS script for computing the W_{ad} is provided in Appendix A.2.2.

4.1.4 Friction coefficient and slip length

To completely characterize the solid-liquid interface, and to provide a complete set of boundary conditions for continuum simulations (see Section 1.2.1), we computed the friction coefficient between graphene and water. This parameter is correlated to the slip length of water on graphene through the viscosity of the liquid [225]:

$$b = \frac{\eta}{f}, \tag{4.7}$$

where, b is the slip length, η is the viscosity of water, and f is the friction coefficient. The friction coefficient can be evaluated through the auto-correlation function (ACF) of the off-diagonal components of the forces between water and graphene as expressed by the Green-Kubo equations during an equilibrium MD simulation [225]:

$$f = \frac{1}{2Ak_BT}\int_0^\infty \langle \mathbf{f}_t(t)\cdot\mathbf{f}_t(0)\rangle dt, \tag{4.8}$$

where, A is the interface area, k_B is the Boltzmann constant, T is the absolute system temperature, $\mathbf{f}_a$ is the transverse force vector between water molecules and graphene, while the brackets indicate an ensemble average and $\cdot$ denotes a dot product.

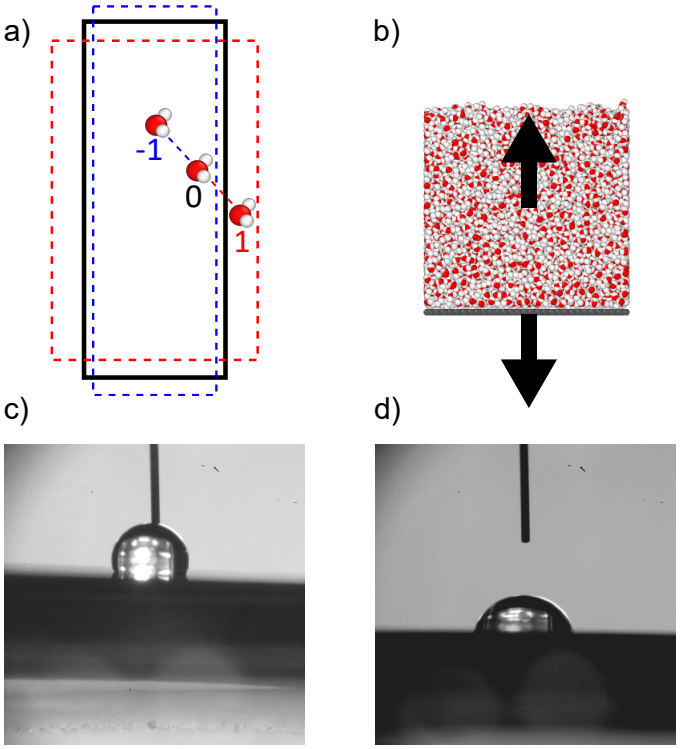

Fig. 4.2 Numerical and experimental protocols for the evaluation of work of adhesion (W_{ad}) and interface tension (γ_{sl}). (a) Implementation of the FEP approach for γ_{sl} by positively and negatively varying the interface area while keeping the volume of the simulation cell constant. The solid line indicates the non-perturbed state (0), while red and blue dashed lines indicate the positive (1) and negative (-1) perturbed states, respectively. The positions of atoms in the simulation cell are displaced accordingly to the deformation of the box. (b) Implementation of the FEP for W_{ad}. The liquid film is separated from the substrate along the direction perpendicular to the interface, as indicated by arrows. The interactions between graphene and water are progressively tuned off, transforming the interface into a non-attractive interface. (c) Advancing contact angle experiment (needle method, see Section 2.2.2) to evaluate the graphene/water γ_{sl}, and (d) static contact angle experiment to evaluate the graphene/water W_{ad}.

Similarly, we evaluated the viscosity of water using the Green-Kubo relation [169].

$$\eta = \frac{V}{k_B T} \int_0^\infty \langle P_t(0) \cdot P_t(t) \rangle dt, \tag{4.9}$$

where V is the volume and P_t are the off-diagonal elements of the pressure or stress tensor. The auto-correlation functions (ACFs) for both properties are calculated every 2 fs using an integration time step of 1 fs. The upper limit of the integral is set to 16 ps and 8 ps for f and eta, respectively. Trajectories of at least 10 ns were used to acquire data.

4.2 Results and discussion

The characterization protocol discussed in this chapter utilizes the FEP approach along with MD simulations to predict the wetting properties of graphene. In this section, we initially present the preliminary results obtained to validate the water model used, as well as the method employed to evaluate the interface tension. Next, we present the results of single-layer graphene models based on various interaction parameters with water and also explore the potential effects of system structure. Finally, we discuss the wettability of multi-layer graphene models, compare the results with experimental data to validate the proposed model, and provide insights into the semi-transparency effect of graphene coatings.

4.2.1 Surface tension of water

Firstly, we evaluated the water surface tension using the FEP approach described in the previous section. In Fig. 4.3b, we report the cumulative average over a trajectory of 10 ns of the surface tension. The blue and orange lines represent the surface tension values evaluated through the FEP approach and the Irving-Kirkwood method, respectively. The two values are in good agreement with each other, as the difference is bounded within the error bars (60.5 ± 1.7mN/m and 59.2 ± 1.4mN/m for the TA and IK methods, respectively). The result obtained is also in good agreement with the literature on other SPC-based water models [204].

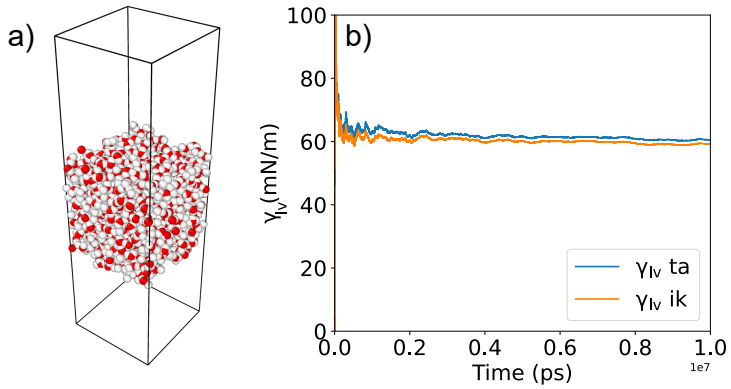

Fig. 4.3 (a) Simulation box of water to evaluate the surface tension. The system is composed of 1000 water molecules deposited in a simulation box with dimensions 30x30x90 Å^3. (b) Cumulative average of surface tension of water γ_{lv} evaluated through the test-area method (blue line) and Irving-Kirkwood relation (orange line).

4.2.2 Single-layer graphene

In Fig. 4.4, we present the density profile associated with the different models adopted, based on various cross-interaction parameters. Both the LSL and LSV models (Figs. 4.1a–b, respectively) show a less structured layering of water in the proximity of graphene while reducing the intensity of the cross-interaction parameter ε. Consistent with the density profile, for models 1, 3, 5, and 6, we observe a progressive reduction of W_{ad} with the reduction of ε, corresponding to an increase in hydrophobicity (see Fig 4.5). Indeed, W_{ad} is related to the contact angle through the Young-Dupré equation:

$$\theta = \arccos\left(\frac{W_{ad}}{\gamma_{lv}} - 1\right). \tag{4.10}$$

In the case of models 2 and 4, we obtained higher values of W_{ad} compared to model 1, despite lower values of ε (see Fig 4.5). This can be attributed to the higher value of σ of these two models compared to the other ones, which affects the interaction between the two phases. Assuming the previously calculated surface tension of water, the contact angle of water onto graphene is in the range of 65°-110°, consistent with previous MD studies that adopted the same or similar interaction parameters [67, 97, 39]. Overall, the first four models express a hydrophilic nature, while models 5 and 6 represent neutral and hydrophobic configurations, respectively.

In the case of γ_{sl}, we first validated the protocol adopted by comparing the result of model 2 with the result reported in the work of Dreher *et al.* [39], being the cross-

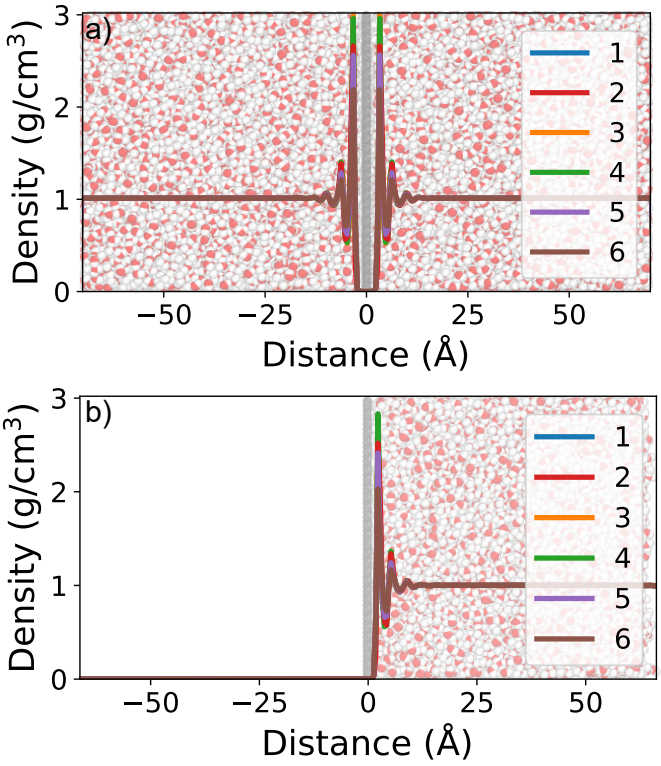

Fig. 4.4 Water density profile of (a) symmetric LSL and (b) asymmetric LSV systems at the graphene water interface. Colors indicate different graphene/water models depending on different interaction parameters (see Tab. 4.1 for a detailed description of the employed parameters.)

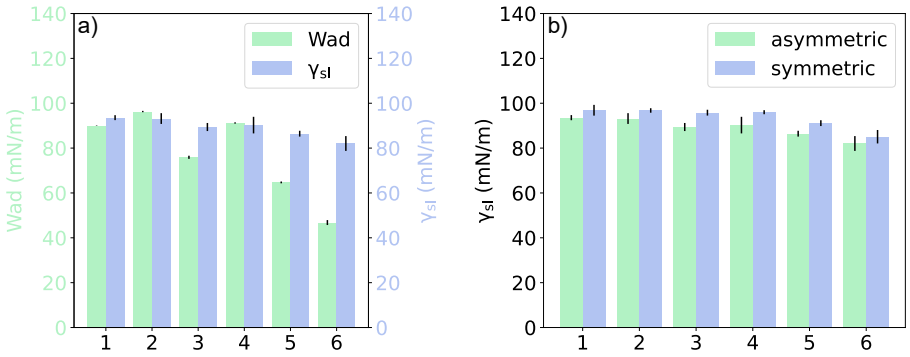

Fig. 4.5 (a) Graphene/water interface W_{ad} and γ_{sl} for different models studied. (b) Variation of γ_{sl} between asymmetric LSV and symmetric LSL systems.

interaction parameters calculated starting from the same carbon atoms LJ parameters: the calculated value (93.2 $\pm$ 2.4 mN/m) is in good agreement to the value reported in their work (102.5 $\pm$ 3 mN/m). The slight difference is attributed to the different water adopted (SPC-Fw in this work and Tip4P-05 in their work). We then compared the possible effects of the model structure (LSL and LSV) on the interface tension at the water-graphene interface. In the case of the LSL model, we divided the value obtained from equation 4.6 by two to account for the presence of two interfaces across the graphene sheet. In the case of the LSV model, we subtracted the value of water surface tension from the one evaluated with equation 4.6 to take into account the presence of the graphene-water interface and free surface of the water. In Fig. 4.5, we compared the interface tension between LSL and LSV systems for all the simulated models. For models 1, 2, and 6 the difference is bounded into the error bars. However, in all cases, we observed a slight reduction in the average value of the interface tension in the LSV systems compared to the LSL ones. The difference observed can be explained by considering the interactions between water molecules across the interface in the case of symmetric systems.

Considering different models depending on the cross-interaction parameters adopted, the γ_{sl} slightly decreases with hydrophobicity, consistent with W_{ad} (see Fig. 4.5b for the LSL and LSV systems and Tab. 4.1). The transient values of γ_{sl} are reported in Figs. 4.6a–b, highlighting the substantial convergence of simulations.

By adopting the Duprée equation $W_{ad} = \gamma_{sv} + \gamma_{lv} - \gamma_{sl}$ (see Eq. 2.7 in Section 2), which expresses the free energy balance between two phases in contact, we were able to estimate the surface free energy (γ_{sv}) of a pure graphene layer. From the

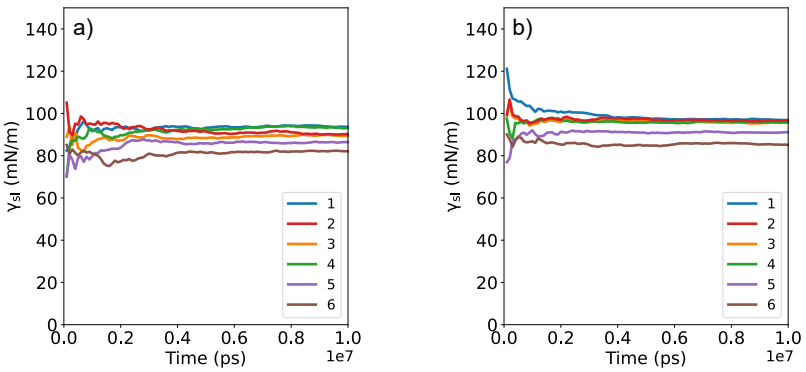

Fig. 4.6 Cumulative average of γ_{sl} along a trajectory of 10 ns for the (a) asymmetric LSV and (b) symmetric mono-layer models.

three most hydrophilic models (1, 2, and 4), we obtained a value in the range of 119-129 mN/m. In the case of model 3, we obtained a value of 104.8 mN/m, while for models 5 and 6 we obtained a value of 91 mN/m and 67.5 mN/m, respectively. The reduction in surface free energy is consistent with the reduction in wettability of these models, as also observed for other low free energy surfaces [70].

4.2.3 Multi-layer graphene and experimental validation

Then, we studied multi-layer graphene systems. Due to the high computational power required for these simulations, we focused on models 3, 4, and 5, being the three most different examples studied in the previous section. Furthermore, we considered LSV systems only, with 3 and 5 layers. For all three models, the W_{ad} increases as the number of graphene layers increases (see Fig. 4.7a and Tab. 4.2). Consequently, multi-layer graphene systems are more wettable than monolayer ones, thanks to the increment of interacting graphene layers with water. On the other hand, γ_{sl} decreases in multi-layer models compared to monolayer ones (see Fig. 4.7b and Tab. 4.2), with an asymptotic trend. The transient values of γ_{sl} are reported in Fig. 4.8, highlighting the substantial convergence of simulations. Similar behaviors were observed by Chiricotto *et al.* while exploring γ_{sl} using the mechanical route MD simulations for mono- and multi-layer graphene sheets [40].

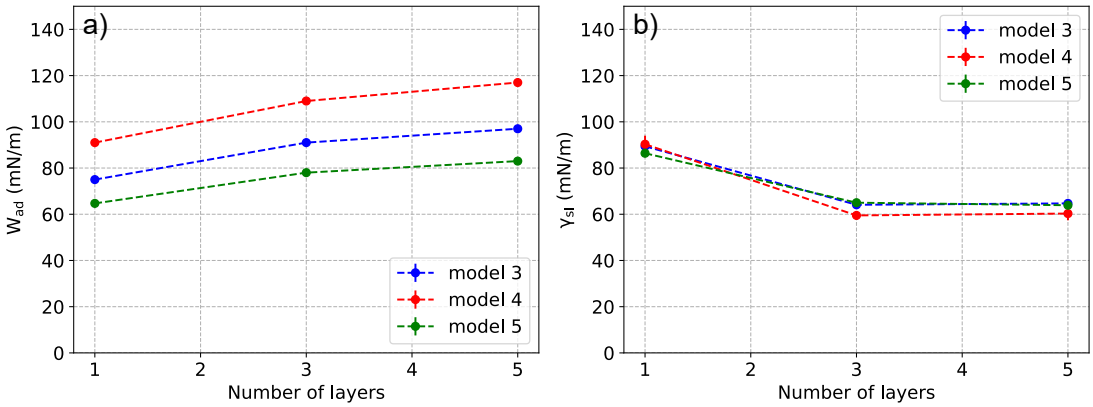

Fig. 4.7 Water/graphene interface W_{ad} and γ_{sl} for multi-layer models

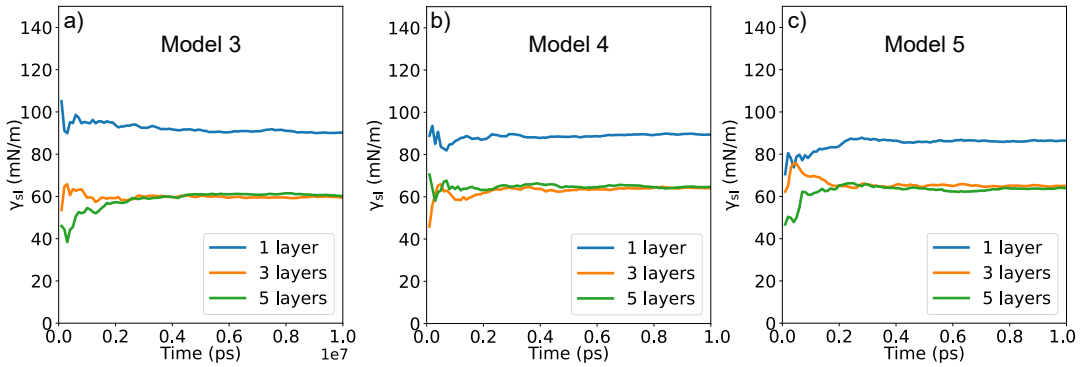

Fig. 4.8 Cumulative average of γ_{sl} along a trajectory of 10 ns for the LSV multi-layer systems based on models 3 (a), 4 (b), and 5 (c)

Table 4.2 Work of adhesion W_{ad} and interface tension γ_{sl} of mono- and multi-layer graphene/water interface for the models 3, 4, and 5 and experiments on single and 2/3 layers supported graphene.

Model / Layers	W_{ad} (mN/m)	γ_{sl} (mN/m)
3 / 1L	75.9±0.7	89.4±1.8
3 / 3L	91.3±0.2	64.1±1.5
3 / 5L	97.1±0.5	64.7±1.4
4 / 1L	91.2±0.3	90.3±3.7
4 / 3L	109.4±0.1	59.5±1.9
4 / 5L	117.1±0.3	60.3±2.9
5 / 1L	64.7±0.4	86.4±1.3
5 / 3L	78.0±0.9	65.0±0.6
5 / 5L	83.1±0.6	63.9±2.4
exp / 1L	102.0±1.2	78.3±2.3
exp / 2L	91.1±1.1	55.2±1.3
exp / 3L	80.8±1.4	36.9±1.8
exp / 5L	78.4±1.2	36.7±1.5

Finally, to validate the proposed model, we compared our numerical predictions with experiments performed on single-, bi, three, and five-layer graphene sheets deposited onto silicon oxide (SiO_2) wafers. The samples were characterized in terms of Raman spectroscopy to ensure the exact number of layers of samples and AFM analysis to evaluate their average roughness. Raman spectroscopy AFM analysis ensured the exact layer composition and the nanoscopically flat nature (roughness in the range of 4-6 nm) of samples, ensuring the validity of comparing our models with samples. The results in terms of W_{ad} and γ_{sl} are summarized in Tab. 4.2, while shown and compared with numerical results of model 5 in Figs. 4.9a–b. Differently from what was observed with MD simulations, multi-layer graphene samples result in less wettable than monolayer ones with a reduction of W_{ad} of around 10%. The inversion in the trend between MD simulations and experimental results highlights the effects of graphene wetting transparency with respect to the substrate (see Fig. 4.9a). SiO_2, indeed, expresses a water static CA of 41° which corresponds to a W_{ad} of 126 mN/m [64], enhancing the hydrophilicity of the sample. The values of W_{ad} for the 3- and 5-layer models are bounded into the error bar, thus highlighting an asymptotic trend. As a consequence, while adding more graphene layers, the effect of the substrate becomes negligible, as also recently observed in previous works in the literature [90, 89, 226, 227]. Interestingly, we observe a convergent trend when comparing the W_{ad} between free-standing graphene studied at the numerical level and supported graphene studied at the experimental level, thus supporting the hypothesis of graphene wetting transparency. Further analysis, like applying the DLVO theory [90, 228] and developing an MD model with SiO_2 substrate, will be carried out to evaluate the effect of the substrate on graphene wetting properties.

On the other hand, γ_{sl} decreases as the number of graphene layers increases for both numerical and experimental results (see Fig. 4.9b). However, a substantial shift between numerical and experimental results is observed. We attributed such a difference to the possible effect of the polar nature of SiO_2 substrate that affects mostly the motion of the contact line and thus the advancing CA, which is correlated to γ_{sl} through the Makkonen relation [103]. Also in this case, an MD model with SiO_2 substrate will be developed to evaluate possible effects of the substrate in the γ_{sl} value.

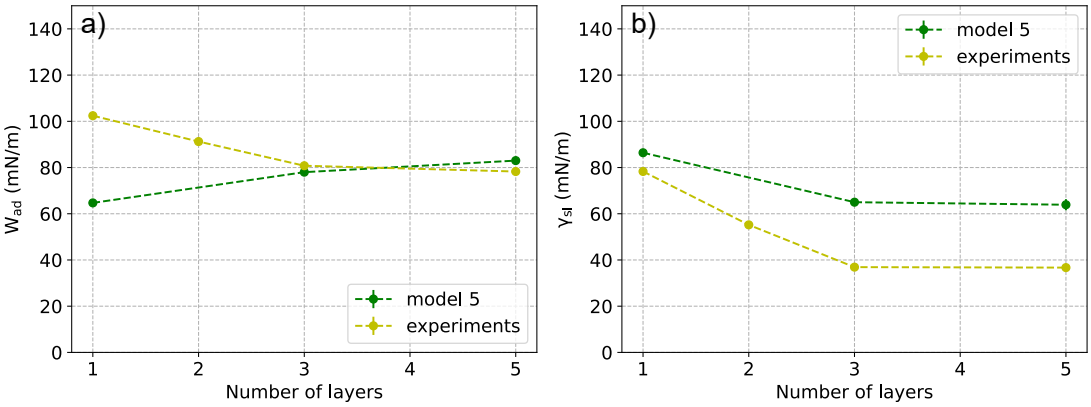

Fig. 4.9 Water/graphene interface W_{ad} and γ_{sl} for multi-layer models (model 5) compared with experimental results

4.2.4 Friction coefficient

Finally, in the context of a multi-scale model that can span from atomistic details to the continuum level, we also evaluated the friction coefficient and slip length at the graphene/water interface, which can be used as parameters for a generalized Navier boundary condition. In Fig. 4.10a, we report the viscosity of water (0.81 mPa s), which agrees well with previous numerical and experimental results (0.75 mPa s and 0.85 mPa s, respectively) in the literature and with experimental evidence [219]. In Fig. 4.10b, we report the friction coefficient calculated for different water/graphene interfaces depending on the cross-interaction parameters. The results obtained are in good agreement with previous MD results in the literature (9.6 x 10^4 Pa s/m) obtained with different water models [229]. Interestingly, despite the similarities in W_{ad} and γ_{sl} among the OPLS, Dreher, and hydrophilic models, the hydrophilic model reports a higher value of the friction coefficient.

4.3 Further perspectives

In this chapter, we employed molecular dynamics (MD) simulations to investigate the characteristics of the graphene/water interface. Graphene was chosen as the focus of our study due to its significant role in various industrial applications. Furthermore, it has been observed in numerous studies that the wetting properties of graphene

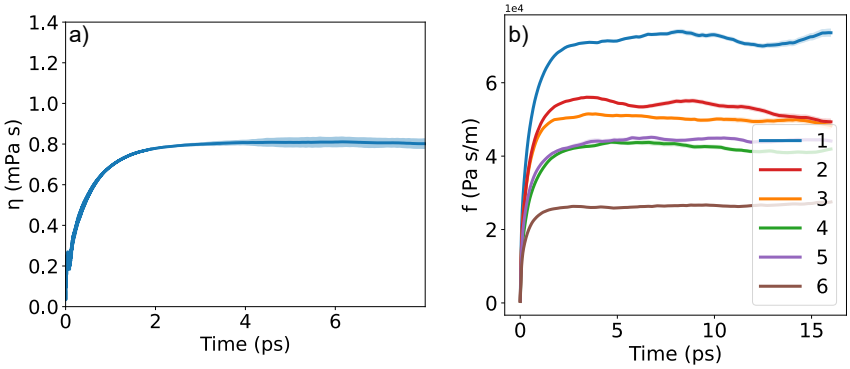

Fig. 4.10 (a) Viscosity of SPC-fW water model and (b) friction coefficient at the water/-graphene interface

strongly depend on the experimental conditions, as highlighted by Belyaeva *et al.* [87]. Consequently, the characterization of the graphene surface remains an unresolved challenge. As suggested by Leroy *et al.* in their seminal paper [67], the evaluation of W_{ad} using the free energy perturbation (FEP) approach in MD simulations provides a promising method for determining the water contact angle (CA) that is less influenced by the specific water model chosen. However, the value of W_{ad} alone does not offer a comprehensive characterization of the water/graphene interface. To fully understand a solid-liquid interface, also the solid-liquid interface tension γ_{sl}, must be considered.

Unlike previous works where only W_{ad} or γ_{sl} were calculated separately, with the missing value obtained from literature data [67, 39, 40], we took a different approach in this study. We employed the free energy perturbation (FEP) method to simultaneously evaluate both W_{ad} and γ_{sl}. By utilizing the surface tension of the probe liquid and assuming flat surfaces, this approach enabled us to comprehensively characterize the solid surface according to the Young-Duprée equation.

In our study, we investigated various models representing different cross-interaction parameters between graphene and water, which spanned from hydrophilic to hydrophobic representations of the solid surface. Subsequently, we examined multi-layer graphene models, observing the changes in the work of adhesion (W_{ad}) and interfacial tension (γ_{sl}) with an increasing number of graphene layers. Our findings revealed that as more layers of graphene were added, there was an increase in W_{ad} and a reduction in γ_{sl}, indicating an effect of multi-layer graphene on the solid-liquid interface properties.

To validate our model, we conducted experimental tests involving sessile droplet and inflation droplet techniques on mono- and multi-layer graphene samples with silicon oxide (SiO2) deposition. These experiments allowed us to evaluate the static contact angle (θ_s) and advancing contact angle (θ_a), which are related to the work of adhesion (Wad) and interfacial tension (γ_{sl}). The experimental results demonstrated a decrease in both W_{ad} and γ_{sl} as more layers of graphene were added. The observed differences compared to numerical simulations can be attributed to the presence of SiO_2, which alters the wetting properties of the graphene surfaces. Specifically, when comparing with model 5, we observed a significant convergence between simulations and experiments as more graphene layers were incorporated, providing evidence for the hypothesis of graphene semi-transparency. Future investigations will involve additional molecular dynamics (MD) simulations, taking into account SiO2 substrates, and incorporating the DLVO theory [90, 228] to directly consider the effect of the substrate at the numerical level. Regarding γ_{sl}, we observed a consistent asymptotic trend across all the studied models compared to the experimental results, despite differences in the calculated values. Further MD simulations will be conducted to assess the impact of the substrate, particularly the polar nature of SiO2 substrates, on the spreading dynamics of water droplets, influencing the advancing contact angle and subsequently γ_{sl}.

Finally, within the scope of a multi-scale framework encompassing atomistic to continuum simulations, we investigated the friction coefficient between graphene and water, which can be utilized to define the generalized Navier boundary condition. Intriguingly, we observed that certain models, despite exhibiting nearly identical work of adhesion and contact angles, displayed different friction coefficient values. This observation emphasizes the importance of accurately characterizing the graphene/water interface, even concerning dynamic properties.

In summary, the protocol presented in this Chapter serves as a valuable tool for selecting an appropriate molecular dynamics (MD) representation of interface problems, thereby improving the numerical depiction of both static and dynamic characteristics. Beyond the specific case study described in this chapter, this protocol can be readily extended to various material classes, facilitating a more comprehensive characterization of interfaces. By utilizing this protocol, researchers can enhance their understanding of interface phenomena across a wide range of materials.

Chapter 5

Coarse-grained water models with enhanced accuracy and speed-up factor[1]

To establish a multi-scale framework, the first step is to develop and validate a mesoscopic CG model capable of accurately describing a probe liquid like water, particularly its interface and mass transport properties. The purpose of this model is to accurately describe such properties while minimizing computational costs. The importance of this approach lies in the fact that interface phenomena involve different length scales, depending on both the chemical composition and surface topology. Therefore, after determining the chemical nature of the interface as discussed in Chapters 3 and 4, accelerated simulations are necessary to investigate the effects of surface structures or roughness.

In this Chapter we explore the tantalizing possibility of carrying out CG-MD simulations of liquid water with near-atomistic quality using the MOLC model [138], which is available as a user-defined package for the popular materials modeling code LAMMPS [175, 176]. The CG models of water presented in this Chapter use one site to represent the whole molecule, but with the possibility to host an arbitrary number of virtual charges to account for realistic electrostatic interactions (see Fig. 5.1).

[1] Part of the work included in this chapter was previously published by Bellussi *et al.* in Ref. [2]



Fig. 5.1 Pictorial view of the water CG model. Beads (violet spheres) correspond to water molecules (graphically represented inside beads). Beads are decorated with virtual sites representing point charges, which correspond to the charges of the reference all-atom, to consider the relative orientation of molecules. Fig. from Ref. [2].

This chapter is organized as follows: first, in the Computational Methods section, we describe the procedure for constructing the CG water model and outline the process of back-mapping the structure to its atomistic counterpart. Additionally, we provide details on the methods utilized to evaluate various physical properties of both the CG and AA models. Next, we present and discuss the results obtained from validating the proposed CG model. We analyze its performance and compare it to the desired accuracy for describing interface properties. Finally, we conclude by summarizing the findings and outlining potential future directions for research in the field of interface properties and surface design.

5.1 Computational methods

In this section, we describe the computational methods adopted to build the CG water model and evaluate some of its physical observables like viscosity, self-diffusion coefficient, surface tension, and enthalpy of vaporization.

5.1.1 Model building

In the MOLC model, the electrostatic interactions are accounted for *via* virtual sites acting as point charges (see Figs. 5.2a–b). The sites are placed within a skin distance from the external surface of a parent CG particle, i.e., an ellipsoid. For the specific case of water, we use spheres, which are a special class of ellipsoids. The short- and long-range interactions are evaluated with a custom algorithm based on the Coulomb pairwise summation in real space and a particle-particle particle-mesh (PPPM) Ewald solver in the reciprocal space [174]. Typically, a reduced set of charges is used to replace the complete set of all-atoms charges. However, here we use the three charges of the original water model without any further modification. The novelty introduced in the MOLC model is that the point charges are defined in the ellipsoid framework to which they are related. In other words, each ellipsoid is decorated with a set of charges whose position is defined with respect to the three principal axes of the ellipsoid. As the virtual sites are defined anywhere inside the ellipsoid, we refer to them as "off–centre" charges. At each timestep, the Cartesian coordinates of each virtual charge are reconstructed by combining the position and orientation of the parent ellipsoidal particle. In this way, there is no need to keep track of the position of the virtual charges, nor to integrate it explicitly.

The AA water models studied are based on 3-site or 4-site rigid molecules with a point charge on each site (in the case of the Tip4P, the oxygen charge is displaced by 0.1546 Å), plus a single Lennard-Jones potential on the oxygen atom. The molecules are kept rigid with the SHAKE [230] or RATTLE [231] algorithms. In the MOLC force field, the three atoms are replaced with a single sphere, whose mass is that of the water molecule and whose radius is the Lennard-Jones σ parameter. The virtual site representing the oxygen charge is placed at the center of the sphere, while the virtual sites representing the hydrogen atoms are placed on the plane $z = 0$ in the molecular frame of reference. Despite using one particle per molecule, the MOLC model of water includes all the terms of the corresponding AA model, described with a different mathematical formalism. Consequently, an arbitrary AA configuration mapped to its CG counterpart will have the same inter-molecular energy in both representations. A slight difference is expected for torques: in the AA model, each atom will generate a contribution acting on the center-of-mass of the rigid molecule; in the CG model, only the virtual particles carrying the charge of hydrogen atoms will produce a torque acting on the center of the CG sphere. However, this difference

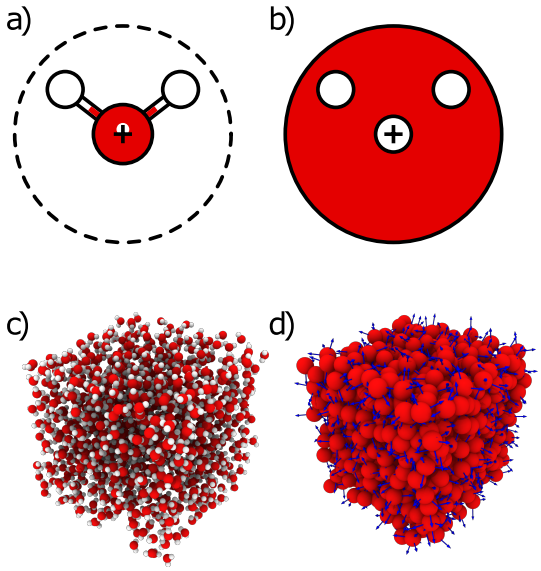

Fig. 5.2 Schematic view of the (a) AA and (b) CG water models. The dashed line in (a) represents the Lennard-Jones sphere centered at the oxygen atom, while the small white point is the center of mass of the molecule. The red circle in (b) represents a finite-size sphere centered at the cross, while the white dots represent the virtual charges. Pictorial view of an (c) AA and the equivalent (d) CG sample of bulk water. The arrows in (d) show the orientation of the three axes of inertia per each finite-size sphere representing a single water molecule. Fig. from Ref. [2].

is limited as the center-of-mass of the water molecule lies some 0.07 Å from the position of oxygen, as shown in Fig. 5.2a.

The CG trajectories can be easily reverse-mapped to the AA representation by using the position and quaternion of each ellipsoid, fully exploiting the extra rotational degrees of freedom associated with finite-size particles. The reverse-mapped trajectories were computed with the open-source Backmap code [232]. A side-by-side comparison of AA and CG samples is shown in Figs. 5.2c–d. For the special cases of the rigid water models (e.g., MD simulations integrated with the SHAKE algorithm [230]), the AA trajectories can be directly compared to the reverse-mapped trajectories using structural observables such as radial distribution functions.

The initial configuration of each simulated system was generated using the program Moltemplate [137], with 3D periodic boundary conditions (PBC) applied. A multi-stage compression was then performed at 298 K by shrinking the initial

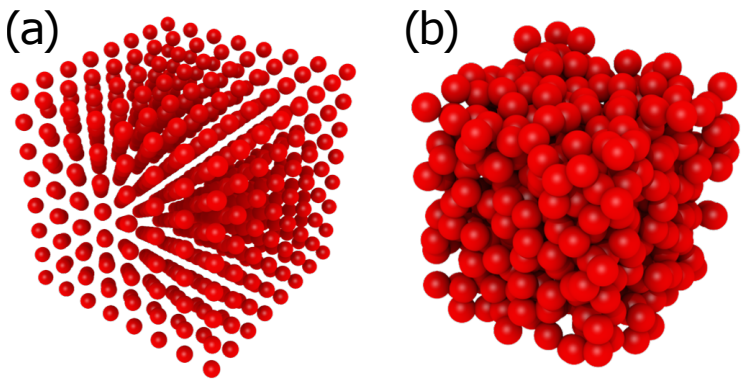

Fig. 5.3 (a) Initial guess and (b) condensed state at 298 K and 1 atm for a sample of 1000 CG water molecules. Fig. from Ref. [2].

simulation box until the system reached a target density of 1 g/cm^3. At each step, the box volume was reduced by 14% every 50 ps. Finally, the system was left free to relax in the NPT ensemble at 1 atm and 298 K for 4 ns (Fig. 5.3).

The van der Waals and electrostatic interactions were modeled with a cut-off radius of 12 Å and 10 Å, respectively. The long-range electrostatic interactions were calculated with the particle-particle particle-mesh (PPPM) method [174] ions were integrated using a timestep of 1 fs, while timesteps of 1 fs or 10 fs were used for the CG simulations.

We test the validity of the MOLC representation for three widely used all-atom water models, namely SPC-E [188], Tip3P-Ew [233] and Tip4P-05 [187], by comparing the computed self-diffusion coefficient, dynamic viscosity, surface free energy, and enthalpy of vaporization [234–239, 204, 240] between the AA and corresponding CG models at $T = 298$ K and $p = 1$ atm. For each AA and CG model, samples made of 500, 1000, and 5000 water molecules were studied to evaluate possible size dependence on the calculated physical observables [241]. For the sake of simplicity, from this point on we will refer to the Tip3P-Ew and Tip4P-05 models as Tip3P and Tip4P, respectively. An example of a LAMMPS script for a typical CG run with the MOLC model is provided in Appendix A.3.1.

5.1.2 Dynamic viscosity

The dynamic viscosity μ was calculated from the auto-correlation function (ACF) of the off-diagonal components of the stress tensor, as expressed by Equation 4.9. The ACF is calculated every 2 fs with an integration timestep of 1 fs, and the upper limit of the integral was defined at 8 ps and 16 ps in the case of the AA and CG simulations, respectively. In the CG simulations with an integration timestep of 10 fs, the ACF is calculated every 20 fs, leaving the upper limit at 16 ps. To obtain reliable statistics, simulations were performed considering the average of the partial contributions in each orthogonal direction along 20 ns of trajectories after 20 ns of stabilization. The error bars were evaluated by combining both the space and time standard deviations. The upper limit for the AA simulation was chosen to increase the accuracy of previous work available in the literature [234], even if we did not observe significant differences after reaching the plateau (see Fig. 5.6). On the other hand, a larger integral upper limit for CG simulations was chosen to avoid possible effects of the ACF tail and to obtain a good confidence interval for the final value.

5.1.3 Self-diffusion coefficient

The self-diffusion coefficient D was calculated from the mean square displacement (MSD) of water particles as a function of the observation time using the classical Einstein relation [242]:

$$D = \frac{1}{2d} \lim_{t \to \infty} \frac{\langle [\mathbf{r}(t) - \mathbf{r}(0)]^2 \rangle}{t}, \tag{5.1}$$

where d is the dimensionality of the system, t the observation time and $\langle [\mathbf{r}(t) - \mathbf{r}(0)]^2 \rangle$ the system averaged mean square displacement. The MSD was evaluated as the space average of each orthogonal direction and the time average of 5 equally spaced blocks, along a trajectory of 4 ns (see Fig. 5.7). Also in this case, the error bars were evaluated combining both the space and time standard deviations. The error bars of the dynamic viscosity and self-diffusion coefficient were calculated considering the averaged value in time and space. Firstly we evaluated the mean value with its standard deviation in time for each orthogonal direction. Then we evaluated the mean ($\overline{X}$) and standard deviation (σ) of the three orthogonal directions

($k = 3$) mean values as:

$$\overline{X} = \frac{\sum_{i=1}^{k} \overline{x_i}}{k} \tag{5.2}$$

$$\sigma^2 = \frac{\sum_{i=1}^{k} [\sigma_i^2 (n_i - 1)] + \sum_{i=1}^{k} [n_i (\overline{x_i} - \overline{X})^2]}{\sum_{i=1}^{k} n_i - 1}, \tag{5.3}$$

where $\overline{x_i}$ is the time average in each orthogonal direction and $\overline{\sigma_i}$ its corresponding standard deviation, n_i is the total number of time blocks for each orthogonal direction.

5.1.4 Surface tension

The surface free energy γ was evaluated using the Kirkwood-Buff relation on a slab geometry. This relation is based on the normal and tangential pressure difference due to the formation of the surface [193]:

$$\gamma = \frac{L_z}{2} \left[\langle P_z \rangle - \frac{\langle P_x \rangle + \langle P_y \rangle}{2} \right], \tag{5.4}$$

where P_z is the pressure in the direction orthogonal to the surface, P_x and P_y are the pressures in the transverse directions, and L_z is the length of the simulation box in the orthogonal direction to the surface. γ was evaluated along a trajectory of 5 ns, as the average of 5 equally spaced blocks, after 5 ns of stabilization. The slab geometry was generated using PBC along x and y, and non-PBC along z, applying the slab correction for the long-range interactions [189]. A reflective wall was applied to prevent atoms or particles to migrate beyond the z fixed boundary direction.

5.1.5 Enthalpy of vaporisation

The enthalpy of vaporization of pure water was evaluated for AA and CG samples of 5000 water molecules using the textbook definition [240]:

$$\Delta H_{\text{vap}}(T) = E_{\text{liquid}}^{\text{inter}}(T) + RT \tag{5.5}$$

where $E_{\text{liquid}}^{\text{inter}}(T)$ is the inter-molecular energy of liquid water at a given T.

5.2 Results and discussion

5.2.1 System structure

The computed density of SPC-E and Tip4P CG models is 0.993 $\pm$ 0.004 g/cm^3, while that of the Tip3P CG model is 0.995 $\pm$ 0.004 g/cm^3, in excellent agreement with the corresponding AA values (0.994 $\pm$ 0.003 g/cm^3 for the SPC-E and the Tip4P, 0.992 $\pm$ 0.004 g/cm^3 for the Tip3P). Furthermore, the 1-to-1 correspondence between the CG and AA representations allows to reintroduce the atomic detail into the CG trajectories without loss of structural information (and vice-versa): the resulting reverse-mapped trajectory was then used to compute the oxygen-oxygen (O-O), oxygen-hydrogen (O-H) and hydrogen-hydrogen (H-H) radial distribution functions (RDFs) for the CG samples. The overlap between the RDFs of the AA and CG models in Fig. 5.4 further corroborates the structural equivalence of the two models.

The position and intensity of RDF peaks from reverse-mapped CG trajectories closely match those from AA simulations. The first and second peaks in the O–O distance are consistently broader in the CG samples, resulting also in a smaller depth of the first well, which is more pronounced for the Tip4P CG model. We attribute this difference to the shifted reference of the axis of inertia, which is centered in the center-of-mass in the AA model (Fig. 5.2a), while in the center of the bead in the CG one (Fig. 5.2b). This leads to slightly different dynamics between the AA and CG models. Such difference is magnified in the Tip4P model since it includes an additional interaction center producing a torque on each molecule.

5.2.2 Self-diffusion coefficient, dynamic viscosity, and surface free energy

The self-diffusion coefficient (D), dynamic viscosity (μ), and surface free energy (γ) of both the AA and CG water models evaluated with a timestep of 1 fs are summarized in Tab. 5.1. The results of AA simulations are in good agreement with reference modeling and experimental values found in the literature [234, 238, 235, 123, 204], without showing a system size dependence within the computed error

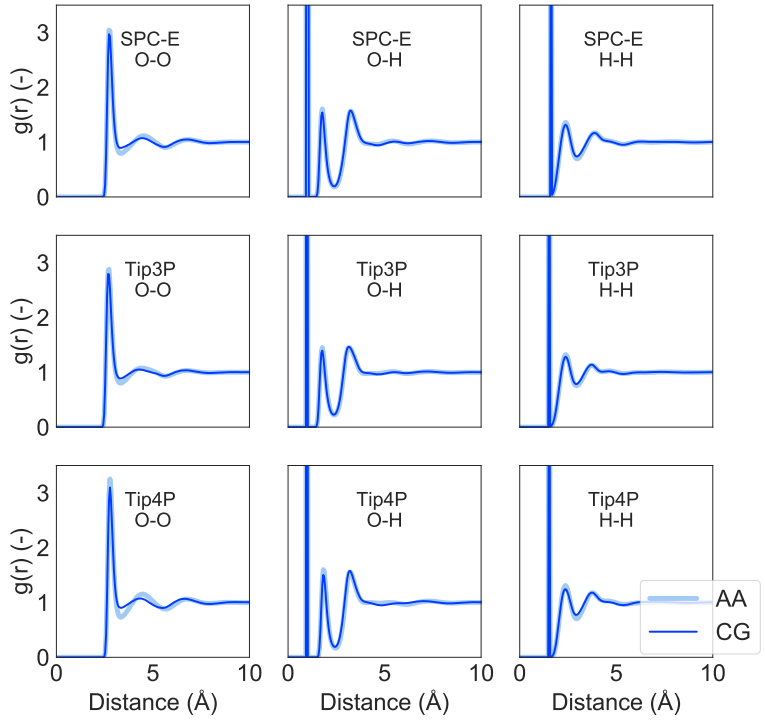

Fig. 5.4 Radial distribution functions $g(r)$ computed from all-atoms (AA) and reverse-mapped coarse-grained (CG) samples for different water models and atoms. Fig. from Ref. [2].

bars. Nevertheless, we observe a progressive reduction of the error bar of D with larger samples, because of the improved statistics.

The self-diffusion coefficient and dynamic viscosity derived from CG simulations are also plotted against the AA reference in Figs 5.5a-b. Results show that the self-diffusion coefficient computed from CG simulations is slightly lower than that from AA ones. Consistently, μ of CG samples is higher than that of AA ones. This evidence agrees with the Stokes-Einstein relation [235] ($D^* = \frac{k_B T}{6\pi\mu r}$, being k_B the Boltzmann constant and r the radius of water molecules, strictly valid for spherical particles), thus proving the self-consistency of the proposed model (see Fig. 5.5c).

The transient values of μ and D are reported in Figs. 5.6 and 5.7, highlighting the substantial convergence of simulations. Furthermore, all obtained results remain in good agreement with the experimental values [243, 234]. Finally, in Fig. 5.5d we

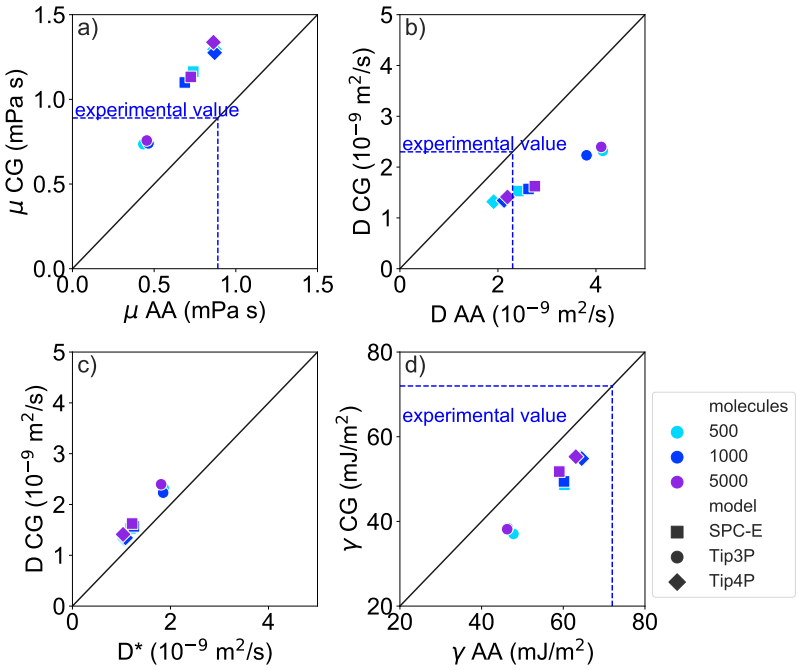

Fig. 5.5 (a) Dynamic viscosity, (b) self-diffusion coefficient, and (d) surface free energy computed with integration timestep of 1 fs for different CG and AA water models and system sizes. Error bars are reported in Tab. 5.1 for clarity. (c) Comparison between the self-diffusion coefficient calculated from the Stokes-Einstein relation ($D^* = \frac{k_B T}{6\pi\mu r}$) and from the mean square displacement (D) for the CG models. Water models are represented by different symbols, while system sizes by colors. Experimental values refer to bulk water properties at $T = 298$ K and $p = 1$ atm. Fig. from Ref. [2].

compare the γ computed with the AA and CG models. The results show an average reduction with respect to the AA reference. However, in the specific case of the SPC-E and the Tip4P CG models, the calculated γ still represents a good approximation of the experimental value (72.8 mJ/m^2) [244], making the CG water models perfectly suitable for describing multi-phase systems and interfacial phenomena. The observed differences between the AA and CG results can be partially explained by the fact that the geometry of the CG model is based on a finite-size sphere and not on an ellipsoid. In fact, the shape of the ellipsoid directly influences the potential energy of the system according to the Gay-Berne potential, as well as the calculation of pressure. Consequently, this can directly affect the evolution of the dynamics and the calculation of thermodynamic and transport properties.

Table 5.1 Self-diffusion coefficient (D, 10^{-9} m^2/s), dynamic viscosity (μ, mPa s) and surface free energy (γ, mJ/m^2) considering a timestep of 1 fs. Results from all-atoms (AA) and coarse-grained (CG) simulations are reported.

	Mol	D AA	D CG 1fs	μ AA	μ CG 1 fs	γ AA	γ CG 1fs
SPC-E	500	2.42±0.74	1.53±0.14	0.74±0.01	1.16±0.04	60.28±2.08	48.64±1.26
	1000	2.62±0.29	1.57±0.19	0.69±0.01	1.10±0.04	59.45±0.47	49.09±1.55
	5000	2.75±0.16	1.62±0.13	0.72±0.02	1.13±0.03	59.02±1.12	51.77±1.80
Tip3P	500	4.14±0.82	2.32±0.44	0.43±0.02	0.74±0.03	47.80±0.85	37.05±1.88
	1000	3.81±0.57	2.23±0.25	0.46±0.01	0.74±0.03	46.40±0.98	38.41±1.37
	5000	4.11±0.33	2.40±0.16	0.45±0.01	0.76±0.02	46.26±0.38	38.16±0.63
Tip4P	500	1.91±0.41	1.32±0.34	0.87±0.03	1.30±0.05	64.38±2.37	55.16±1.59
	1000	2.13±0.32	1.34±0.16	0.87±0.01	1.28±0.04	64.52±0.98	54.84±1.51
	5000	2.19±0.11	1.41±0.08	0.86±0.02	1.34±0.03	63.07±1.54	55.29±0.78

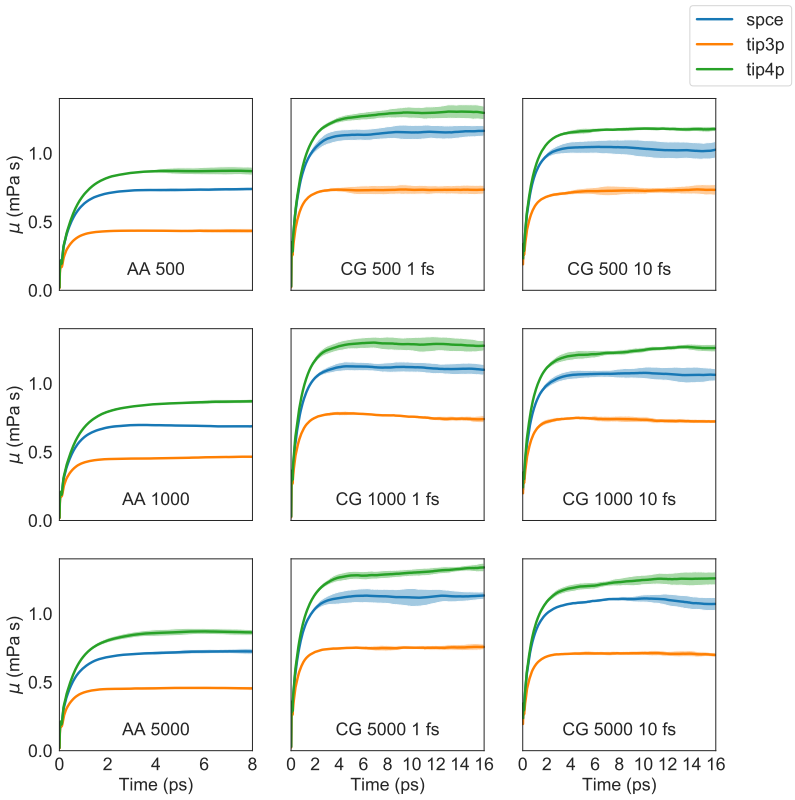

Fig. 5.6 Integrated auto-correlation functions (ACF) for the evaluation of the dynamic viscosity of the system studied. The upper limit of the integral of the ACFs for the AA systems is fixed at 8 ps, while in the case of the CG systems is at 16 ps, to evaluate possible tail effects. The error bands are obtained considering the deviation with respect to the mean on three orthogonal dimensions and the mean value in time. Fig. from Ref. [2].

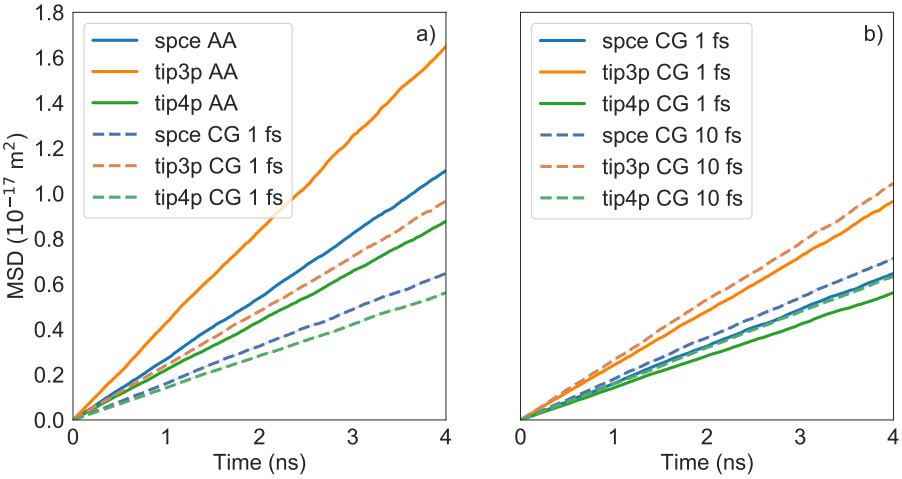

Fig. 5.7 Mean square displacements of water molecules for the systems studied. (a) Comparison between AA and CG systems integrated with a time step of 1 fs. (b) Comparison between CG systems integrated with a timestep of 1 fs and 10 fs. Fig. from Ref. [2].

5.2.3 Timestep effect

The self-diffusion coefficient, dynamic viscosity, and surface free energy computed from the CG-MD simulations integrated with a longer timestep of 10 fs are summarized in Fig. 5.8 and fully reported in Tab. 5.2 Also in this case, the evaluated physical observables are not sensibly dependent on the system size.

The viscosity and self-diffusion coefficients obtained with a longer timestep (Figs. 5.8a–b) are consistent with those obtained with a timestep equal to 1 fs. The self-diffusion coefficients D^* computed *via* the Stokes-Einstein relation from the μ values are also consistent with those obtained with the mean square displacement (Fig. 5.8c). No significant difference is observed for the computed value of the surface free energy (Fig. 5.8d). These results show that no substantial degradation of the computed properties of CG models is observed using a longer timestep of 10 fs. Furthermore, for the specific case of the SPC-E and the Tip4P CG models, we recall the good accuracy with respect to the experimental values.

Table 5.2 Self-diffusion coefficient (D, 10^{-9} m^2/s), dynamic viscosity (μ, mPa s) and surface free energy (γ, mJ/m^2) considering a timestep of 10 fs. Results from coarse-grained (CG) simulations are reported.

	Mol	D CG 10fs	μ CG 10fs	γ CG 10fs
SPC-E	500	1.70±0.28	1.03±0.06	47.05±2.05
	1000	1.64±0.25	1.06±0.05	48.15±1.54
	5000	1.79±0.11	1.07±0.05	51.05±1.63
Tip3P	500	2.56±0.41	0.73±0.04	38.47±1.98
	1000	2.57±0.39	0.72±0.01	37.25±1.18
	5000	2.58±0.16	0.70±0.02	37.39±1.07
Tip4P	500	1.53±0.23	1.18±0.02	53.92±1.92
	1000	1.42±0.21	1.26±0.03	55.12±2.71
	5000	1.60±0.13	1.26±0.05	53.87±1.78

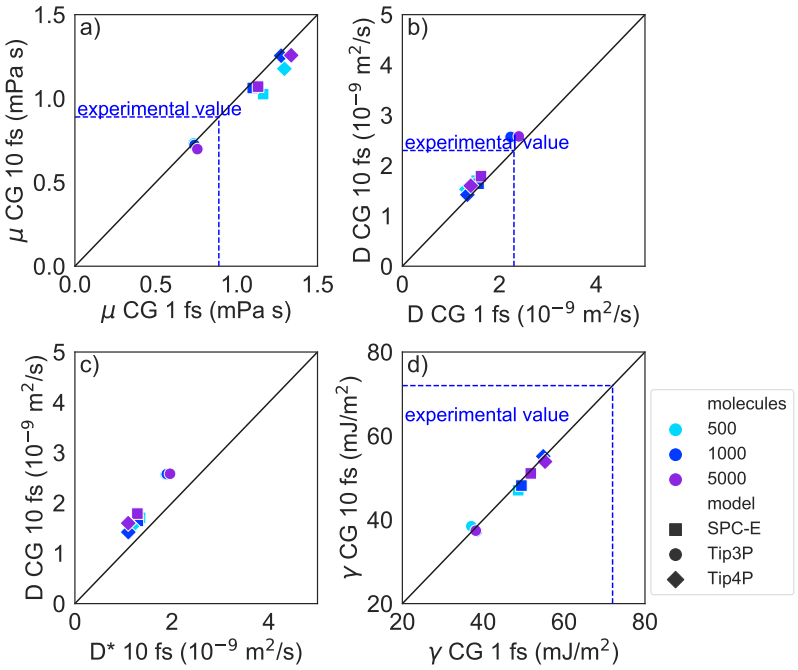

Fig. 5.8 (a) Dynamic viscosity, (b) self-diffusion coefficient, and (d) surface free energy computed with integration timesteps of 1 fs and 10 fs for different CG models and system sizes. Error bars are reported in Tab. 5.2 for clarity. (c) Comparison between the self-diffusion coefficient calculated from the Stokes-Einstein relation ($D^* = \frac{k_B T}{6\pi\mu r}$) and from the mean square displacement (D) for the CG models with 10 fs timestep. Water models are represented by different symbols, while system sizes by colors. Experimental values refer to bulk water properties at $T = 298$ K and $p = 1$ atm. Fig. from Ref. [2].

5.2.4 Enthalpy of vaporisation

The computed enthalpy of vaporization for samples of 5000 molecules is reported in Tab. 5.3, showing a substantial agreement between the AA and CG models. A comprehensive assessment of other thermodynamic properties, such as the low-temperature density anomaly or the melting temperature [141, 245, 246], will be the subject of future investigations.

Table 5.3 Enthalpy of vaporization (ΔH_{vap}, kJ/mol). Results from all-atoms (AA) and coarse-grained (CG) simulations are reported. The reference experimental value is 44 kJ/mol [246].

Model	ΔH_{vap} AA	ΔH_{vap} CG
SPC-E	49.1±0.09	49.4±0.09
Tip3P	44.1±0.09	44.5±0.09
Tip4P	50.1±0.10	50.4±0.10

5.2.5 Wall time ration and speed-up factor

Considering the Tip3P water as a representative case study for assessing the computational performance of the MOLC model, Fig. 5.9a reports the wall time ratio ($wall\ time\ ratio = CG\ elapsed\ computational\ time/AA\ elapsed\ computational\ time$) between CG and AA simulations with the same trajectory length. At a given timestep (1 fs), the computational cost of the CG models results approximately the same as the AA ones, being the wall time ratio between CG and AA in the range of 0.8-1.8. Indeed, despite reducing the number of particles from 3 to 1, the electrostatic interactions are identical in the AA and CG force fields and so is the computational cost. On the other hand, the possibility of using a timestep of 10 fs leads to a speed-up factor ($speed\text{-}up\ factor = CG\ performance/AA\ performance$, being the performance evaluated as nanoseconds of trajectory computed per day) of up to 6x (see Fig. 5.9b).

The use of a longer timestep has the obvious advantage of speeding up significantly the mesoscopic model with respect to the original atomistic one. As a matter of fact, the timestep of AA water simulations typically does not exceed 2 fs, even for accelerated MD simulations of bio-molecules where the scale of microseconds is routinely achieved [247, 248]. Here we investigate the longest timestep still able to guarantee stable CG simulations and realistic water properties. To this, we compute

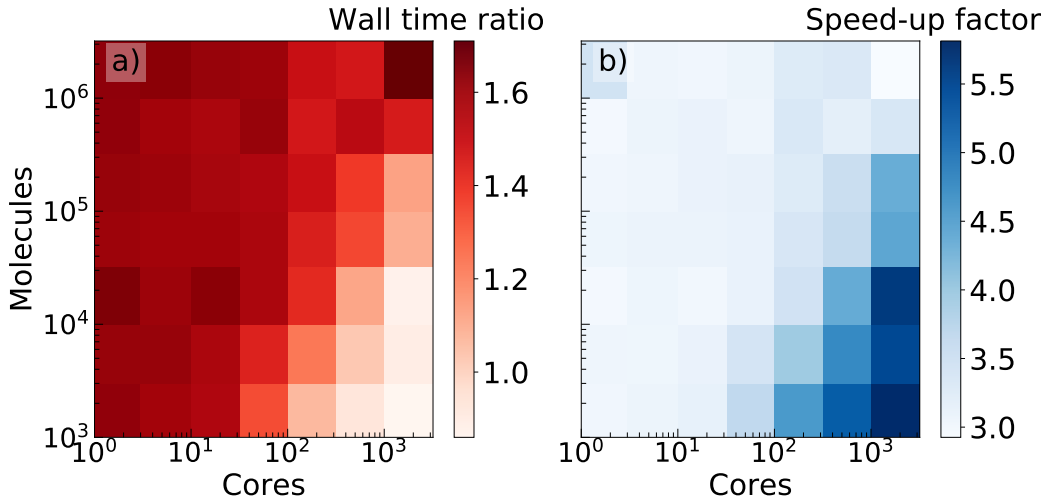

Fig. 5.9 (a) Wall time ratio between the MOLC CG model and the corresponding AA model considering different boxes of Tip3P water molecules and a variable amount of computational cores (2 x 24-cores/node Intel Xeon 8160 at 2.10 GHz), but a fixed timestep of 1 fs for both models. (b) Speed-up factor of CG model with respect to AA one, when the former is simulated with a timestep of 10 fs and the latter of 1 fs. Fig. from Ref. [2].

the viscosity of the Tip3P water model using timesteps of 1, 10, 15, 20, 40, and 80 fs. As the timestep is increased, numerical instabilities arise from the accumulation of integration errors. To mitigate the inaccuracies in sampling the higher frequency motions, the mass of CG water molecules is progressively increased to have a larger moment of inertia and slower dynamics (see Fig. 5.10), an expedient already adopted in other works [249]. The higher mass of CG water molecules leads to simulation stability up to 80 fs timestep, but results show a steady increase of dynamic viscosity with mass (see Fig. 5.11) in agreement with literature values [250]. The scaled density and RDFs, instead, are in excellent agreement with the reference values even with the largest timestep tested.

A core feature of the MOLC model is to represent the inter-molecular interactions via a Gay-Berne potential and point charges, which can be seamlessly mixed with standard AA force fields based on Lennard-Jones potentials. Using this framework, water models based on four or more point charges can be readily transformed into a CG model without any reparametrization, and AA force fields can be mixed with CG models in the same simulation. Another direction for the fine-tuning of CG water models involves replacing the finite-size isotropic spheres with finite-size anisotropic ellipsoids, to reproduce the anisotropic inertia tensor of the AA water model. Ultra-

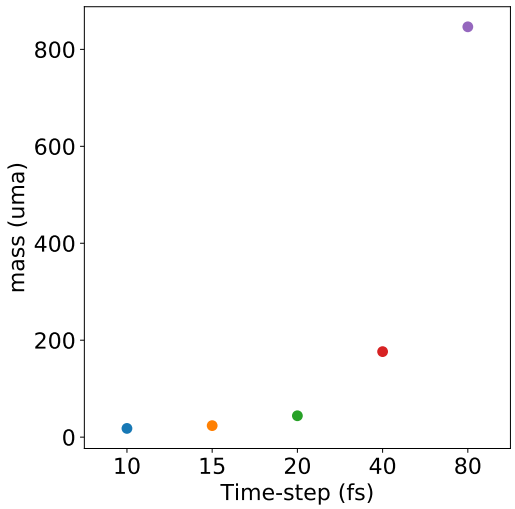

Fig. 5.10 Variation of mass for the CG Tip3P water model to limit the numerical instabilities while increasing the integration timestep. Fig. from Ref. [2].

coarse-grained models [251–253], i.e., where a single particle represents a cluster of water molecules, are also natively supported by the MOLC model and easily implementable by placing many electrostatic sites inside a large spheroidal particle, whose position and strength should be optimized to reproduce simultaneously the packing of pure water and its enthalpy of vaporization. The implementation of new water models is beyond the scope of this thesis, but it is mentioned to encourage the translation of existing force fields in the MOLC representation. Similarly, from an application point of view, further studies will be necessary to validate the proposed model in multi-phase systems (e.g., for the description of wettability or adsorption phenomena) [49, 254, 255], nanoconfined geometries [256, 64] or heat transfer processes [257, 258].

5.3 Further perspectives

In this work, we have proposed, tested, and validated a new coarse description of classic water models based on the MOLC force field. We chose three popular all-atoms models (SPC-E, Tip3P-Ew, and Tip4P-05) and found that their corresponding coarse-grained representations show accurate structural and dynamical properties: density, radial distribution functions, self-diffusion coefficient, dynamic viscosity, surface free, and enthalpy of vaporization. We observed a reduction of the CG

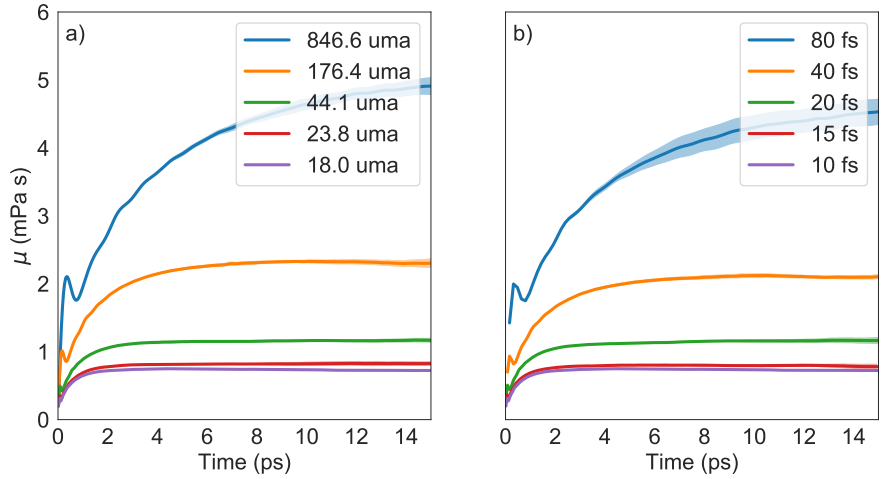

Fig. 5.11 (a) Variation of dynamic viscosity for different water masses with an integration timestep of 10 fs and Tip3P CG model. (b) Variation of dynamic viscosity for different water masses and different timesteps, considering a Tip3P CG model. Comparing the two panels, we can observe that the dynamic viscosity depends mainly on the water mass and not on the integration timestep. Fig. from Ref. [2].

self-diffusion coefficient, which is matched by an increase in the dynamic viscosity, consistently with the Stokes-Einstein relation. The computed surface free energy is approximately 14% smaller for all the CG models. However, the computed surface free energy is still reasonably close to the experimental value, confirming that the CG models of water are good enough for describing interface problems such as materials wettability or adsorption phenomena.

A speed-up factor between 3 and 6 times is obtained with respect to the AA model, being entirely due to the increase in the integration timestep unlocked by coarse-graining. The speed-up achieved through the development of this model, combined with the accuracy obtained in terms of bulk and interface properties, establishes the MOLC CG representation of atomistic water as a robust model for the development of a multi-scale approach to predict surface wettability and aid in their design.

Nevertheless, the primary limitation of the proposed model is its current exclusive implementation within LAMMPS. For biomolecular simulations, such as protein folding and unfolding, which often involve longer time scales, alternative software tools like GROMACS [259], NAMD [260], or Amber [261] are predominantly favored due to their generally superior computational performance compared to

LAMMPS. In addition, wider adoption of the model by other groups may be limited by the complexity of using MOLC in LAMMPS, as comprehensive documentation is not yet available.

In the following Chapter 6, we will delve into the development and validation of a CG model for polymers. Once validated with respect to some bulk properties, we will demonstrate its coupling with the water model discussed here, as well as present results on polymer wettability at the CG level.

Chapter 6

Coarse-grained polymers models: the case study of PLGA

This chapter focuses on the development and validation of a new coarse-grained (CG) polymer model, designed to accurately describe interface properties while minimizing computational costs. The significance of this approach lies in the consideration of the interface phenomena's multi-scale nature, which depends on both chemical composition and surface topology. Therefore, after assessing the chemical nature of the interface, as done in previous Chapters 3 and 4, accelerated simulations are necessary to examine the potential effects of surface structures or roughness. Consequently, the next step towards establishing a multi-scale framework for evaluating interface and wettability properties involves developing and validating a mesoscopic CG model capable of accurately describing condensed phases like polymers. Based on the findings presented in Chapter 3, the focus here is on PLGA (Poly(lactic-co-glycolic acid)).

The validation of this model includes assessing several bulk properties, such as glass transition temperature, thermal conductivity, and elastic moduli. Once validated, this model will be coupled with the water model proposed in Chapter 5 to demonstrate how the combined model can assess wetting properties by accurately replicating the sessile droplet experiment, even on surfaces with nano-roughness (see Fig. 6.1). Validating the bulk properties is not only necessary to ensure the model's quality but also because a single phase's bulk properties can impact the interface

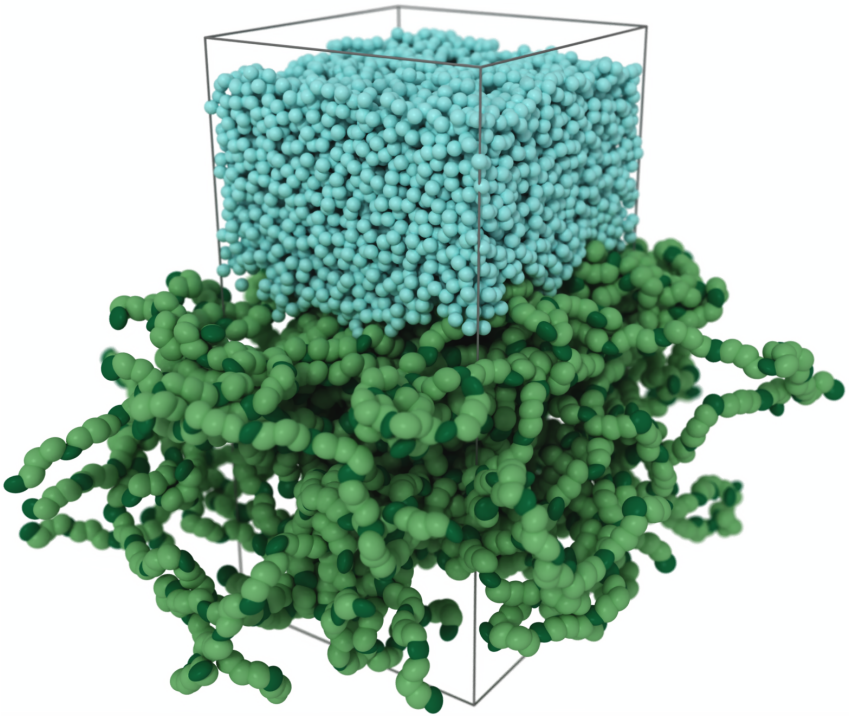

Fig. 6.1 Pictorial view of the coupled PLGA/water CG model

properties of the coupled model. For instance, the substrate's stiffness can influence the deformation of the soft interface, thereby affecting the overall results.

This chapter is structured as follows: first, in the Computational Details section, we outline the process of constructing the coarse-grained (CG) polymer model and its subsequent back-mapping to the atomistic counterpart. Subsequently, we elaborate on the methods employed to assess the thermal conductivity and elastic properties of both the CG and back-mapped atomistic models, and their respective results are discussed in the Results and Discussion section. Then, we describe the coupled water/polymer model and emphasize its utilization in evaluating the impacts of nano-roughness. Finally, we present concluding remarks and discuss future research prospects in this field.

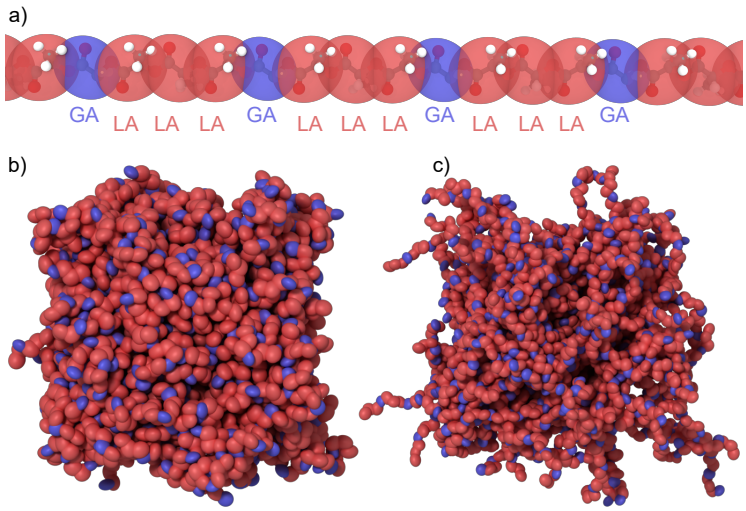

Fig. 6.2 (a) PLGA CG chain mapping. LA and GA indicate the lactic acid and glycolic acid monomer residues, respectively. Each monomer residue is represented by one coarse-grained bead. (b) Amorphous and (c) semi-crystalline PLGA CG models.

6.1 Computational methods

6.1.1 Model building

The MOLC force field [138] was used to define the PLGA coarse-grained (CG) molecules. The MOLC model uses finite-sized particles such as spheroids or ellipsoids, which have a moment of inertia, rotational energy, and angular momentum. The non-covalent interactions are represented by the Gay-Berne potential, while the electrostatic interaction depends on the internal charge distribution. The CG parameters were obtained using a bottom-up procedure that fits the atomistic parameters of the OPLS-AA force field [164]. The parameters for describing the interactions between beads, both in terms of the bond and non-bond interactions, are reported in Appendix A.4.1.

Here, we have reproduced a PLGA polymer chain that is chemically equivalent to the atomistic one. The PLGA chain has a 75:25 lactic (LA) to glycolic acid (GA) ratio and consists of 12 repetition units. The coarse-graining mapping based on the atomistic geometry is shown in Fig. 6.2a. In this model, each CG bead represents a LA or GA monomer residue, and a repetition unit corresponds to a sequence of 3 LA

and 1 GA beads, substantially reducing the number of particles in the simulation box. However, the CG beads are characterized by 6 degrees of freedom (3 translations and 3 rotations) instead of the 3 degrees of freedom of an all-atom particle. Therefore, the main advantage of the CG model in terms of computational cost is not due to a reduction in the degrees of freedom but to the possibility of using a simulation time-step that is ten or twenty times higher than that of a classical molecular dynamics simulation, how also observed in the case of water molecules (see Fig. 5.9 in Chapter 5). On the other hand, we did not observe significant differences in computational performance when using the same integration time-step for both the atomistic and CG configurations.

Taking into consideration the relative orientation of the beads, it is possible to maintain track of the atomistic distribution of the polymer chain. By keeping track of the relative orientation of the particles forming a molecule, a reverse-mapping procedure can be performed to reintroduce the atomic level of detail using a one-to-one mapping procedure. The reverse-mapping procedure is based on the knowledge of the atomic structure represented by a single finite-size particle, with its geometrical center at the point (0,0,0) and in the standard orientation (the local reference of the bead is aligned to the absolute Cartesian reference), where its axes of inertia align with the spheroids' three axes of rotational symmetry. The resulting atomic structure has a thermal energy distribution that is not equally distributed among its internal degrees of freedom. In particular, all the bonds, angles, and dihedrals derived from a single finite-size particle are at their equilibrium values, corresponding to a temperature of 0 K. To obtain a physically accurate structure, a short annealing at the desired temperature is carried out to redistribute the thermal energy evenly across the molecules. The potential energy is used to identify when the system reaches thermal equilibrium (as discussed in Section 3.1.1).

The initial configuration of the CG system was generated using Moltemplate [137]. A randomly sparse distribution of PLGA chains was placed on a cubic grid with periodic boundary conditions. We followed the multi-step compression and relaxation of the system described in Sections 3.1.1 and 5.1. Two polymer configurations were studied by differently controlling the compression and relaxation stages of the system, namely amorphous and semi-crystalline structures (see Figs. 6.2b–c). The amorphous model consists of a simulation box containing PLGA molecules without any geometrical order or periodicity between chains. This structure was obtained by allowing the polymer chains to freely deform during compression, guided by their

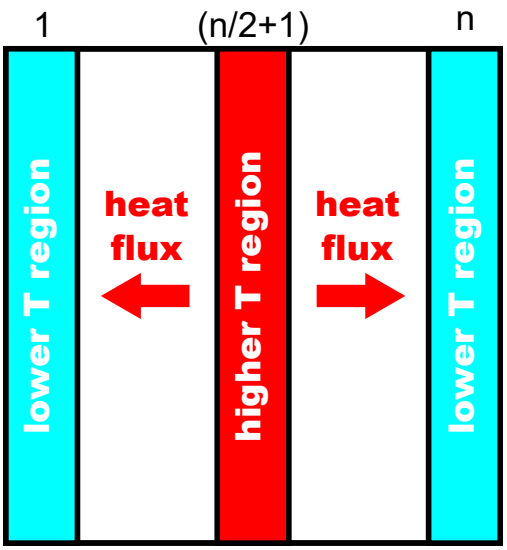

Fig. 6.3 Setup employed to compute λ by NEMD methods.

parameterized intra-molecular potential, aiming to achieve a random assembly of the chains. On the other hand, the semi-crystalline structure consists in a PLGA simulation box that presents a structural order or periodicity between chains. In this case, the system is obtained by carefully adjusting the intra-molecular potentials (bonds and angles) to maintain straight chains during the initial stages of compression, resulting in a more regular structure after the relaxation. Both the configurations were easily back-mapped to their atomistic counterparts using the open-source Backmap code [232]. To describe the atomistic configurations, we used the OPLS-AA force field [164], which is consistent with the model developed and described in Chapter 3. After the back-mapping process, we allowed the two systems to relax freely in the NPT ensemble at 298 K and 1 atm until equilibrium in energy, which typically required around 2 ns. The van der Waals and electrostatic interactions were modeled with a cutoff radius of 12 Å and 10 Å, respectively. The long-range electrostatic interactions were calculated using the particle-particle particle-mesh (PPPM) method [174]. The all-atom MD simulations were integrated using a timestep of 1 fs, while a timestep of 10 fs was used for the CG simulations. All simulations were performed using LAMMPS [175, 176].

6.1.2 Evaluation of the PLGA thermal conductivity

The thermal conductivity of the PLGA CG and back-mapped AA systems was evaluated through the non-equilibrium molecular dynamics (NEMD) approach [262]. This method is implemented by imposing a thermal gradient on the system and calculating the subsequent heat flux. The thermal gradient is imposed through a binning procedure (see Fig. 6.3). The simulation box is divided into N bins, where the terminal bins '1' and 'N' are specified as the regions at a lower temperature (cyan regions in Fig. 6.3) and the middle bin 'n/2+1' is the one at higher temperature (red region in Fig. 6.3). First, the box is divided into 21 bins, and then the central and the two extreme bins are thermostated with a Langevin thermostat at 320 K and 280 K, respectively. The equations of motion are integrated into the NVE ensemble to allow the heat flux to flow from the central to the extreme bins. The thermal conductivity is then computed through the Fourier model:

$$\mathbf{q} = \lambda_c \nabla T, \tag{6.1}$$

where $\mathbf{q}$ is the specific heat flux, λ_c is the thermal conductivity, and ∇T is the temperature gradient. ∇T is evaluated and averaged over the bins without the applied thermostat to avoid possible artifacts. First, we performed 1 ns simulations to reach the non-equilibrium steady state. Then we acquired data related to the thermal gradient and heat flux along a trajectory of 2 ns.

In the case of CG simulations, we implemented a new LAMMPS command to compute the average temperature in each bin associated with all the degrees of freedom (rotational + translational). Despite the recent increasing interest in rigid body dynamics, which is testified by the large number of new packages developed in LAMMPS [136], a command that can evaluate the average temperature per bin associated with the roto-translational kinetic energy is still lacking. Consequently, we propose to compute the roto-translational kinetic energies per bead and average their values over bins (also called chunks in LAMMPS). We defined a compute command called `compute erotate/asphere/atom` to compute the rotational kinetic energy per bead. Then, we sum its value to the translational kinetic energy contribution evaluated with the standard LAMMPS command `compute ke/atom`. The chunk

temperature is then computed through the following equation:

$$KE = \sum_{i=1}^{n} \frac{1}{2} m_i v_i^2 + \frac{1}{2} I_i \omega_i^2 = \frac{DOF}{2} k_B T \tag{6.2}$$

where KE is the total kinetic energy per chunk, i is the i-th atom in the chunk, m and v are its mass and translational velocity, respectively, I and ω are its moment of inertia and rotational velocity, respectively, DOF is the number of degrees of freedom (6 in 3D), k_B is the Boltzmann constant, and T is the chunk temperature. The thermal conductivity is evaluated along the three orthogonal directions to test for possible effects of the system structure and to increase the statistics. An example of a LAMMPS script for computing thermal conductivity is provided in Appendix A.4.1.

6.1.3 Evaluation of the PLGA elastic properties

The elastic properties of the CG and the corresponding back-mapped systems are evaluated through NEMD. In this case, after the relaxation process, we applied a box deformation along one orthogonal direction (i) while leaving the other two (j, k) free to relax (see Fig. 6.4). This process is implemented by applying a thermostat at the equilibrium temperature (298 K) and a barostat at 0 atm in the two directions orthogonal to the deformation. This allows us to compute not only the stress-strain curve and thus Young's modulus (E), but also the transverse strain associated with the shrinkage on the two directions orthogonal to the applied deformation ($\varepsilon_{j,k} - \varepsilon_i$), and thus the Poisson ratio (ν). The elastic modulus is evaluated considering the slope of the linear regression of the initial portion of the stress-strain curve (between 0 and 0.025 strain, see Fig. 6.5a). Similarly, the Poisson ratio is evaluated considering the slope of the linear regression of the initial portion of the strain-strain curve (between 0 and 0.025 strain, see Fig. 6.5b). Finally, under the assumption of isotropic material, the transverse elastic modulus (G) is evaluated as:

$$G = \frac{E}{2(1+\nu)}. \tag{6.3}$$

An example of a LAMMPS script for computing elastic properties is provided in Appendix A.4.2.

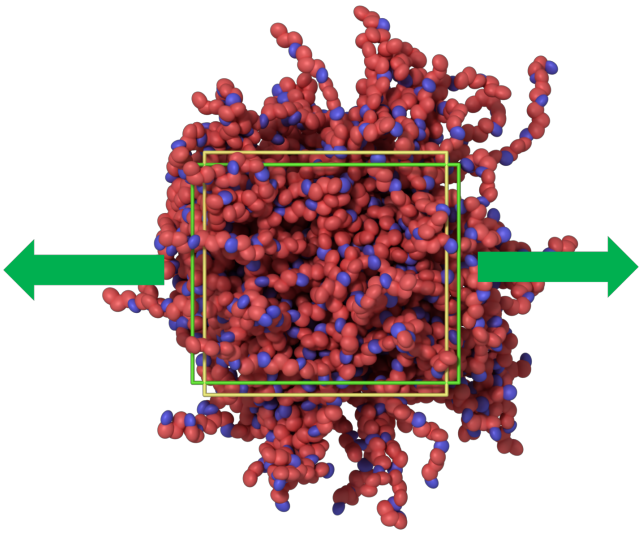

Fig. 6.4 Stress-strain test performed on the CG model by deforming the simulation box. Green arrows indicate the applied deformation by deforming the simulation domain. Yellow and green boxes indicate schematically the initial unperturbed and deformed configurations, respectively. The deformed configuration highlights both the elongation along the applied deformation direction and the shrinkage in the transversal direction.

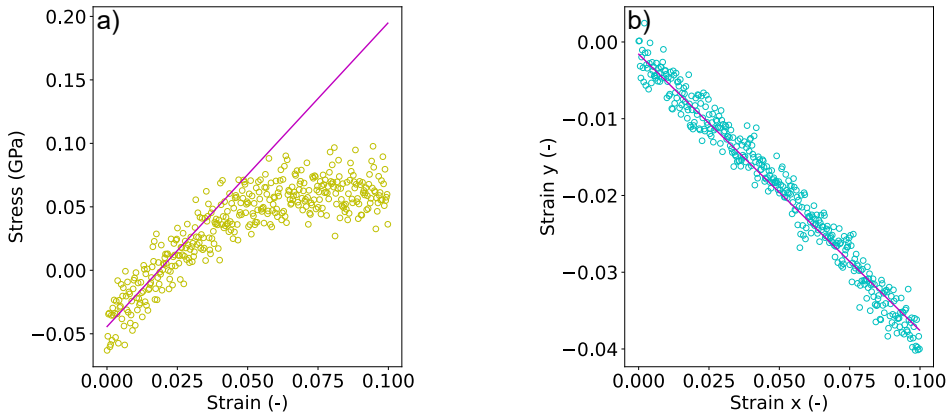

Fig. 6.5 Example of a stress-strain test performed on the CG model by deforming the simulation box. (a) Example of a stress_i-strain_i curve obtained from a test performed along the i direction. The elastic modulus is evaluated considering the slope of the linear regression of the initial portion of the stress-strain curve (between 0 and 0.025 strain, violet line). (b) Example of the $\text{strain}_{j,k}$-strain_i curve. The Poisson ratio is evaluated considering the slope of the linear regression of the initial portion of the strain-strain curve (between 0 and 0.025 strain, violet line).

6.2 Results and discussion

In this section, we present the results obtained from the CG simulations of the PLGA model, which are compared with the atomistic counterpart obtained through the back-mapping process described in Chapter 5. We evaluate the validity of the MOLC representation of polymers for two different structures of PLGA, namely amorphous and semi-crystalline, by comparing bulk properties such as elastic properties (Young's Modulus E, Poisson Ratio ν, and Tangential Modulus G) and thermal conductivity λ between the AA and corresponding CG models. All models were previously equilibrated at 298 K and 1 atm.

6.2.1 Density and glass transition temperature

The computed density of amorphous and semi-crystalline CG models is 1.256 $\pm$ 0.002 g/cm^3 and 1.248 $\pm$ 0.002 g/cm^3, respectively, in excellent agreement with their corresponding back-mapped AA models (1.280 $\pm$ 0.002 g/cm^3 and 1.288 $\pm$ 0.002 g/cm^3, respectively). These values also result in excellent agreement with experimental evidence (1.30 g/cm^3 [195, 198]).

Then, we computed the glass transition temperature (T_g) for the two CG models by performing a temperature scan between 250 K and 450 K ($\Delta T = 10K$) and monitoring the density variation [199]. Taking advantage of the higher computational time-step allowed in CG simulations, we replicated five heating-up and cooling-down cycles. This approach aims to improve statistical accuracy, reduce computational noise, and investigate potential hysteresis effects. In Figs. 6.6a–b, we report the density of PLGA as a function of temperature for the two CG models, identifying the two distinct branches of the plastic and glassy states. These branches are interpolated with two linear regressions. For the amorphous system, the T_g results in 402.5 K, while in the case of the semi-crystalline one, the T_g results in 367.0 K. These results show how the CG model developed can capture differences in some physical observable, like the T_g, due to different structural configurations, e.g., amorphous and semi-crystalline.

Due to the extremely high computational requirements needed to evaluate the T_g, we did not repeat the evaluation for the corresponding AA systems. Instead, we compared the CG T_g results with the one obtained for the amorphous PLGA system

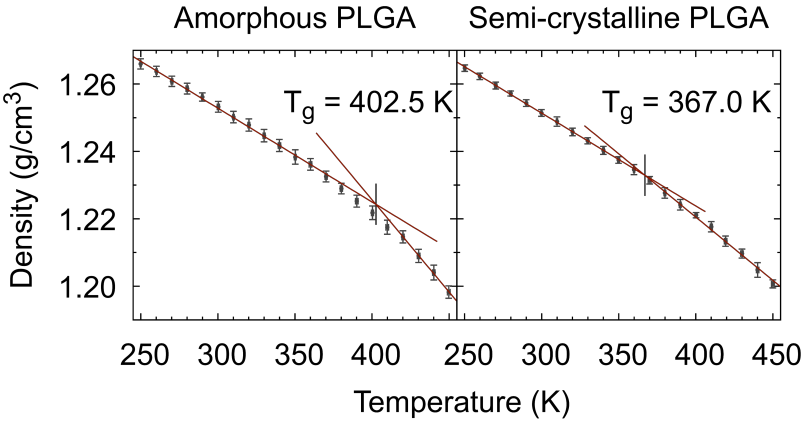

Fig. 6.6 Glass transition temperature of (a) amorphous and (b) semi-crystalline CG models obtained from the interpolation of the plastic and glassy branches.

proposed in Chapter 3, where we obtained T_g=328 K. The observed differences can be attributed partially to the comparison between different structural configurations, as the AA reference is not a CG back-mapped representation. Additionally, variations may arise due to the adopted protocols: while the CG systems underwent five heating-up and cooling-down cycles, the AA reference was subjected to a single heating-up cycle only. However, despite these factors, the CG results demonstrate reasonable agreement with available experimental data for PLGA. In Chapter 3, we reported an experimental temperature range of 320–330 K [195, 198], obtained from the producer's website of the sample used for model validation. Furthermore, the obtained results ensure that the evaluation of other properties was conducted under consistent conditions between the AA and CG models, specifically in the glassy state.

6.2.2 Thermal conductivity

In Figs. 6.7a–b, we compare the temperature profiles of a CG system with side lengths of 71 Å with that of a supercell system with side lengths of 142 Å. In the smaller system (Fig. 6.7a), despite the imposed temperatures of 320 K and 280 K in the central and extreme bins, the minimum average temperature of the cold regions is 290 K, while in the hot region, the average temperature is 310 K. We attribute this discrepancy between the imposed and measured average temperatures to the reduced number of particles in bins with respect to AA models (see Fig. 6.8). Indeed, the

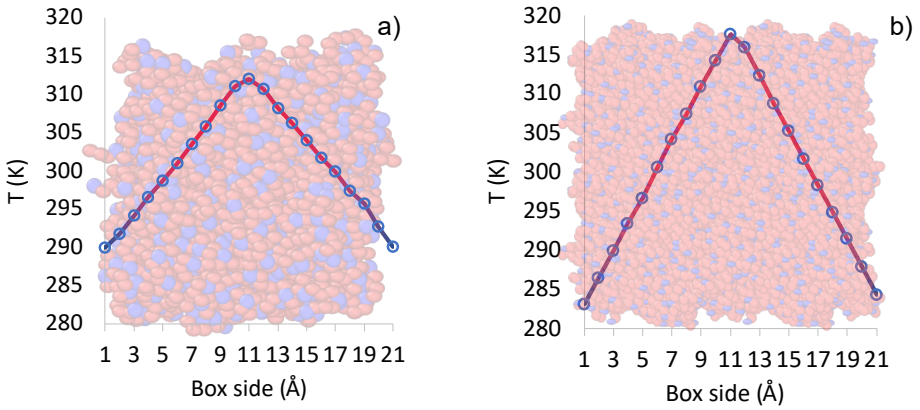

Fig. 6.7 (a) Temperature profile of the CG model evaluated on a cell with a side length of 71 Å; (b) Temperature profile of the CG model evaluated on a super-cell with side length 142 Å.

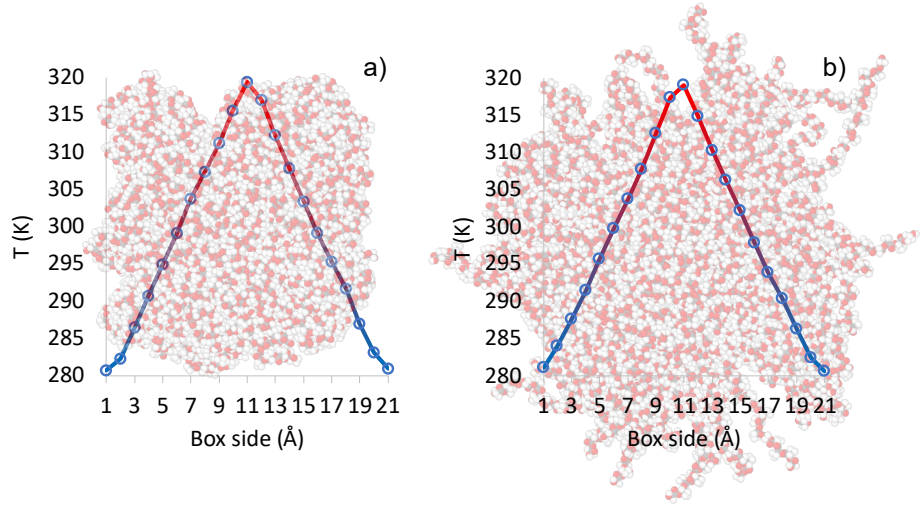

Fig. 6.8 (a) Temperature profile of the amorphous AA model evaluated on a cell with a side length of 71 Å; (b) Temperature profile of the semi-crystalline AA model evaluated on a super-cell with side length 71 Å.

number of atoms contributing to the average temperature value is reduced from the AA to the CG representation at a ratio of 1:8, resulting in less reliable statistics in each bin.

For this reason, we developed a supercell system with thicker chunks and a higher number of particles. In this case, the temperature of the thermostated hot and cold regions is in very good agreement with the imposed temperatures (318 K and 283 K, respectively). The thermal conductivity results obtained from the AA simulations

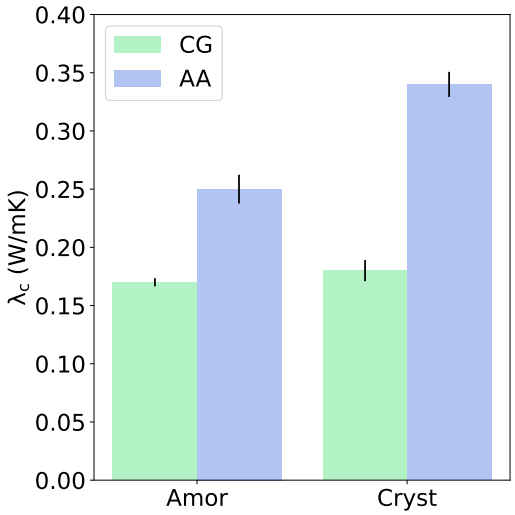

Fig. 6.9 Thermal conductivity comparison between AA and CG models for both the amorphous and semi-crystalline configurations.

agree well with both experimental findings and previous numerical simulations of polymers, falling in the range of 0.25–0.35 W/mK. For the CG models, the thermal conductivity values are in the range of 0.18–0.20 W/mK (see Fig. 6.9). To the best of our knowledge, experimental data for the thermal conductivity of PLGA are not available in the literature. Nevertheless, our results are comparable to those reported for poly-lactic acid (PLA), which are in the range of 0.18–0.20 W/mK, according to previous studies [263, 264].

Comparing the thermal conductivity between CG models shows slightly lower values than their AA counterparts. This characteristic is more evident for the semi-crystalline structures. Indeed, differently from what was observed for the T_g, in the case of λ_c, the CG system does not predict sensible differences between the amorphous and semi-crystalline structures. The reduction in thermal conductivity may be attributed to the loss of degrees of freedom and vibrational modes from the AA to the CG configurations, thus primarily affecting thermal properties and reducing the sensitivity in their evaluation, depending on different structures such as amorphous and semi-crystalline.

Further improvements, such as simulating even larger cells, could be implemented to increase the accuracy of the simulations and explore larger configurations. Additionally, other methods to evaluate λ can be used to minimize the possible effects of the binning process, such as equilibrium methods based on the Green-Kubo

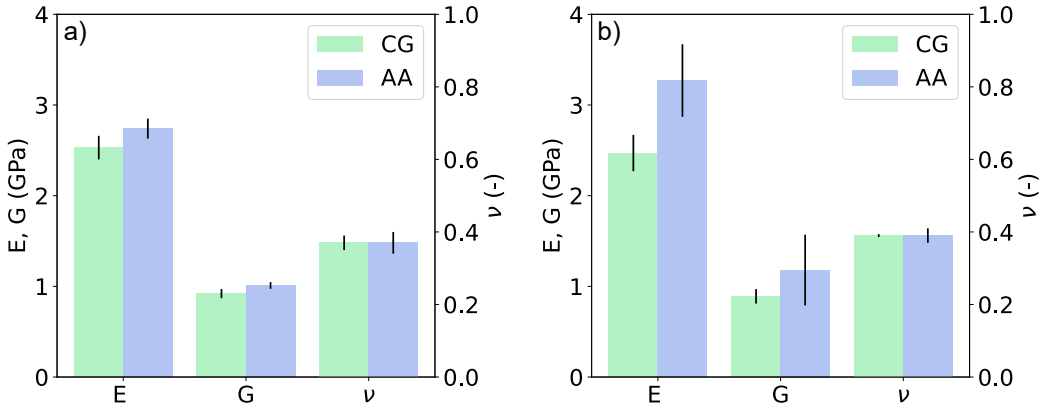

Fig. 6.10 Elastic and shear moduli and Poisson ratio comparison between AA and CG models for both the (a) amorphous and (b) semi-crystalline configurations.

relation or reverse non-equilibrium methods like the Muller-Plathe algorithm [265]. However, implementing these methods in LAMMPS for finite-sized particles would require further LAMMPS modifications, which goes beyond the scope of this work.

6.2.3 Elastic properties

Figs 6.10a and b show a comparison of the elastic properties of amorphous and semi-crystalline CG models with their AA counterparts. Both the AA and CG models agree well with experimental data available in the literature on elastic properties [266]. In the case of amorphous systems, the difference between the AA and CG models is within the error bars for both Young's modulus and Poisson's ratio, and hence for the tangential elastic modulus. The equivalence of Young's modulus and Poisson's ratio indicates the same stress and lateral shrinkage response between AA and CG models for lateral and longitudinal deformation. For semi-crystalline models, we observe a slight difference in Young's modulus. As seen in the case of thermal conductivity, the CG model is less sensitive to the structural characteristics of the numerical sample. In contrast, for Poisson's ratio, both AA and CG semi-crystalline systems exhibit the same lateral shrinkage response to longitudinal deformation. Consequently, the derivative CG transverse modulus is lower than that of the AA system, but still within the error bar.

6.3 Coupled water/PLGA CG model

This section describes the coupling process between the water and PLGA coarse-grained (CG) models that were previously developed. This activity builds upon the works described in Chapters 3. The intermolecular Van der Waals interactions between the two phases are described using the Lorentz-Berthelot mixing rule (see Eqs. 4.4 and 4.5. We reproduced the sessile droplet experiment by extending the protocol described in Chapter 3 to the CG configuration. The CG systems studied consisted of amorphous and semi-crystalline supercells with dimensions equivalent to the system described at the atomistic level (approximately 350,000 atoms, which implies around 50,000 CG beads).

The evolution of a water droplet on the PLGA amorphous and semi-crystalline surfaces is shown in Figs. 6.11 and 6.12 over a trajectory of 20 ns. Based on these preliminary results, considering the last 5 ns of simulations as the acquisition time, we observed a water contact angle (CA) of $37^\circ \pm 5^\circ$ and $33^\circ \pm 4^\circ$ for the amorphous and semi-crystalline systems, respectively. The difference with the value calculated in Chapter 3 ($61.7^\circ \pm 3.8^\circ$) can be attributed, first, to the structural difference between the atomistic and CG samples, which may be affected by different surface roughness. Furthermore, the reduction in CA is consistent with the reduction of water surface tension of the CG model compared to the atomistic counterpart. Finally, it is worth mentioning that performing simulations on larger systems would be beneficial to reduce the numerical noise of the CG droplets and aligns with the motivation behind developing this method.

6.4 Further perspectives

In this Chapter, we proposed, tested, and validated a new coarse-grained (CG) PLGA model based on the MOLC force field, using the OPLS-AA atomistic (AA) force field as a parametrization reference.

We investigated two different material configurations, namely amorphous and semi-crystalline structures, using the proposed coarse-grained (CG) representation. In both cases, the CG model accurately reproduced the structural and thermal properties compared to their atomistic (AA) counterparts obtained through a back-mapping process. The density (ρ) of the CG models agreed excellently with the corresponding

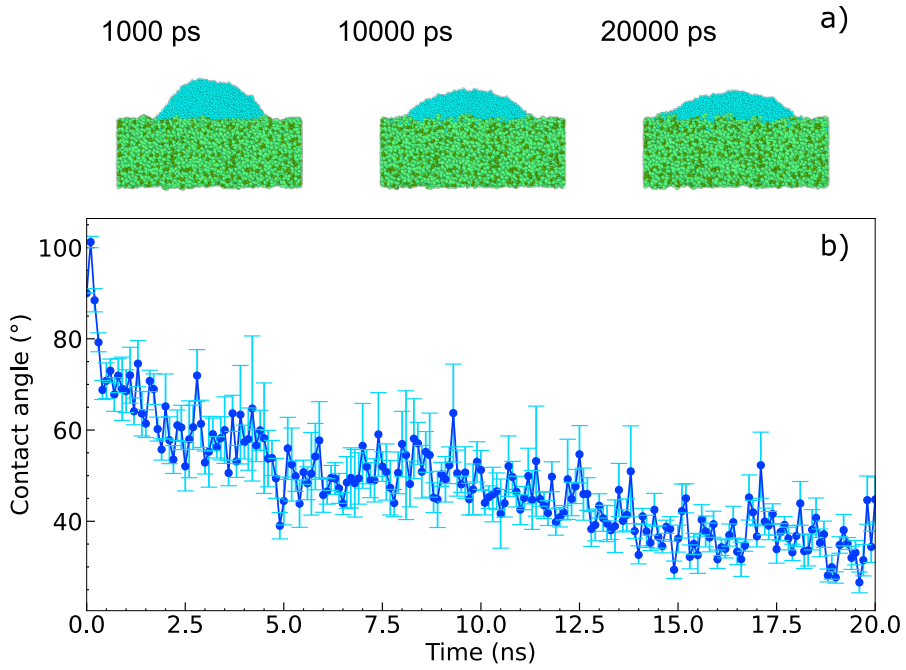

Fig. 6.11 (a) Pictorial view of the CG water droplet evolution during the simulated stabilization on the CG PLGA amorphous surface. (b) Variation of the apparent contact angle during the stabilization and acquisition trajectory.

back-mapped AA representations and experimental values. Assessing the glass transition temperature (T_g) at the atomistic level would have required prohibitively high computational resources, so we compared the CG results with those reported in Chapter 3. The observed difference was still reasonable, considering the reduced degrees of freedom and structural differences between the compared models. Additionally, the CG results remained reasonably consistent with experimental evidence. Both the CG and AA models exhibited good agreement with experimental evidence in terms of thermal conductivity (λ), with a close match between the two representations. The main discrepancy was observed in the semi-crystalline CG structure, which failed to fully capture the increase in λ resulting from chain distributions. Similar behavior was observed in the case of elastic properties. Despite the excellent agreement between the CG and AA configurations in terms of Young's Modulus (E), Poisson's Ratio (ν), and Tangential Modulus (G), the values consistently fell within the error bars, except E for the semi-crystalline configuration.

In any case, all the results show good agreement with the experimental evidence. The substantial equivalence in structure and properties between the CG and AA

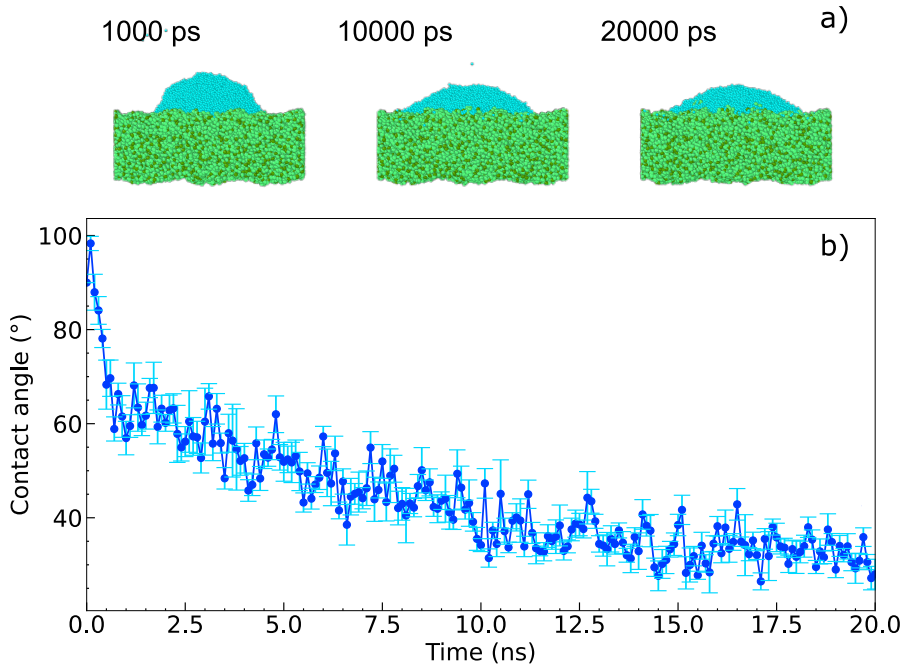

Fig. 6.12 (a) Pictorial view of the CG water droplet evolution during the simulated stabilization on the CG PLGA semi-crystalline surface. (b) Variation of the apparent contact angle during the stabilization and acquisition trajectory.

models (with only a short annealing period of around 1 ns required to relax the back-mapped structure), combined with the 10x timestep enhancement in computational performance, enables the study of more extensive and complex polymer structures, especially in the development of supercells for surface property evaluations.

With this in mind, we conducted sessile droplet experiments on amorphous and semi-crystalline supercells, observing their behavior over trajectories of 20 ns. The results, although preliminary, indicate a lower contact angle (CA) compared to the atomistic results reported in Chapter 3. This reduction in CA can be attributed to the lower surface tension of the coarse-grained (CG) water model in comparison to the atomistic counterpart. Furthermore, potential effects arising from variations in surface roughness should be considered due to the differences in morphology. Future refinements will include optimizing the post-processing techniques for CA evaluation, as well as conducting simulations on larger systems to minimize potential numerical noise.

Once optimized, the objective of this activity will be to construct a polymer supercell to evaluate the effects of controlled or uncontrolled surface roughness or structure, as well as different topologies. This can be achieved through tailored deposition and assembly of polymer chains. Additionally, this methodology can be extended to serve as an atomistic numerical reference for sessile droplet experiments in continuum simulations using the phase-field approach, as demonstrated by Jorgensen [64, 65]. In their work, they employed a pseudo-2D atomistic model with a radius similar to that used in continuum simulations, typically in the micrometer range. By employing a coarse-grained (CG) model with atomistic accuracy, it becomes feasible to utilize a full 3D model for the same purpose while significantly reducing the computational time required. As a future perspective, we should also mention the goal of developing the free energy perturbation approach (FEP) described in Chapter 4 for the CG model, to further reduce the computational time required for such simulations.

Chapter 7

Conclusion and perspectives

In this dissertation, we aim to explore the significance of predicting and controlling the wetting behavior of materials to enhance the development of more efficient and effective surfaces. These advancements can lead to improvements in various fields such as energy production, storage, and consumption (e.g., anti-icing, self-cleaning, drag reduction), healthcare (e.g., biomedical membranes), and environmental sustainability (e.g., biodegradability and desalination membranes).

Given the complex and multi-scale nature of interface and wetting phenomena, it is crucial to employ numerical methods that can encompass both discrete and continuum descriptions. This comprehensive approach allows for a better understanding of these phenomena. Consequently, the objective of this thesis is to utilize, combine, and, if necessary, propose and validate new numerical simulation tools to assist the initial stages of surface design and prototyping.

Taking this into consideration, we have introduced an innovative multi-scale framework that aims to predict the wetting characteristics of soft surfaces and 2D materials. The primary goal of this framework is to facilitate the design of surfaces with customized properties. Our proposed methodology combines molecular dynamics (MD) simulations at both atomistic and mesoscopic scales, allowing for seamless integration with continuum simulations and experimental data. This integration enhances the accuracy and quality of surface property analysis and design.

Initially, we concentrate on all-atom (AA) molecular dynamics (MD) simulations of the solid-fluid interface. We assess the wetting properties of PLGA surfaces and graphene using two distinct numerical approaches. These properties include the static

contact angle (CA), work of adhesion (W_{ad}), and interface tension (γ_{sl}). Subsequently, guided by the insights gained from polymer surface investigations, we propose and validate a novel coarse-grained (CG) representation of water and polymers. This representation allows for mesoscopic simulations with quasi-atomistic precision.

Regarding polymer surfaces, we conducted molecular dynamics simulations to replicate sessile droplet experiments. We aimed to propose an integrated methodology that combines simulations with experimental data to predict the wettability of soft interfaces. To illustrate this approach, we focused on Poly(Lactic-co-Glycolic Acid) (PLGA) surfaces, which are commonly used in biomedical and environmentally friendly membranes due to their biodegradable and biocompatible properties. We investigated the wetting behavior of these surfaces using polar and non-polar solvents such as water, formamide, toluene, and hexane. To ensure the reliability of our model, we validated each intermediate step of its development against experimental results. This validation included verifying the surface tension of the probe liquids, as well as assessing the surface topography and the glass transition temperature of the polymer phase. The contact angle (CA) was subsequently calculated through post-processing of the molecular dynamics trajectory. The obtained results demonstrated excellent agreement with experimental measurements, thereby validating our proposed protocol. Furthermore, by thoroughly examining the surface topography and considering interface deformation, we achieved a higher level of accuracy in describing the wettability of soft materials compared to previous studies in the literature. This analysis also allowed us to identify potential nanoscale roughness effects, as observed in the case of formamide.

Graphene, on the other hand, was investigated due to its growing interest in the energy and environmental sectors, particularly as a membrane material for distillation and desalination processes. Additionally, understanding the wetting properties is crucial for determining the adhesion and friction response of fluid phases in contact with graphene, which directly impact mass transport and fluid flow properties. To achieve this, we employed a methodological procedure based on the free energy perturbation (FEP) approach, to calculate the work of adhesion (W_{ad}) and the surface tension of the solid-liquid interface (γ_{sl}). These calculated values are directly correlated to the static and advancing contact angles (CAs) using the Young and Makkonen relations. By applying small perturbations, this approach enables a comprehensive characterization of surfaces using a single model, thereby expediting the simulation process. Similar to the case of polymer surfaces, our

numerical protocol was integrated with experiments. The experiments were used to validate the proposed model and establish a correlation between the nano- and macro-scales, specifically considering graphene layers supported on silica (SiO2) substrates. The calculated values of Wad and the static contact angle, when compared with experimental data, revealed the semi-transparency of a single layer of graphene with respect to the supporting substrate, as also observed in previous studies. As for γ_{sl}, we observed a progressive reduction in value with the addition of more graphene layers. This behavior was also observed experimentally, although there was a consistent shift of approximately 10 mN/m for all the models investigated. This shift can be attributed to the effect of charges on the substrate, which can hinder droplet motion and consequently affect the advancing contact angle. Considering different supporting substrates and their influence on both the static and advancing contact angles will be addressed for future improvements, but it falls beyond the scope of this thesis. Overall, the values obtained using our proposed protocol, which can be applied to different classes of materials, allow for direct characterization of material surfaces, significantly reducing the analysis time.

Despite the high accuracy achieved with the proposed and validated methods, atomistic molecular dynamics (MD) simulations are susceptible to finite-size effects [210]. These limitations include constraints on the size of the investigated surface, maximum realistic roughness modeling on a periodic surface, and the size of droplets, which should not exceed half the periodic box vectors. Additionally, the timescale accessible in MD simulations is typically in the order of 10 ns per sample. To address these challenges, a pseudo-2D model utilizing a periodic cylinder can be adopted to increase droplet size while managing computational costs [64, 65]. However, this approach may introduce significant approximations when considering the effects of random substrate roughness. Another way to overcome the limitations of atomistic models is through coarse-graining, which reduces the resolution and internal degrees of freedom of the system. Coarse-graining allows for accelerated simulations of larger systems while maintaining a reasonable computational cost.

In this perspective, in the context of soft interfaces, we propose and validate a novel coarse-grained (CG) model, known as MOLC, for water and PLGA. This CG model enhances the efficiency and quality of mesoscopic simulations while preserving quasi-atomistic precision. The results demonstrate good agreement with the corresponding atomistic references, validating the proposed CG model. Importantly, the CG structure can be easily reverse-mapped to the atomistic representation and

vice versa, allowing for the adoption of different levels of detail during production runs. By using the water model as an upper limit for the integration time-step (10 fs), we achieve a speed-up factor of 3 to 6 compared to the atomistic model, solely due to the increased integration time-step enabled by coarse-graining. For instance, an accelerated protocol for predicting material and surface properties could involve using CG simulations during stabilization steps while gathering data from reverse-mapped atomistic simulations. We finally conducted simulations of sessile droplet experiments at the coarse-grained (CG) level, considering a system with dimensions equivalent to the atomistic level (approximately 350,000 atoms / 50,000 CG beads) and extending the simulated time to 20 ns. In these simulations, we observed a lower contact angle (CA) compared to the atomistic level. Further analysis and simulations are necessary to comprehensively evaluate wetting properties using this model, including surface topography, roughness, and optimization of the post-process code for CA calculations. Additionally, performing simulations on larger systems to reduce numerical noise inherent in CG droplets would be beneficial and aligns with the motivation behind developing this method.

The differences in spatiotemporal scales between experiments and simulations are the main ones responsible for the intrinsic limitation of atomistic simulations in predicting macroscopic results such as contact angle and more in general wettability and mass transfer properties at the macro-scale. On the other hand continuum simulations, i.e. finite elements or finite volumes, can reproduce macroscopic experiments. For this reason, coupling the two approaches with a standardized and validated protocol can provide a useful tool to predict the wettability properties of structured, non-uniform, or more generally random or tailored surfaces. At the same time, experimental protocols can be adapted, developed, and validated to the micro- and nano-scale, as also recently done by Liimatainen *et al.* [267] and Sbarra *et al.* [268]. Further numerical investigations, on the other hand, can provide information regarding macroscopic wetting phenomena that can be observed at the nano-scale, as recently done by Giacomello *et al.* [269], verifying the Wenzel and Cassie-Baxter state on nano-structured surfaces.

The findings of this thesis have potential implications for bridging the gap between discrete and continuum simulations. The results obtained at the atomistic level can provide boundary conditions for multi-phase continuum simulations. For instance, in the case of structured surfaces, continuum simulations incorporating boundary conditions derived from MD results can be employed (see Fig. 7.1).

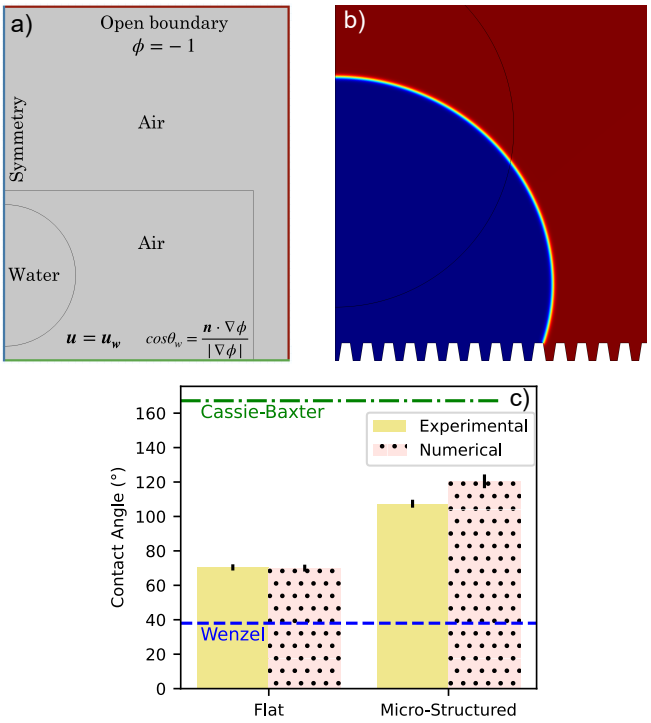

Fig. 7.1 Phase-field model of micro-structured surfaces. (a) Boundary conditions adopted, (b) equilibrium droplet on the micro-structured surface, and (c) contact angle results. Fig. from Ref. [23].

These simulations, based on finite element or volume methods, typically rely on the knowledge of static and advancing contact angles to describe the static and dynamic evolution of the liquid-gas-solid contact line. Additionally, the slip length is necessary to implement the generalized Navier boundary condition (GNBC) considering potential slip conditions at the solid-liquid interface. As demonstrated in the case of graphene, these quantities can be directly obtained from MD simulations using the same stabilized system. The proposed coarse-grained (CG) model can also facilitate the development of large-scale MD systems. To our knowledge, the largest simulated experiment at the atomistic level involved 1.2 million water molecules in a pseudo-2D droplet with a radius of 50 nm. With our CG model, it becomes feasible to create models with dimensions comparable to continuum simulations and experiments, enabling direct comparisons between discrete and continuum results. In this regard, it is worth noting that significant efforts have been dedicated over the past decade to introducing tools for discrete element methods (DEM), such as

LIGGGTHS [270] or the atom to the continuum (ATC) [271] package in LAMMPS, to adopt hybrid MD-CAD and MD-FEM models.

Finally, considering the current level of accuracy supported by validated results over the past decades and the continuous advancements in computational power, numerical simulations are emerging as standalone tools for predicting material properties. This development enhances the speed of prototyping and ultimately reduces the time to market for new components. Additionally, the recent progress in powerful machine learning algorithms and neural networks opens up possibilities for discovering new correlations between chemistry, morphology, and macroscopic properties of materials, thereby revolutionizing the concept of product development. In this context, accurate and accelerated CG simulations, capable of generating massive and reliable databases, are fundamental instruments for the next generation of materials discovery.

Appendix A

LAMMPS codes

In this appendix, we provide information about the files necessary to run MD simulations in LAMMPS, as described in previous chapters. The **.in* files are run directly in LAMMPS using commands such as `mpirun -np #-of-cores lmp\_mpi -in *.in`. The **.init* files include the initialization of the simulation, while the **.settings* files contain interaction parameters between atoms. The **.run* files contain commands related to simulations. The **.data* files contain the initial geometries and topologies of the simulated system.

Due to their length, we do not include the **.data* files in this appendix. However, more detailed files related to the simulations discussed in Chapters 3 and 5 can be found in the Zenodo archives (https://doi.org/10.5281/zenodo.6629427 and https://doi.org/10.5281/zenodo.5552351, respectively). Similarly, more detailed files related to the simulations described in Chapters 4 and 6 will be available in Zenodo repositories after the publication of the associated papers.

A.1 Experimentally-augmented atomistic models for PLGA surfaces

Due to its length, we do not include the **.settings* file in this section of the appendix.

A.1.1 MD PLGA/water sessile experiment

plga_slab01_01.in file

```
# ----------------- Init Section -----------------

include "plga_slab01_01.in.init"

# ----------------- Atom Definition Section -----------------

read_data  "plga_slab01_01.data" extra/atom/types \\
                2 extra/bond/types 1 extra/angle/types 1

replicate 3 3 1

read_data  "water_s01_01.data" add append
                offset 15 11 21 31 0 shift 72.950 72.904 81.0

# ----------------- Settings Section -----------------

include "plga_slab01_01.in.settings"


# ----------------- Run Section -----------------

include "plga_slab01_01.in.run"
```

plga_slab01_01.in.init file

```
atom_style full

variable run string plga_slab01_01
variable temp equal 300.
variable steps equal 49

echo            log
log             ${run}.log

units           real
boundary        p p f
atom_style      full
bond_style      harmonic
angle_style     harmonic
dihedral_style  opls
improper_style  harmonic
pair_style hybrid lj/cut/coul/long 13. &
                lj/cut/tip4p/long/soft 16 17 12 22 0.1546 1 0.5 10 13.
kspace_style pppm/tip4p 1.0e-4
kspace_modify slab 3.0
special_bonds lj 0.0 0.0 0.5 coul 0.0 0.0 0.5 angle yes dihedral yes

# Neighbour list.
neighbor        3.0 bin
neigh_modify every 1 delay 1 check yes
```

plga_slab01_01.in.run file

```
# Physical observables.

# Output.
thermo          1000
thermo_style custom step etotal evdwl ecoul elong ebond ke pe &
temp press vol density cpu
thermo_modify flush yes

dump 1 all dcd 10000 ${run}.dcd
dump_modify     1 unwrap yes
dump 2 all custom 25000 ${run}.dump id mol type q x y z vx vy vz

velocity        all create ${temp} 391624 dist gaussian

fix fShakeSPCE all shake 0.0001 10 0 b 12 a 22

# 2. Thermalisation and relaxation, NPT ensemble, 4 ns.

fix zwalls all wall/reflect zlo EDGE zhi EDGE

fix             3 all nvt temp 300. 300. 100.

run    1000000

write_data droplet_substrate.data nocoeff
```

A.2 Wettability of graphene surfaces predicted by the free energy perturbation

A.2.1 Interface tension γ_{sl}

graphene.in file

```
# ----------------- Init Section -----------------

include "spcfw_graph_01.in.init"


# ----------------- Atom Definition Section ------------------

read_data relaxed_spcfw-graph.data

# ----------------- Settings Section -----------------

include "spcfw_graph_01.in.settings"


# ----------------- Run Section -----------------

include "spcfw_graph_01.in.run"
```

graphene.in.init file

```
atom_style full

variable run  string spcfw_graph_01
variable temp equal 298.
variable steps equal 4
echo            log
log             ${run}.log

# Neighbour list.
neighbor        2.0 bin
neigh_modify    check yes

# Force field definition from the SPCE LT file.
boundary p p p

# -- Default styles for solo "SPC-FW" water --
units        real
atom_style   full
pair_style   lj/cut/coul/long 12.0 12.0
pair_modify tail yes
bond_style   harmonic
angle_style  harmonic
kspace_style pppm 0.0001
```

graphene.in.settings file

```
bond_coeff   1         529.581   1.012
angle_coeff  1         37.95  113.24

pair_coeff   1 1  0.1554253  3.165492
pair_coeff   2 2  0.0     0.0

pair_coeff   3 3  0.0     0.0

pair_coeff   1 2  0.0     0.0
pair_coeff   1 3 0.093690249  3.19
pair_coeff   2 3 0.0  0.0

group spcfw type  1  2
group graph type  3

#fix fShakeSPCE spce shake 0.0001 10 0 b @bond:OH a @angle:HOH
# Remember to "unfix" fShakeSPCE during minimization.
```

gamma_sl.in.run file

```
# Physical observables.

variable Nadaptw  equal 25000
variable Neveryw  equal 1000
variable Nrepeatw equal 25


compute temp_spcfw spcfw temp
compute press_spcfw all pressure temp_spcfw

compute msqdis  all msd com yes

# Output.
thermo          1000
thermo_style custom step etotal evdwl ecoul elong ebond eangle ke pe temp &
c_temp_spcfw press c_press_spcfw vol density &
c_msqdis[1] c_msqdis[2] c_msqdis[3] c_msqdis[4] cpu
thermo_modify flush yes

# Save UNWRAPPED coordinates.
dump 1 all custom 25000 ${run}.dump id type xu yu zu mol
dump 2 all dcd 25000 ${run}.dcd
dump_modify 2 unwrap yes

# 1. Shrink the cell to the target density.

timestep        1.

fix freeze graph setforce 0.0 0.0 0.0

fix             2 spcfw nvt temp ${temp} ${temp} 100.
fix_modify      2 temp temp_spcfw # press press_spcfw

run 1000000

write_data post_relax.data nocoeff

compute TA all fep/ta ${temp} xy 1.0001 tail yes
```

```
fix FEP all ave/time 100 1000 100000 c_TA[] &
ave running file spcfw_fep_ta_0001.txt
fix FEP2 all ave/time 1000 1 1000  c_TA[] &
ave running file spcfw_fep_ta_2_0001.txt

compute TA_neg all fep/ta ${temp} xy 0.9999 tail yes
fix FEP_neg all ave/time 100 1000 100000 c_TA_neg[] &
ave running file spcfw_fep_ta_0001_neg.txt
fix FEP2_neg all ave/time 1000 1 1000  c_TA_neg[] &
ave running file spcfw_fep_ta_2_0001_neg.txt

compute chunks all chunk/atom bin/1d z &
-1.4210854715202004e-14 1.0 units box
compute chunks_water spcfw chunk/atom bin/1d z &
-1.4210854715202004e-14 1.0 units box
compute chunks2 all chunk/atom bin/1d z &
-1.4210854715202004e-14 0.5 units box
compute chunks2_water spcfw chunk/atom bin/1d z &
-1.4210854715202004e-14 0.5 units box

run 10000000

write_data post_test-area_1.data nocoeff
```

A.2.2 Work of adhesion W_{ad}

*.in, *.init, and *.settings files can be taken from the previous section.

W_ad.in.run file

```
# Update positions -----------------------------------------------------

compute temp_spcfw spcfw temp
compute press_spcfw all pressure temp_spcfw

thermo 1000
thermo_style custom step etotal evdwl ecoul elong ebond eangle ke pe &
temp c_temp_spcfw press c_press_spcfw vol density cpu
thermo_modify flush yes


dump 1 all custom 25000 ${run}.dump id type xu yu zu mol

timestep        1.
velocity         all set NULL NULL NULL
velocity        all create ${temp} 353281 dist gaussian

fix mom spcfw momentum 100 linear 1 1 0
fix freeze graph setforce 0.0 0.0 0.0
#fix zwalls all wall/reflect zlo EDGE zhi EDGE
fix             2 spcfw nvt temp ${temp} ${temp} 100.
fix_modify      2 temp temp_spcfw # press press_spcfw

run 1000000

variable Nadapt  equal 800000  # every 800 ps 0.8 ns, adapt value of lambda
variable Nevery  equal     100  # every 100 fs, take a sample
variable Nrepeat equal  3000  # take 3000 samples, over a period of 300 ps &
                this implies that 500 ps are available for equilibration

variable lambda  equal ramp1.0,0.0
variable dlambda equal -0.05

fix ADAPT all adapt/fep ${Nadapt} pair lj/cut/coul/long/soft &
```

```
lambda 1after yes
fix PRINT all print ${Nadapt} "Charge and Lj  adapt lambda = ${lambda} "
compute FEP all fep 300 pair lj/cut/coul/long/soft lambda 1-2 3 v_dlambda
fix FEPAVE all ave/time ${Nevery} ${Nrepeat} ${Nadapt} c_FEP[1] c_FEP[2] &
                                        file fep_PLGA_12_spcfw.lmp

run    16000000

write_data after_fep.data nocoeff
```

A.3 Coarse-grained water models with enhanced accuracy and speed-up factor

A.3.1 Typical CG run with MOLC

tip4p_CG.in file

```
# ----------------- Init Section -----------------

include "tip4p_CG.in.init"


# ----------------- Atom Definition Section -----------------

read_data "tip4p_m1000_01.data"

# ----------------- Settings Section -----------------

include "tip4p_CG.in.settings"


# ----------------- Run Section -----------------

include "tip4p_CG.in.run"
```

tip4p_CG.in.init file

```
variable run  string tip4p_m1000_01
variable temp equal 298.
variable steps equal 5
echo            log
log             ${run}.log
units           real
boundary        p p p
atom_style      hybrid molecular ellipsoid

# Neighbour list.
neighbor        4.0 bin
neigh_modify    check yes
```

tip4p_CG.in.settings file

```
     mass 1  18.0152

pair_style hybrid/overlay gayberne 1 1 -3 14 &
        coul/long/offcentre 14 3 1 0.75695 0.585882 0.0 &
        0.5564 1 -0.75695 0.585882 0.0 0.5564 1 0.00000 0.154600 &
    0.0 -1.1128

kspace_style pppm/offcentre 1e-4 3 1 0.75695 &
        0.585882 0.0 0.5564 1 -0.75695 0.585882 0.0 &
        0.5564 1 0.00000 0.154600 0.0 -1.1128

# Pair coefficients: Coulomb and Gay-Berne parameters.
pair_coeff pair_coeff 1 1 gayberne 0.18519 3.1589 1 1 1 1 1 1 14.
```

tip4p_CG.in.run file

```
# Physical observables.
compute q               all property/atom quatw quati quatj quatk
compute shape           all property/atom shapex shapey shapez
compute msqdis          all msd com yes
compute temp_trasl      all temp
compute temp_rototrasl  all temp/asphere dof all
compute press_trasl     all pressure temp_trasl

# Output.
thermo       1000
thermo_style custom step etotal evdwl ecoul elong ebond ke pe &
        temp press vol density &
        c_msqdis[1] c_msqdis[2] c_msqdis[3] c_msqdis[4] cpu
thermo_modify temp temp_rototrasl
thermo_modify press press_trasl
thermo_modify flush yes

# Save UNWRAPPED coordinates.
dump 1 all custom 1000 ${run}.dump &
id type xu yu zu c_q[1] c_q[2] c_q[3] c_q[4] &
c_shape[1] c_shape[2] c_shape[3] vx vy vz &
angmomx angmomy angmomz mol

# 1. Shrink the cell to the target density.
timestep        10.
velocity        all create ${temp} 391624 dist gaussian
fix             2 all nve/asphere
fix             3 all langevin ${temp} ${temp} 1000. 35785 angmom 0.9
fix_modify      3 temp temp_rototrasl
fix             4 all deform 1 x scale .95 y scale .95 z scale .95 &
units box remap x

# 100 ps per cycle.

label    cycle1
variable i loop ${steps}
  print "  run    10000
  next   i
```

```
jump SELF cycle1
variable i delete

# 2. Thermalisation and relaxation, NPT ensemble, 4 ns.
unfix 2
unfix 4
fix             2 all nph/asphere iso 1. 1. 10000.
fix_modify      2 press press_trasl
run    400000
```

A.4 Coarse-grained polymers models: the case study of PLGA

A.4.1 Thermal conductivity

plga_CG.in file

```
# ----------------- Init Section -----------------

include "plga_CG.in.init"


# ----------------- Atom Definition Section -----------------

read_data "plga_CG.data"

# ----------------- Settings Section -----------------

include "plga_CG.in.settings"


# ----------------- Run Section -----------------

include "plga_CG_therm.in.run"
```

plga_CG.in.init file

```
variable run string plga_s04_02
variable temp equal 300.
variable Th equal 320.
variable Tc equal 280.
variable steps equal 49
#        [J/K]        Boltzmann
variable        kB        equal        1.38e-23
# conversion from kcal/mol to Joules including Avogadro
variable        kcal_mol2J        equal        6.95e-21
variable        binnumber        equal        20
variable        BoxDimZ        equal        lz
variable        BoxDimX        equal        lx
variable        BoxDimY        equal        ly

echo            log
log             ${run}.log
units           real
boundary        p p p
atom_style      hybrid molecular ellipsoid

# Neighbour list.
neighbor        5.0 bin
neigh_modify    check yes
```

plga_CG.in.settings file

```
    mass 1 72.0634
    mass 2  58.0366

pair_style hybrid/overlay gayberne 1 1 -3 14 &
        coul/long/offcentre 14 7 1 1.931251 0.539650 1.011545 0.0668 1 &
        0.446082 0.057700 -0.000000 0.6529 1 -0.712230 1.072980 0.000000 &
        -0.4227 1 -0.653529 -1.140853 0.000000 -0.2970 2 -0.422955 -1.245763 &
         0.000000 -0.313 2 0.527142 0.083536 0.000000 0.716 2 &
    -0.856806 0.981621 0.000000 -0.403

kspace_style pppm/offcentre 1e-4 7 1 1.931251 0.539650 1.011545 0.0668 &
        1 0.446082 0.057700 -0.000000 0.6529 1 -0.712230 1.072980 0.000000 &
        -0.4227 1 -0.653529 -1.140853 0.000000 -0.2970 2 -0.422955 -1.245763 &
        0.000000 -0.313 2 0.527142 0.083536 0.000000 0.716 2 -0.856806 0.981621 &
    0.000000 -0.403

# Pair coefficients: Coulomb and Gay-Berne parameters.
pair_coeff pair_coeff 1 2 gayberne 1.03684 3.4086 0.97313 1 0.36835 &
    0.53249 0.53249 1 14.
pair_coeff 1 1 gayberne 1.0627 3.4740 0.97313 1 0.36835 0.97313 1 0.36835 14.
pair_coeff 2 2 gayberne 1.0116 3.3432 0.53249 0.53249 1 0.53249 0.53249 1 14.

    bond_style ellipsoid
    special_bonds lj/coul 0.0 0.2 0.5

    bond_coeff 1     &
    poly 2 0   -0.90854   -3.67091    21.0619    3.46926 &
    cos  2 0   0.468392     1.5682    0.77494          0 &
    cos  2 0   0.051231    1.55637   0.368657          0 &
    cos  2 0   -0.63579    1.57002   -0.40024          0 &
    cos  1 0  -0.291573       1.57                       &
    cos  2 0 -0.0454135    1.56739  -0.159876          0 &
    cos  2 0  0.0689315    1.56411   0.326725          0 &
    cos  2 0 -0.0380405    1.56469  -0.222524          0 &
    cos  1 0   0.214176    1.57072                       &
    cos  2 0    0.06476      1.555   0.672605          0 &
    poly 2 0    0.63728    2.15358     35.456   0.284144 &
    cos  1 0    1.06641     4.7121                       &
```

```
poly 0 0                                                &
poly 2 0    1.09113    2.29165    13.2812   1.04108    &
poly 2 0    1.29123    1.05776    4.62779   0.409837 &
poly 2 0    1.71005    1.02317    12.3945 -0.0340389
```

plga_CG_therm.in.run file

```
# Physical observables.
compute q          all property/atom quatw quati quatj quatk
compute shape           all property/atom shapex shapey shapez
compute temp_trasl      all temp
compute temp_rot        all temp/asphere dof rotate
compute temp_rototrasl  all temp/asphere dof all
compute press_trasl     all pressure temp_trasl
#compute inter all inter/molc kspace yes

# Output.
thermo          1000
thermo_style custom step etotal evdwl ecoul elong ebond ke pe &
                                temp press pxx pyy pzz vol density cpu
thermo_modify temp temp_rototrasl
thermo_modify press press_trasl
thermo_modify flush yes

dump 1 all custom 10000 ${run}.dump &
id type xu yu zu c_q[1] c_q[2] c_q[3] c_q[4] &
c_shape[1] c_shape[2] c_shape[3] vx vy vz &
angmomx angmomy angmomz mol

# 1. Initial Thermalization
timestep        10.
velocity        all create ${temp} 391624 dist gaussian
fix             2 all nve/asphere
fix             3 all langevin ${temp} ${temp} 1000. 35785 angmom 0.9
fix_modify      3 temp temp_rototrasl
run 20000

unfix 2
unfix 3
reset_timestep 0

# Thermal Conductivity--------------------------------------------------------------------

variable        binnumber equal 21
variable        BoxDimX equal "lx"
```

```
variable        BoxDimXmin equal "xlo"
variable        BoxDimXmax equal "xhi"
variable        midBoxDimX equal ${BoxDimXmax}-${BoxDimX}/2.0 #
variable        bindelta equal ${BoxDimX}/${binnumber}

variable        BoxDimXminplusdelta equal ${BoxDimXmin}+${bindelta}/2

variable        midBoxDimXplusdelta equal ${midBoxDimX}+${bindelta}/2

variable        midBoxDimXminusdelta equal ${midBoxDimX}-${bindelta}/2

variable        BoxDimXmaxminusdelta equal ${BoxDimXmax}-${bindelta}/2

region          Regioncoldleft block ${BoxDimXmin} ${BoxDimXminplusdelta} &
                        INF INF INF INF units box
region          Regioncoldright block ${BoxDimXmaxminusdelta} ${BoxDimXmax} &
                        INF INF INF INF units box
region          Regionhot block ${midBoxDimXminusdelta} ${midBoxDimXplusdelta} &
                        INF INF INF INF units box

group               Grouphot region Regionhot
group               Groupcoldleft region Regioncoldleft
group       Groupcoldright region Regioncoldright

compute         TRhoT Grouphot temp/asphere dof all
compute         TRcoldleft Groupcoldleft temp/asphere dof all
compute         TRcoldright Groupcoldright temp/asphere dof all

fix               1 all nve/asphere

fix             Lgvhot Grouphot langevin ${Th} ${Th} 1000 35785 angmom 0.9
fix             Lgvcoldleft Groupcoldleft langevin ${Tc} ${Tc} 1000 35785 angmom 0.9
fix             Lgvcoldright Groupcoldright langevin ${Tc} ${Tc} 1000 35785 angmom 0.9
fix_modify      Lgvhot temp TRhoT
fix_modify      Lgvcoldleft temp TRcoldleft
fix_modify      Lgvcoldright temp TRcoldright

variable        deltaTleft equal c_TRhot-c_TRcoldleft
variable        deltaTright equal c_TRhot-c_TRcoldright

run 100000

unfix             Lgvhot
```

```
unfix             Lgvcoldleft
unfix             Lgvcoldright
unfix             1

# Temperature profile ---------------------------------------------------------

fix                2 all nve/asphere

compute                Ktrasl all ke/atom
compute         KErot  all erotate/asphere/atom
variable        TPA_trasl atom c_Ktrasl${kcal_mol2J}
variable        TPA_rot   atom c_KErot${kcal_mol2J}
variable        TPA_rototrasl   atom &
    [c_KErot${kcal_mol2J}+c_Ktrasl${kcal_mol2J}]/[3${kB}]


compute layers all chunk/atom bin/1d x lower ${bindelta} units box
fix aveTPA1 all ave/chunk 10 50 500 layers v_TPA_rototrasl file temp_prof.txt
fix aveTPA2 all ave/chunk 10 50 500 layers v_TPA_trasl file temp_prof_trasl.txt
fix aveTPA3 all ave/chunk 10 50 500 layers v_TPA_rot file temp_prof_rot.txt

# Langevin --------------------------------------------------------------------

fix             Lgvhot Grouphot langevin ${Th} ${Th} 1000 35785 angmom 0.9 tally yes
fix             Lgvcoldleft Groupcoldleft langevin ${Tc} ${Tc} 1000 35785 &
    angmom 0.9 tally yes
fix             Lgvcoldright Groupcoldright langevin ${Tc} ${Tc} 1000 35785 &
    angmom 0.9 tally yes
fix_modify      Lgvhot temp TRhoT
fix_modify      Lgvcoldleft temp TRcoldleft
fix_modify      Lgvcoldright temp TRcoldright

variable        EnergyExchange equal 0.5fix heatflux all ave/time 10 50 500 &
    v_EnergyExchange file HeatFlux.dat

run        200000
```

A.4.2 Elastic properties

*.in, *.init, and *.settings files can be taken from the previous section.

plga_CG_mech.in.run file

```
# Physical observables.
compute q          all property/atom quatw quati quatj quatk
compute shape           all property/atom shapex shapey shapez
compute temp_trasl      all temp
compute temp_rot        all temp/asphere dof rotate
compute temp_rototrasl  all temp/asphere dof all
compute press_trasl     all pressure temp_trasl
compute press_rototrasl     all pressure temp_rototrasl

variable     tmp     equal lx
variable     lx0     equal ${tmp}
variable     tmp     equal ly
variable     ly0     equal ${tmp}
variable     tmp     equal lz
variable     lz0     equal ${tmp}

variable     etotal  equal etotal/atoms #eV/atom
variable     pe      equal     pe/atoms #eV/atom
variable     ke      equal     ke/atoms #eV/atom
variable     strainx equal lx-${lx0}/${lx0}
variable     strainy equal ly-${ly0}/${ly0}
variable     strainz equal lz-${lz0}/${lz0}
variable     stressx equal -c_press_rototrasl[1]${fpress} #GPa
variable     stressy equal -c_press_rototrasl[2]${fpress} #GPa
variable     stressz equal -c_press_rototrasl[3]${fpress} #GPa

# Output.
timestep         10.
thermo          100
thermo_style custom step etotal evdwl ecoul elong ebond ke pe &
    temp press vol density cpu
thermo_modify temp temp_rototrasl
thermo_modify press press_trasl
thermo_modify flush yes
```

```
# 1. Aniso relaxation.
#velocity        all create ${temp} 391624 dist gaussian
#fix                  2 all nph/asphere aniso 1. 1. 5000.
#fix             3 all langevin ${temp} ${temp} 500. 35785 angmom 0.9
#fix_modify      3 temp temp_rototrasl

#run 200000

#unfix 2
#unfix 3

#reset_timestep 0

dump 1 all custom 500 ${run}.dump &
id type xu yu zu c_q[1] c_q[2] c_q[3] c_q[4] &
c_shape[1] c_shape[2] c_shape[3] vx vy vz &
angmomx angmomy angmomz mol

# 2. Uniaxial tensile test

fix          boxdeform all deform 1 x erate 0.0000001 remap x
fix          2 all npt/asphere temp ${temp} ${temp} 1000. &
    y 0. 0. 10000. z 0. 0. 10000.
fix_modify   2 temp temp_rototrasl press press_trasl
fix              def_print all print 50 "${strainx} ${stressx} &
    ${strainy} ${stressy} ${strainz} ${stressz}" &
    file stress-strain.txt screen no
run          100000
```

Nomenclature

Roman Symbols

$\mathbf{a}$	Acceleration vector	$[m\ s^{-2}]$
$\mathbf{v}$	Velocity vector	$[m\ s^{-1}]$
ΔH_{vap}	Enthalpy of vaporisation	$[J\ mol^{-1}]$
ΔP	Pressure Difference	$[Pa]$
ΔT	Temperature Difference	$[K]$
$\mathbf{F}$	Force vector	$[N]$
$\mathbf{f}_t$	Transversal force acting at the solid-liquid interface	$[N]$
$\mathbf{P}$	Pressure tensor	$[Pa]$
$\mathbf{Q}$	Orientation vector	$[rad$ or $^\circ]$
$\mathbf{r}$	Position vector	$[m]$
∇T	Temperature gradient	$[K\ m^{-1}]$
A	Area	$[m^2]$
b	Slip Length	$[m]$
D	Self-diffusion coefficient	$[m^2\ s^{-1}]$
E	Elastic modulus	$[Pa]$
F	Helmotz free energy	$[J]$

f	Friction coefficient	$[Pa\ s\ m^{-1}]$
F_a	Resisting force at the contact line	$[N]$
F_a	Resisting force per unit of contact line	$[N\ m^{-1}]$
f_{sg}	Liquid fraction in contact with trapped air	$[-]$
f_{sl}	Liquid fraction in contact with the solid substrate	$[-]$
G	Gibbs free energy (Chapter 1)	$[J]$
G	Shear modulus (Chapter 6)	$[Pa]$
g	Gravitational acceleration	$[m\ s^{-2}]$
I	Moment of inertia	$[kg\ m^2]$
N	Number of particles	$[-]$
P	Pressure	$[Pa]$
q_i	Electric charge	$[C]$
r	Wenzel roughness factor	$[-]$
R_c	Capillary length	$[m]$
r_c	Radius of the contact line	$[m]$
R_i	Local radii of curvature	$[m]$
T	Temperature	$[K]$
T_g	Glass transition temperature	$[K]$
U	Potential energy	$[J]$
V	Volume	$[m^3]$
$\mathbf{q}$	Specific heat flux vector	$[W\ m^{-2}]$
k_B	Boltzmann constant	$[J\ K^{-1}]$
W_{ad}	Work Of Adhesion	$[N\ m^{-1}]$

Greek Symbols

ε	Lennard-Jones well depth	$[kcal\ mol^{-1}]$
η	Dynamic viscosity	$[Pa\ s]$
γ	Interface tension	$[N\ m^{-1}]$
γ_{lv}	Liquid-vapour interface tension	$[N\ m^{-1}]$
γ_{sl}	Solid-liquid interface tension	$[N\ m^{-1}]$
γ_{sv}	Solid-vapour interface tension	$[N\ m^{-1}]$
λ	Coupling parameter in free energy perturbation	$[-]$
λ_c	Thermal conductivity	$[W\ m^{-1}\ K^{-1}]$
ν	Poisson ratio	$[-]$
ω	Rotational velocity	$[rad\ s^{-1}]$
ρ	Density	$[kg\ m^{-3}]$
σ	Lennard-Jones collision diameter	[Å]
θ_A	Advancing CA	[*rad* or °]
θ_R	Receding CA	[*rad* or °]
θ_W	Wenzel contact angle	[*rad* or °]
θ_{CB}	Cassie-Baxter contact angle	[*rad* or °]
θ_Y	Young or intrinsic CA	[*rad* or °]

Acronyms / Abbreviations

AFM	Atomic Force Microscopy
CA	Contact Angle
CB	Cassie-Baxter
CG	Coarse-Graining

DOF Degrees of Freedom

FEP Free Energy Perturbation

GA Glycolic Acid

KE Kinetic Energy

LA Lactic Acid

LJ Lennard-Jones

MD Molecular Dynamics

NPT Isothermal-isobaric ensemble

NVE Micro-canonical ensemble

NVT Canonical ensemble

PLGA Poly(Lactic-co-Glycolic Acid)

SAS Solvent Accessible Surface

SFE Surface Free Energy

vdW van der Waals

LSL Liquid-Solid-Liquid

LSV Liquid-Solid-Vapour

RDF Radial Distribution Function

List of Figures

1.1 Multi-scale Workflow 13

2.1 Basic concepts of wetting 20

2.2 Advancing contact angle measurment 21

2.3 Wenzel and Cassie-Baxter states 22

2.4 Graphical representation of LJ (a) and Coulomb (b) potentials for different values of λ. 36

2.5 Diagram showing two off–centre charges, in blue and red, defined for two ellipsoids. Fig. from Ref. [2] 39

3.1 Soft surface and liquids considered in the MD simulations. 45

3.2 MD snapshot of the initial configuration of a water/PLGA sample . 46

3.3 PLGA Glass transition temperature and PLGA/water density profile 50

3.4 Numerical and experimental surface topography 53

3.5 MD Tip4P-05 apparent contact angle 55

3.6 MD SPC-E apparent contact angle 56

3.7 Experimental formamide droplet on the flat PLGA specimen 57

3.8 MD formamide apparent contact angle 58

3.9 MD formamide apparent contact angle with 10 wt% of water 58

3.10 MD formamide apparent contact angle with 20 wt% of water 59

3.11 Experimental toluene droplet on the flat PLGA specimen 60

3.12 MD toluene apparent contact angle 61
3.13 MD hexane apparent contact angle 62
3.14 Experimental / numerical wetting properties of the PLGA and fluids. 63

4.1 Asymmetric and Symmetric Graphene/Water Interface Models . . . 70
4.2 FEP Approach for Interface Tension and Work of Adhesion 73
4.3 Surface tension of water γ_{lv}. 75
4.4 Water density profile at the graphene/water interface 76
4.5 Water/graphene interface W_{ad} and γ_{sl} 77
4.6 Cumulative average of γ_{sl} 78
4.7 Water/graphene interface W_{ad} and γ_{sl} for multi-layer models 79
4.8 Cumulative average of γ_{sl} for multi-layer models 79
4.9 Numerical vs experimental W_{ad} and γ_{sl} for multi-layer models . . . 82
4.10 Viscosity of SPC-fW water model and friction coefficient 83

5.1 Water CG model 86
5.2 Schematic view of the AA and CG water models. 88
5.3 Initial and condensed states for a sample of 1000 CG water molecules 89
5.4 AA and CG back-mapped water radial distribution functions 93
5.5 CG water properties computed with integration timestep of 1 fs . . . 94
5.6 Integrated ACF for the evaluation of the dynamic viscosity 96
5.7 Mean square displacements of water molecules 97
5.8 CG water properties computed with integration timestep of 10 f . . . 99
5.9 Wall time ratio and Speed-up factor between the CG and AA models 101
5.10 Variation of mass to increase the integration timestep. 102
5.11 Variation of dynamic viscosity for different water masses and timesteps 103

6.1 Coupled PLGA/water CG model 106

6.2 PLGA CG chain and configurations 107
6.3 Setup employed to compute λ_c by NEMD methods 109
6.4 Pictorial view of the stress-strain test on the CG model 112
6.5 Example of stress-strain curves from CG simulations 112
6.6 Glass Transition Temperature of CG models 114
6.7 Example of temperature profile of CG PLGA model 115
6.8 Example of temperature profile of AA PLGA model 115
6.9 Thermal conductivity comparison between AA and CG models . . . 116
6.10 Elastic properties comparison between AA and CG models 117
6.11 CG MD water apparent contact angle - amorphous 119
6.12 CG MD water apparent contact angle - semi-crystalline 120

7.1 Phase-field model of micro-structured surfaces 127

List of Tables

3.1 MD liquid density, surface tension and CA 52

3.2 Apparent and Young CA of water and formamide 53

3.3 Experimental CA and Surface Free Energy (SFE) of flat PLGA sample 55

4.1 Graphene/water models studied 70

4.2 W_{ad} and γ_{sl} of mono- and multi-layer graphene/water interface . . . 80

5.1 CG water properties computed with integration timestep of 1 f . . . 95

5.2 CG water properties computed with integration timestep of 10 f . . . 98

5.3 Enthalpy of vaporization of CG water model 100

References

[1] Francesco Maria Bellussi, Otello Maria Roscioni, Edoardo Rossi, Annalisa Cardellini, Marina Provenzano, Luca Persichetti, Valeriya Kudryavtseva, Gleb Sukhorukov, Pietro Asinari, Marco Sebastiani, et al. Wettability of soft plga surfaces predicted by experimentally augmented atomistic models. *MRS Bulletin*, 48:108–117, 2022.

[2] Francesco Maria Bellussi, Otello Maria Roscioni, Matteo Ricci, and Matteo Fasano. Anisotropic electrostatic interactions in coarse-grained water models to enhance the accuracy and speed-up factor of mesoscopic simulations. *J. Phys. Chem. B*, 125(43):12020–12027, 2021.

[3] Tim Wolfer, Patrick Bollgruen, Dario Mager, Ludger Overmeyer, and Jan G Korvink. Printing and preparation of integrated optical waveguides for optronic sensor networks. *Mechatronics*, 34:119–127, 2016.

[4] Dengke Chen, Yang Liu, Huawei Chen, and Deyuan Zhang. Bio-inspired drag reduction surface from sharkskin. *Biosurface and Biotribology*, 4(2):39–45, 2018.

[5] Chao-Hua Xue, Hui-Gui Li, Xiao-Jing Guo, Ya-Ru Ding, Bing-Ying Liu, Qiu-Feng An, and Yingtang Zhou. Superhydrophobic anti-icing coatings with self-deicing property using melanin nanoparticles from cuttlefish juice. *Chemical Engineering Journal*, 424:130553, 2021.

[6] Kesong Liu and Lei Jiang. Bio-inspired self-cleaning surfaces. *Annual Review of Materials Research*, 42:231–263, 2012.

[7] Sing Shy Liow, Anis Abdul Karim, and Xian Jun Loh. Biodegradable thermogelling polymers for biomedical applications. *MRS Bull.*, 41(7):557–566, 2016.

[8] Albert Boretti, Sarim Al-Zubaidy, Miroslava Vaclavikova, Mohammed Al-Abri, Stefania Castelletto, and Sergey Mikhalovsky. Outlook for graphene-based desalination membranes. *npj Clean Water*, 1(1):5, 2018.

[9] Yihan Sun and Zhiguang Guo. Recent advances of bioinspired functional materials with specific wettability: from nature and beyond nature. *Nanoscale Horizons*, 4(1):52–76, 2019.

[10] Ming Li, Chang Li, Bamber RK Blackman, and Saiz Eduardo. Mimicking nature to control bio-material surface wetting and adhesion. *International Materials Reviews*, 67(6):658–681, 2022.

[11] Lin Feng, Yanan Zhang, Jinming Xi, Ying Zhu, Nü Wang, Fan Xia, and Lei Jiang. Petal effect: a superhydrophobic state with high adhesive force. *Langmuir*, 24(8):4114–4119, 2008.

[12] Thierry Darmanin and Frédéric Guittard. Superhydrophobic and superoleophobic properties in nature. *Materials today*, 18(5):273–285, 2015.

[13] Dehui Wang, Qiangqiang Sun, Matti J Hokkanen, Chenglin Zhang, Fan-Yen Lin, Qiang Liu, Shun-Peng Zhu, Tianfeng Zhou, Qing Chang, Bo He, et al. Design of robust superhydrophobic surfaces. *Nature*, 582(7810):55–59, 2020.

[14] Dhriti Nepal, Saewon Kang, Katarina M Adstedt, Krishan Kanhaiya, Michael R Bockstaller, L Catherine Brinson, Markus J Buehler, Peter V Coveney, Kaushik Dayal, Jaafar A El-Awady, et al. Hierarchically structured bioinspired nanocomposites. *Nature materials*, pages 1–18, 2022.

[15] Cunming Yu, Srdjan Sasic, Kai Liu, Samir Salameh, Robin HA Ras, and J Ruud van Ommen. Nature–inspired self–cleaning surfaces: Mechanisms, modelling, and manufacturing. *Chemical Engineering Research and Design*, 155:48–65, 2020.

[16] Amirul Syafiq, Vengadaesvaran Balakrishnan, Mohd Syukri Ali, Sanjay J Dhoble, Nasrudin Abd Rahim, Azimah Omar, et al. Application of transparent self-cleaning coating for photovoltaic panel: A review. *Current Opinion in Chemical Engineering*, 36:100801, 2022.

[17] Monojit Chakraborty, Justin A Weibel, James A Schaber, and Suresh V Garimella. The wetting state of water on a rose petal. *Advanced Materials Interfaces*, 6(17):1900652, 2019.

[18] Marleen Kamperman, Elmar Kroner, Aránzazu Del Campo, Robert M McMeeking, and Eduard Arzt. Functional adhesive surfaces with "gecko" effect: The concept of contact splitting. *Advanced Engineering Materials*, 12(5):335–348, 2010.

[19] Luciano F Boesel, Christian Greiner, Eduard Arzt, and Aránzazu Del Campo. Gecko-inspired surfaces: a path to strong and reversible dry adhesives. *Advanced Materials*, 22(19):2125–2137, 2010.

[20] Gregory D Bixler and Bharat Bhushan. Bioinspired rice leaf and butterfly wing surface structures combining shark skin and lotus effects. *Soft matter*, 8(44):11271–11284, 2012.

[21] Samaneh Bandehali, Hamidreza Sanaeepur, Abtin Ebadi Amooghin, Saeed Shirazian, and Seeram Ramakrishna. Biodegradable polymers for membrane separation. *Separation and Purification Technology*, 269:118731, 2021.

[22] Vilim Filipovic, Keith L Bristow, Lana Filipovic, Yusong Wang, Henry Y Sintim, Markus Flury, and Jiri Simunek. Sprayable biodegradable polymer membrane technology for cropping systems: Challenges and opportunities. *Environmental Science & Technology*, 54(8):4709–4711, 2020.

[23] Marina Provenzano, Francesco Maria Bellussi, Matteo Morciano, Edoardo Rossi, Mario Schleyer, Pietro Asinari, Thomas Straub, Marco Sebastiani, and Matteo Fasano. Experimentally validated phase-field model to design the wettability of micro-structured surfaces. *Materials & Design*, page 112042, 2023.

[24] Xiaobin Yang, Linlin Yan, Jun Ma, Yongping Bai, and Lu Shao. Bioadhesion-inspired surface engineering constructing robust, hydrophilic membranes for highly-efficient wastewater remediation. *Journal of Membrane Science*, 591:117353, 2019.

[25] Song Zhang, Mingchao Chi, Jilong Mo, Tao Liu, Yanhua Liu, Qiu Fu, Jinlong Wang, Bin Luo, Ying Qin, Shuangfei Wang, et al. Bioinspired asymmetric amphiphilic surface for triboelectric enhanced efficient water harvesting. *Nature communications*, 13(1):4168, 2022.

[26] Hyeongyun Cha, Hamed Vahabi, Alex Wu, Shreyas Chavan, Moon-Kyung Kim, Soumyadip Sett, Stephen A Bosch, Wei Wang, Arun K Kota, and Nenad Miljkovic. Dropwise condensation on solid hydrophilic surfaces. *Science advances*, 6(2):eaax0746, 2020.

[27] Shuang Zhao, Chenghao Jiang, Jingcun Fan, Shanshan Hong, Pei Mei, Ruxin Yao, Yilin Liu, Sule Zhang, Hui Li, Huaqian Zhang, et al. Hydrophilicity gradient in covalent organic frameworks for membrane distillation. *Nature Materials*, 20(11):1551–1558, 2021.

[28] Sean C O'Hern, Doojoon Jang, Suman Bose, Juan-Carlos Idrobo, Yi Song, Tahar Laoui, Jing Kong, and Rohit Karnik. Nanofiltration across defect-sealed nanoporous monolayer graphene. *Nano letters*, 15(5):3254–3260, 2015.

[29] David Cohen-Tanugi and Jeffrey C Grossman. Water desalination across nanoporous graphene. *Nano letters*, 12(7):3602–3608, 2012.

[30] Liang Chen, Guosheng Shi, Jie Shen, Bingquan Peng, Bowu Zhang, Yuzhu Wang, Fenggang Bian, Jiajun Wang, Deyuan Li, Zhe Qian, et al. Ion sieving in graphene oxide membranes via cationic control of interlayer spacing. *Nature*, 550(7676):380–383, 2017.

[31] Jijo Abraham, Kalangi S Vasu, Christopher D Williams, Kalon Gopinadhan, Yang Su, Christie T Cherian, James Dix, Eric Prestat, Sarah J Haigh, Irina V Grigorieva, et al. Tunable sieving of ions using graphene oxide membranes. *Nature nanotechnology*, 12(6):546–550, 2017.

[32] Thomas Young. III. An essay on the cohesion of fluids. *Philos. Trans. R. Soc. Lond.*, 95:65–87, 1805.

[33] Edward Bormashenko. General equation describing wetting of rough surfaces. *J. Colloid Interface Sci.*, 360(1):317–319, 2011.

[34] Robert N. Wenzel. Resistance of solid surfaces to wetting by water. *Ind. Eng. Chem.*, 28(8):988–994, 1936.

[35] A. B. D. Cassie and S. Baxter. Wettability of porous surfaces. *Trans. Faraday Soc.*, 40:546–551, 1944.

[36] Hongyi Liu, Yan Li, Wendy E Krause, Orlando J Rojas, and Melissa A Pasquinelli. The soft-confined method for creating molecular models of amorphous polymer surfaces. *J. Phys. Chem. B*, 116(5):1570–1578, 2012.

[37] Chongqin Zhu, Yurui Gao, Hui Li, Sheng Meng, Lei Li, Joseph S Francisco, and Xiao Cheng Zeng. Characterizing hydrophobicity of amino acid side chains in a protein environment via measuring contact angle of a water nanodroplet on planar peptide network. *Proc. Natl. Acad. Sci. U.S.A.*, 113(46):12946–12951, 2016.

[38] Sai Ankit Etha, Parth Rakesh Desai, Harnoor Singh Sachar, and Siddhartha Das. Wetting dynamics on solvophilic, soft, porous, and responsive surfaces. *Macromolecules*, 54(2):584–596, 2021.

[39] Thibaud Dreher, Claire Lemarchand, Nicolas Pineau, Emeric Bourasseau, Aziz Ghoufi, and Patrice Malfreyt. Calculation of the interfacial tension of the graphene-water interaction by molecular simulations. *The Journal of chemical physics*, 150(1):014703, 2019.

[40] Mara Chiricotto, Fausto Martelli, Giuliana Giunta, and Paola Carbone. Role of long-range electrostatic interactions and local topology of the hydrogen bond network in the wettability of fully and partially wetted single and multilayer graphene. *The Journal of Physical Chemistry C*, 125(11):6367–6377, 2021.

[41] Jie Pan. Scaling up system size in materials simulation. *Nature Computational Science*, 1(2):95–95, 2021.

[42] Yanzi Gao, Wenhuan Yao, Jian Sun, Huimin Zhang, Zhendong Wang, Ling Wang, Dengke Yang, Lanying Zhang, and Huai Yang. A novel soft matter composite material for energy-saving smart windows: from preparation to device application. *J. Mater. Chem. A*, 3:10738–10746, 2015.

[43] Nicolas Cottenye, Karine Anselme, Lydie Ploux, and Corinne Vebert-Nardin. Vesicular structures self-assembled from oligonucleotide-polymer hybrids: Mechanical prevention of bacterial colonization upon their surface tethering through hybridization. *Adv. Funct. Mater.*, 22(23):4891–4898, 2012.

[44] Annalisa Cardellini, Matteo Fasano, Eliodoro Chiavazzo, and Pietro Asinari. Interfacial water thickness at inorganic nanoconstructs and biomolecules: Size matters. *Phys. Lett. A*, 380(20):1735–1740, 2016.

[45] Qin Chen, Xinyue Zhang, Kai Chen, Xiaofang Wu, Tian Zong, Cunao Feng, and Dekun Zhang. Anisotropic hydrogels with enhanced mechanical and tribological performance by magnetically oriented nanohybrids. *Chem. Eng. J.*, 430:133036, 2022.

[46] Joseph E Mates, Ramsey Ibrahim, Alejandro Vera, Stephen Guggenheim, Jian Qin, Debbie Calewarts, Don E Waldroup, and Constantine M Megaridis. Environmentally-safe and transparent superhydrophobic coatings. *Green Chem.*, 18(7):2185–2192, 2016.

[47] Deepti Ballal and Walter G Chapman. Hydrophobic and hydrophilic interactions in aqueous mixtures of alcohols at a hydrophobic surface. *J. Chem. Phys.*, 139(11):114706, 2013.

[48] Hao-Cheng Yang, Yunsong Xie, Henry Chan, Badri Narayanan, Lin Chen, Ruben Z Waldman, Subramanian KRS Sankaranarayanan, Jeffrey W Elam, and Seth B Darling. Crude-oil-repellent membranes by atomic layer deposition: oxide interface engineering. *ACS Nano*, 12(8):8678–8685, 2018.

[49] Matteo Fasano, Alessio Bevilacqua, Eliodoro Chiavazzo, Thomas Humplik, and Pietro Asinari. Mechanistic correlation between water infiltration and framework hydrophilicity in mfi zeolites. *Sci. Rep.*, 9(1):1–12, 2019.

[50] Panlong Wang, Guoqiang Zheng, Kun Dai, Chuntai Liu, and Changyu Shen. Programmable micropatterned surface for single-layer homogeneous-polymer janus actuator. *Chem. Eng. J.*, 430:133052, 2022.

[51] Regina Mažeikienė, Gediminas Niaura, and Albertas Malinauskas. Poly(n-methylaniline) vs. polyaniline: An extended ph range of polaron stability as revealed by raman spectroelectrochemistry. *Spectrochim. Acta, Part A*, 262:120140, 2021.

[52] Trinh Thi Nguyen, Hien Thi Thu Khuat, Shinya Asakura, Goro Mizutani, Yoshitaka Murakami, and Takashi Okada. Study of the molecular orientation of steroidal side chains at polyimide surfaces using sum frequency generation vibrational spectroscopy. *J. Chem. Phys.*, 155(8):084702, 2021.

[53] Weiduo Wang, Huayi Li, Qian Li, and Zhi Luo. A novel grafted polyethylene with diphenyl phosphoryl group: Improved flame retardancy and favorable compatibility. *J. Appl. Polym. Sci.*, 138(42):51242, 2021.

[54] Jonas Delabie, Julien De Winter, Olivier Deschaume, Carmen Bartic, Pascal Gerbaux, Thierry Verbiest, and Guy Koeckelberghs. Development of a layered hybrid nanocomposite material using α,ω-bifunctionalized polythiophenes. *Macromolecules*, 53(24):11098–11105, 2020.

[55] Julia Gerber, Tobias Lendenmann, Hadi Eghlidi, Thomas M Schutzius, and Dimos Poulikakos. Wetting transitions in droplet drying on soft materials. *Nat. Commun.*, 10(1):1–10, 2019.

[56] D. K. Owens and R. C. Wendt. Estimation of the surface free energy of polymers. *J. Appl. Polym. Sci.*, 13(8):1741–1747, 1969.

[57] Robert J. Good and L. A. Girifalco. A theory for estimation of surface and interfacial energies. iii. estimation of surface energies of solids from contact angle data. *J. Phys. Chem.*, 64(5):561–565, 1960.

[58] L. A. Girifalco and R. J. Good. A theory for the estimation of surface and interfacial energies. i. derivation and application to interfacial tension. *J. Phys. Chem.*, 61(7):904–909, 1957.

[59] E. M. Rossi, P. Sudharshan Phani, R. Guillemet, Julie Cholet, Doriane Jussey, W. C. Oliver, and M. Sebastiani. A novel nanoindentation protocol to characterize surface free energy of superhydrophobic nanopatterned materials. *Journal of Materials Research*, 36(11):2357–2370, jun 2021.

[60] Beth S Guiton, Morgan Stefik, Veronica Augustyn, Sarbajit Banerjee, Christopher J Bardeen, Bart M Bartlett, Jun Li, Vilmalí López-Mejías, Leonard R MacGillivray, Amanda Morris, et al. Frontiers in hybrid and interfacial materials chemistry research. *MRS Bull.*, 45(11):951–964, 2020.

[61] Tak-Sing Wong, Taolei Sun, Lin Feng, and Joanna Aizenberg. Interfacial materials with special wettability. *MRS Bull.*, 38(5):366–371, 2013.

[62] Markus J Buehler. Materials by design – a perspective from atoms to structures. *MRS Bull.*, 38(2):169–176, 2013.

[63] Daniel Bonn, Jens Eggers, Joseph Indekeu, Jacques Meunier, and Etienne Rolley. Wetting and spreading. *Rev. Mod. Phys.*, 81:739–805, May 2009.

[64] Petter Johansson and Berk Hess. Molecular origin of contact line friction in dynamic wetting. *Phys. Rev. Fluids*, 3:074201, Jul 2018.

[65] Petter Johansson, Andreas Carlson, and Berk Hess. Water–substrate physicochemistry in wetting dynamics. *J. Fluid Mech.*, 781:695–711, 2015.

[66] Frédéric Leroy and Florian Müller-Plathe. Dry-surface simulation method for the determination of the work of adhesion of solid–liquid interfaces. *Langmuir*, 31(30):8335–8345, 2015.

[67] Frédéric Leroy, Shengyuan Liu, and Jianguo Zhang. Parametrizing nonbonded interactions from wetting experiments via the work of adhesion: Example of water on graphene surfaces. *J. Phys. Chem. C*, 119(51):28470–28481, 2015.

[68] Leili Zhang, Binquan Luan, and Ruhong Zhou. Parameterization of molybdenum disulfide interacting with water using the free energy perturbation method. *J. Phys. Chem. B*, 123(34):7243–7252, 2019.

[69] Ananth Govind Rajan, Michael S. Strano, and Daniel Blankschtein. Liquids with lower wettability can exhibit higher friction on hexagonal boron nitride: The intriguing role of solid–liquid electrostatic interactions. *Nano Lett.*, 19(3):1539–1551, 2019.

[70] Annalisa Cardellini, Francesco Maria Bellussi, Edoardo Rossi, Lorenzo Chiavarini, Claude Becker, David Cant, Pietro Asinari, and Marco Sebastiani. Integrated molecular dynamics and experimental approach to characterize low-free-energy perfluoro-decyl-acrylate (pfda) coated silicon. *Mater. Des.*, 208:109902, 2021.

[71] Hamzeh Yaghoubi and Masumeh Foroutan. Molecular investigation of the wettability of rough surfaces using molecular dynamics simulation. *Phys. Chem. Chem. Phys.*, 20:22308–22319, 2018.

[72] Hamzeh Yaghoubi and Masumeh Foroutan. Wettability of striped patterned mono-and multilayer graphene supported on platinum. *Appl. Surf. Sci.*, 500:144002, 2020.

[73] Takahiro Koishi, Kenji Yasuoka, Shigenori Fujikawa, and Xiao Cheng Zeng. Measurement of contact-angle hysteresis for droplets on nanopillared surface and in the cassie and wenzel states: A molecular dynamics simulation study. *ACS Nano*, 5(9):6834–6842, 2011.

[74] Vishnu Sresht, Ananth Govind Rajan, Emilie Bordes, Michael S. Strano, Agílio A.H. Pádua, and Daniel Blankschtein. Quantitative modeling of mos2–solvent interfaces: Predicting contact angles and exfoliation performance using molecular dynamics. *J. Phys. Chem. C*, 121(16):9022–9031, 2017.

[75] Kostya S Novoselov, Andre K Geim, Sergei V Morozov, De-eng Jiang, Yanshui Zhang, Sergey V Dubonos, Irina V Grigorieva, and Alexandr A Firsov. Electric field effect in atomically thin carbon films. *science*, 306(5696):666–669, 2004.

[76] Kostya S Novoselov, Andre K Geim, Sergei Vladimirovich Morozov, Dingde Jiang, Michail I Katsnelson, Irina V Grigorieva, SVb Dubonos, and andAA Firsov. Two-dimensional gas of massless dirac fermions in graphene. *nature*, 438(7065):197–200, 2005.

[77] Fatemeh Farjadian, Somayeh Abbaspour, Mohamad Amin Abdolahi Sadatlu, Soroush Mirkiani, Amir Ghasemi, Mojtaba Hoseini-Ghahfarokhi, Naeimeh Mozaffari, Mahdi Karimi, and Michael R Hamblin. Recent developments in graphene and graphene oxide: Properties, synthesis, and modifications: A review. *ChemistrySelect*, 5(33):10200–10219, 2020.

[78] Frank Schwierz. Graphene transistors. *Nature nanotechnology*, 5(7):487–496, 2010.

[79] Beibei Zhan, Chen Li, Jun Yang, Gareth Jenkins, Wei Huang, and Xiaochen Dong. Graphene field-effect transistor and its application for electronic sensing. *Small*, 10(20):4042–4065, 2014.

[80] Jiacheng Wei, Thuc Vo, and Fawad Inam. Epoxy/graphene nanocomposites–processing and properties: a review. *Rsc Advances*, 5(90):73510–73524, 2015.

[81] Ahsan Mehmood, NM Mubarak, Mohammad Khalid, Rashmi Walvekar, EC Abdullah, MTH Siddiqui, Humair Ahmed Baloch, Sabzoi Nizamuddin, and Shaukat Mazari. Graphene based nanomaterials for strain sensor application—a review. *Journal of Environmental Chemical Engineering*, 8(3):103743, 2020.

[82] Haixin Chang and Hongkai Wu. Graphene-based nanocomposites: preparation, functionalization, and energy and environmental applications. *Energy & Environmental Science*, 6(12):3483–3507, 2013.

[83] Abdul Ghani Olabi, Mohammad Ali Abdelkareem, Tabbi Wilberforce, and Enas Taha Sayed. Application of graphene in energy storage device–a review. *Renewable and Sustainable Energy Reviews*, 135:110026, 2021.

[84] Chen Chen, Lingjie Jia, Jiachen Li, Li Zhang, Lijun Liang, Eryu Chen, Zhe Kong, Xinping Wang, Wei Zhang, and Jia-Wei Shen. Understanding the effect of hydroxyl/epoxy group on water desalination through lamellar graphene oxide membranes via molecular dynamics simulation. *Desalination*, 491:114560, 2020.

[85] Vahid Mortazavi, Ali Moosavi, and Ali Nouri-Borujerdi. Water desalination by charged multilayer graphene membrane: A molecular dynamics simulation. *Journal of Molecular Liquids*, 355:118953, 2022.

[86] Yunhui Wang, Zhongjin He, Krishna M Gupta, Qi Shi, and Ruifeng Lu. Molecular dynamics study on water desalination through functionalized nanoporous graphene. *Carbon*, 116:120–127, 2017.

[87] Liubov A Belyaeva and Grégory F Schneider. Wettability of graphene. *Surface science reports*, 75(2):100482, 2020.

[88] Fereshte Taherian, Valentina Marcon, Nico FA van der Vegt, and Frédéric Leroy. What is the contact angle of water on graphene? *Langmuir*, 29(5):1457–1465, 2013.

[89] Donghwan Kim, Eunchan Kim, Sohyun Park, Seungah Kim, Byoung Koun Min, Hyo Jae Yoon, Kyungwon Kwak, and Minhaeng Cho. Wettability of graphene and interfacial water structure. *Chem*, 7(6):1602–1614, 2021.

[90] Javad Rafiee, Xi Mi, Hemtej Gullapalli, Abhay V Thomas, Fazel Yavari, Yunfeng Shi, Pulickel M Ajayan, and Nikhil A Koratkar. Wetting transparency of graphene. *Nature materials*, 11(3):217–222, 2012.

[91] Jin-You Lu, Tuza Olukan, Srinivasa Reddy Tamalampudi, Abdulrahman Al-Hagri, Chia-Yun Lai, Mariam Ali Al Mahri, Harry Apostoleris, Ibraheem Almansouri, and Matteo Chiesa. Insights into graphene wettability transparency by locally probing its surface free energy. *Nanoscale*, 11(16):7944–7951, 2019.

[92] Bladimir Ramos-Alvarado, Satish Kumar, and GP Peterson. On the wettability transparency of graphene-coated silicon surfaces. *The Journal of chemical physics*, 144(1):014701, 2016.

[93] Christian D van Engers, Nico EA Cousens, Vitaliy Babenko, Jude Britton, Bruno Zappone, Nicole Grobert, and Susan Perkin. Direct measurement of the surface energy of graphene. *Nano letters*, 17(6):3815–3821, 2017.

[94] Xuemei Li, Zhengyang Li, Yuyang Long, Yanshuang He, Baowen Li, Jidong Li, Hu Qiu, Jun Yin, and Wanlin Guo. Wetting stability of supported graphene in ambient environment. *Advanced Engineering Materials*, 24(6):2101283, 2022.

[95] Anna V Prydatko, Liubov A Belyaeva, Lin Jiang, Lia MC Lima, and Grégory F Schneider. Contact angle measurement of free-standing square-millimeter single-layer graphene. *Nature Communications*, 9(1):4185, 2018.

[96] Zhiting Li, Yongjin Wang, Andrew Kozbial, Ganesh Shenoy, Feng Zhou, Rebecca McGinley, Patrick Ireland, Brittni Morganstein, Alyssa Kunkel, Sumedh P Surwade, et al. Effect of airborne contaminants on the wettability of supported graphene and graphite. *Nature materials*, 12(10):925–931, 2013.

[97] T Werder, Jens Honore Walther, RL Jaffe, T Halicioglu, and Petros Koumoutsakos. On the water- carbon interaction for use in molecular dynamics simulations of graphite and carbon nanotubes. *The Journal of Physical Chemistry B*, 107(6):1345–1352, 2003.

[98] S Dong. On imposing dynamic contact-angle boundary conditions for wall-bounded liquid–gas flows. *Computer Methods in Applied Mechanics and Engineering*, 247:179–200, 2012.

[99] Zhen Zhang and Xianmin Xu. Effective boundary conditions for dynamic contact angle hysteresis on chemically inhomogeneous surfaces. *Journal of Fluid Mechanics*, 935:A34, 2022.

[100] Johan Göhl, Andreas Mark, Srdjan Sasic, and Fredrik Edelvik. An immersed boundary based dynamic contact angle framework for handling complex surfaces of mixed wettabilities. *International Journal of Multiphase Flow*, 109:164–177, 2018.

[101] Ziyang Huang, Guang Lin, and Arezoo M Ardekani. Implementing contact angle boundary conditions for second-order phase-field models of wall-bounded multiphase flows. *Journal of Computational Physics*, 471:111619, 2022.

[102] Malcolm E Schrader. Young-dupre revisited. *Langmuir*, 11(9):3585–3589, 1995.

[103] Lasse Makkonen. A thermodynamic model of contact angle hysteresis. *The Journal of chemical physics*, 147(6):064703, 2017.

[104] Terence D Blake. The physics of moving wetting lines. *Journal of colloid and interface science*, 299(1):1–13, 2006.

[105] Arnout MP Boelens and Juan J de Pablo. Generalised navier boundary condition for a volume of fluid approach using a finite-volume method. *Physics of Fluids*, 31(2):021203, 2019.

[106] Thomas E Gartner III and Arthi Jayaraman. Modeling and simulations of polymers: a roadmap. *Macromolecules*, 52(3):755–786, 2019.

[107] Satyen Dhamankar and Michael A Webb. Chemically specific coarse-graining of polymers: methods and prospects. *Journal of Polymer Science*, 59(22):2613–2643, 2021.

[108] Marissa G Saunders and Gregory A Voth. Coarse-graining methods for computational biology. *Annual review of biophysics*, 42:73–93, 2013.

[109] Sebastian Kmiecik, Dominik Gront, Michal Kolinski, Lukasz Wieteska, Aleksandra Elzbieta Dawid, and Andrzej Kolinski. Coarse-grained protein models and their applications. *Chem. Rev.*, 116(14):7898–7936, 2016. PMID: 27333362.

[110] Helgi I. Ingólfsson, Cesar A. Lopez, Jaakko J. Uusitalo, Djurre H. de Jong, Srinivasa M. Gopal, Xavier Periole, and Siewert J. Marrink. The power of coarse graining in biomolecular simulations. *WIREs Comput. Mol. Sci.*, 4(3):225–248, 2014.

[111] Emiliano Brini, Elena A. Algaer, Pritam Ganguly, Chunli Li, Francisco Rodríguez-Ropero, and Nico F. A. van der Vegt. Systematic coarse-graining methods for soft matter simulations a review. *Soft Matter*, 9:2108–2119, 2013.

[112] Soumil Y. Joshi and Sanket A. Deshmukh. A review of advancements in coarse-grained molecular dynamics simulations. *Mol. Simul.*, 0(0):1–18, 2020.

[113] Rajat Srivastava, Matteo Fasano, Shahin Mohammad Nejad, Hernán Chávez Thielemann, Eliodoro Chiavazzo, and Pietro Asinari. Modeling carbon-based smart materials. In Constantinos A. Charitidis, Elias P. Koumoulos, and Dimitrios A. Dragatogiannis, editors, *Carbon-Based Smart Materials*, chapter 3, pages 33–80. De Gruyter, Berlin/Boston, 2020.

[114] Takahiro Yoshizawa, Ken Uchibori, Mitsugu Araki, Shigeyuki Matsumoto, Biao Ma, Ryo Kanada, Yosuke Seto, Tomoko Oh-hara, Sumie Koike, Ryo Ariyasu, Satoru Kitazono, Hironori Ninomiya, Kengo Takeuchi, Noriko

Yanagitani, Satoshi Takagi, Kazuma Kishi, Naoya Fujita, Yasushi Okuno, Makoto Nishio, and Ryohei Katayama. Microsecond-timescale md simulation of egfr minor mutation predicts the structural flexibility of egfr kinase core that reflects egfr inhibitor sensitivity. *npj Precis. Onc.*, 5(1):32, 2021.

[115] Taylor R. Quinn, Calvin N. Steussy, Brandon E. Haines, Jinping Lei, Wei Wang, Fu Kit Sheong, Cynthia V. Stauffacher, Xuhui Huang, Per-Ola Norrby, Paul Helquist, and Olaf Wiest. Microsecond timescale md simulations at the transition state of pmhmgr predict remote allosteric residues. *Chem. Sci.*, 12:6413–6418, 2021.

[116] Sebastian Kmiecik, Dominik Gront, Michal Kolinski, Lukasz Wieteska, Aleksandra Elzbieta Dawid, and Andrzej Kolinski. Coarse-grained protein models and their applications. *Chemical reviews*, 116(14):7898–7936, 2016.

[117] Soumil Y Joshi and Sanket A Deshmukh. A review of advancements in coarse-grained molecular dynamics simulations. *Molecular Simulation*, 47(10-11):786–803, 2021.

[118] Siewert J. Marrink, H. Jelger Risselada, Serge Yefimov, D. Peter Tieleman, and Alex H. de Vries. The martini force field: Coarse grained model for biomolecular simulations. *J. Phys. Chem. B*, 111(27):7812–7824, 2007. PMID: 17569554.

[119] Siewert J Marrink, Alex H De Vries, and Alan E Mark. Coarse grained model for semiquantitative lipid simulations. *The Journal of Physical Chemistry B*, 108(2):750–760, 2004.

[120] Djurre H de Jong, Gurpreet Singh, WF Drew Bennett, Clement Arnarez, Tsjerk A Wassenaar, Lars V Schafer, Xavier Periole, D Peter Tieleman, and Siewert J Marrink. Improved parameters for the martini coarse-grained protein force field. *Journal of chemical theory and computation*, 9(1):687–697, 2013.

[121] Semen O. Yesylevskyy, Lars V. SchÃ¤fer, Durba Sengupta, and Siewert J. Marrink. Polarizable water model for the coarse-grained martini force field. *PLoS Comput. Biol.*, 6(6):1–17, 06 2010.

[122] Riccardo Alessandri, Fabian Grünewald, and Siewert J Marrink. The martini model in materials science. *Advanced Materials*, 33(24):2008635, 2021.

[123] Mario Orsi. Comparative assessment of the elba coarse-grained model for water. *Mol. Phys.*, 112(11):1566–1576, 2014.

[124] Sereina Riniker and Wilfred F. van Gunsteren. A simple, efficient polarizable coarse-grained water model for molecular dynamics simulations. *J. Chem. Phys.*, 134(8):084110, 2011.

[125] Zhe Wu, Qiang Cui, and Arun Yethiraj. A new coarse-grained model for water: The importance of electrostatic interactions. *J. Phys. Chem. B*, 114(32):10524–10529, 2010. PMID: 20701383.

[126] William George Noid. Perspective: Coarse-grained models for biomolecular systems. *The Journal of chemical physics*, 139(9):09B201_1, 2013.

[127] Huilin Ye, Weikang Xian, and Ying Li. Machine learning of coarse-grained models for organic molecules and polymers: Progress, opportunities, and challenges. *ACS omega*, 6(3):1758–1772, 2021.

[128] Kévin Kempfer, Julien Devemy, Alain Dequidt, Marc Couty, and Patrice Malfreyt. Development of coarse-grained models for polymers by trajectory matching. *ACS omega*, 4(3):5955–5967, 2019.

[129] Hwankyu Lee, Alex H de Vries, Siewert-Jan Marrink, and Richard W Pastor. A coarse-grained model for polyethylene oxide and polyethylene glycol: conformation and hydrodynamics. *The journal of physical chemistry B*, 113(40):13186–13194, 2009.

[130] Jiang Wang, Simon Olsson, Christoph Wehmeyer, Adrià Pérez, Nicholas E Charron, Gianni De Fabritiis, Frank Noé, and Cecilia Clementi. Machine learning of coarse-grained molecular dynamics force fields. *ACS central science*, 5(5):755–767, 2019.

[131] Patrick G Sahrmann, Timothy D Loose, Aleksander EP Durumeric, and Gregory A Voth. Utilizing machine learning to greatly expand the range and accuracy of bottom-up coarse-grained models through virtual particles. *Journal of Chemical Theory and Computation*, 2023.

[132] Henry Chan, Mathew J Cherukara, Badri Narayanan, Troy D Loeffler, Chris Benmore, Stephen K Gray, and Subramanian KRS Sankaranarayanan. Machine learning coarse grained models for water. *Nature communications*, 10(1):379, 2019.

[133] Paraskevi Gkeka, Gabriel Stoltz, Amir Barati Farimani, Zineb Belkacemi, Michele Ceriotti, John D Chodera, Aaron R Dinner, Andrew L Ferguson, Jean-Bernard Maillet, Hervé Minoux, et al. Machine learning force fields and coarse-grained variables in molecular dynamics: application to materials and biological systems. *Journal of chemical theory and computation*, 16(8):4757–4775, 2020.

[134] Gerardo Andres Cisneros, Kjartan Thor Wikfeldt, Lars Ojamae, Jibao Lu, Yao Xu, Hedieh Torabifard, Albert P. Bartok, Gabor Csanyi, Valeria Molinero, and Francesco Paesani. Modeling molecular interactions in water: From pairwise to many-body potential energy functions. *Chem. Rev.*, 116(13):7501–7528, 2016. PMID: 27186804.

[135] Aidan P Thompson, H Metin Aktulga, Richard Berger, Dan S Bolintineanu, W Michael Brown, Paul S Crozier, Pieter J in't Veld, Axel Kohlmeyer, Stan G Moore, Trung Dac Nguyen, et al. Lammps-a flexible simulation tool for particle-based materials modeling at the atomic, meso, and continuum scales. *Computer Physics Communications*, 271:108171, 2022.

[136] Trung Dac Nguyen and Steven J Plimpton. Aspherical particle models for molecular dynamics simulation. *Computer Physics Communications*, 243:12–24, 2019.

[137] Andrew I. Jewett, David Stelter, Jason Lambert, Shyam M. Saladi, Otello M. Roscioni, Matteo Ricci, Ludovic Autin, Martina Maritan, Saeed M. Bashusqeh, Tom Keyes, Remus T. Dame, Joan-Emma Shea, Grant J. Jensen, and David S. Goodsell. Moltemplate: A tool for coarse-grained modeling of complex biological matter and soft condensed matter physics. *J. Mol. Biol.*, page 166841, 2021.

[138] Matteo Ricci, Otello Maria Roscioni, Lara Querciagrossa, and Claudio Zannoni. Molc. a reversible coarse grained approach using anisotropic beads for the modelling of organic functional materials. *Phys. Chem. Chem. Phys.*, 21:26195–26211, 2019.

[139] Alexander E Cohen, Nicholas E Jackson, and Juan J De Pablo. Anisotropic coarse-grained model for conjugated polymers: Investigations into solution morphologies. *Macromolecules*, 54(8):3780–3789, 2021.

[140] Hujun Shen, Yan Li, Pengyu Ren, Dinglin Zhang, and Guohui Li. Anisotropic coarse-grained model for proteins based on gay–berne and electric multipole potentials. *Journal of chemical theory and computation*, 10(2):731–750, 2014.

[141] Jibao Lu, Yuqing Qiu, Riccardo Baron, and Valeria Molinero. Coarse-graining of tip4p/2005, tip4p-ew, spc/e, and tip3p to monatomic anisotropic water models using relative entropy minimization. *J. Chem. Theory Comput.*, 10(9):4104–4120, 2014. PMID: 26588552.

[142] Jaehyeok Jin, Yining Han, Alexander J. Pak, and Gregory A. Voth. A new one-site coarse-grained model for water: Bottom-up many-body projected water (bumper). i. general theory and model. *J. Chem. Phys.*, 154(4):044104, 2021.

[143] Kristyna Pluhackova and Rainer A. Backmann. Biomembranes in atomistic and coarse-grained simulations. *J. Phys.: Condens. Matter*, 27(32):323103, jul 2015.

[144] W. M. Brown, M. K. Petersen, S. J. Plimpton, and G. S. Grest. Liquid crystal nanodroplets in solution. *J. Chem. Phys.*, 130:044901, 2009.

[145] Lewis Fry Richardson and Richard Tetley Glazebrook. Ix. the approximate arithmetical solution by finite differences of physical problems involving differential equations, with an application to the stresses in a masonry dam. *Philos. Trans. Roy. Soc. London A*, 210(459-470):307–357, 1911.

[146] Henrik Bruus. *Theoretical microfluidics*, volume 18. Oxford university press, 2007.

[147] Andrea Cavalli. Wetting on micro-structured surfaces: modelling and optimization. 2013.

[148] J Zhang. Work of adhesion and work of cohesion. *Encyclopedia of Tribology; Wang, QJ, Chung, Y.-W., Eds*, pages 4127–4132, 2013.

[149] Alphonsus V Pocius and David A Dillard. *Adhesion science and engineering: surfaces, chemistry and applications*. Elsevier, 2002.

[150] Rawesh Kumar. *Surface Characterization Techniques: From Theory to Research*. Walter de Gruyter GmbH & Co KG, 2022.

[151] Jörgen Bergström. Experimental characterization techniques. *Mechanics of Solid Polymers*, pages 19–114, 2015.

[152] Tommi Huhtamäki, Xuelin Tian, Juuso T Korhonen, and Robin HA Ras. Surface-wetting characterization using contact-angle measurements. *Nature protocols*, 13(7):1521–1538, 2018.

[153] Bastian E Rapp. *Microfluidics: modeling, mechanics and mathematics*. Elsevier, 2022.

[154] Sreya Sarkar, Mohamad Jafari Gukeh, Tamal Roy, Harshad Gaikwad, Francesco Maria Bellussi, Shashwata Moitra, and Constantine M Megaridis. A new methodology for measuring solid/liquid interfacial energy. *Journal of Colloid and Interface Science*, 633:800–807, 2023.

[155] Graham Hodgson, Martin Passmore, Maciej Skarysz, Andrew Garmory, and Franck Paolillo. Contact angle measurements for automotive exterior water management. *Experiments in Fluids*, 62(5):119, 2021.

[156] Suprakas Sinha Ray. 3–structure and morphology characterization techniques. *Clay-containing polymer nanocomposites*, pages 39–66, 2013.

[157] John C Lindon, George E Tranter, and David Koppenaal. *Encyclopedia of spectroscopy and spectrometry*. Academic Press, 2016.

[158] Neil K Adam and Gilbert Jessop. Ccl.angles of contact and polarity of solid surfaces. *J. Chem. Soc., Trans.*, 127:1863–1868, 1925.

[159] Robert J Good. A thermodynamic derivation of wenzel's modification of young's equation for contact angles; together with a theory of hysteresis1. *J. Am. Chem. Soc.*, 74(20):5041–5042, 1952.

[160] MA González. Force fields and molecular dynamics simulations. *École thématique de la Société Française de la Neutronique*, 12:169–200, 2011.

[161] Alex D MacKerell Jr, Donald Bashford, MLDR Bellott, Roland Leslie Dunbrack Jr, Jeffrey D Evanseck, Martin J Field, Stefan Fischer, Jiali Gao, H Guo, Sookhee Ha, et al. All-atom empirical potential for molecular modeling and dynamics studies of proteins. *The journal of physical chemistry B*, 102(18):3586–3616, 1998.

[162] Chris Oostenbrink, Alessandra Villa, Alan E Mark, and Wilfred F Van Gunsteren. A biomolecular force field based on the free enthalpy of hydration and solvation: the gromos force-field parameter sets 53a5 and 53a6. *Journal of computational chemistry*, 25(13):1656–1676, 2004.

[163] Wendy D Cornell, Piotr Cieplak, Christopher I Bayly, Ian R Gould, Kenneth M Merz, David M Ferguson, David C Spellmeyer, Thomas Fox, James W Caldwell, and Peter A Kollman. A second generation force field for the simulation of proteins, nucleic acids, and organic molecules. *Journal of the American Chemical Society*, 117(19):5179–5197, 1995.

[164] Shirley W. I. Siu, Kristyna Pluhackova, and Rainer A. Böckmann. Optimization of the opls-aa force field for long hydrocarbons. *J. Chem. Theory Comput.*, 8(4):1459–1470, 2012.

[165] Huai Sun. Compass: an ab initio force-field optimized for condensed-phase applications overview with details on alkane and benzene compounds. *The Journal of Physical Chemistry B*, 102(38):7338–7364, 1998.

[166] Anthony K Rappé, Carla J Casewit, KS Colwell, William A Goddard III, and W Mason Skiff. Uff, a full periodic table force field for molecular mechanics and molecular dynamics simulations. *Journal of the American chemical society*, 114(25):10024–10035, 1992.

[167] Stephen L Mayo, Barry D Olafson, and William A Goddard. Dreiding: a generic force field for molecular simulations. *Journal of Physical chemistry*, 94(26):8897–8909, 1990.

[168] Devleena Shivakumar, Joshua Williams, Yujie Wu, Wolfgang Damm, John Shelley, and Woody Sherman. Prediction of absolute solvation free energies using molecular dynamics free energy perturbation and the opls force field. *Journal of chemical theory and computation*, 6(5):1509–1519, 2010.

[169] Mark E. Tuckerman. *Statistical mechanics theory and molecular simulation*. Oxford graduate texts. Oxford University Press, New York, 2010.

[170] Thomas C Beutler, Alan E Mark, René C van Schaik, Paul R Gerber, and Wilfred F Van Gunsteren. Avoiding singularities and numerical instabilities in free energy calculations based on molecular simulations. *Chemical physics letters*, 222(6):529–539, 1994.

[171] JG Gay and BJ Berne. Modification of the overlap potential to mimic a linear site–site potential. *The Journal of Chemical Physics*, 74(6):3316–3319, 1981.

[172] Roberto Berardi, C Fava, and Claudio Zannoni. A generalized gay-berne intermolecular potential for biaxial particles. *Chemical physics letters*, 236(4-5):462–468, 1995.

[173] Roberto Berardi, Carlo Fava, and Claudio Zannoni. A gay–berne potential for dissimilar biaxial particles. *Chemical physics letters*, 297(1-2):8–14, 1998.

[174] Roger W Hockney and James W Eastwood. *Computer simulation using particles*. crc Press, 2021.

[175] Lammps molecular dynamics simulator. https://www.lammps.org.

[176] Steve Plimpton. Fast parallel algorithms for short-range molecular dynamics. *J. Comput. Phys.*, 117(1):1–19, 1995.

[177] User-molc package is available on github. https://github.com/matteoeghirotta/lammps-30Oct19.

[178] Xue Shen Wu and Nuo Wang. Synthesis, characterization, biodegradation, and drug delivery application of biodegradable lactic/glycolic acid polymers. part ii: Biodegradation. *J. Biomater. Sci., Polym. Ed.*, 12(1):21–34, 2001.

[179] Marianne Parent, Cécile Nouvel, Martin Koerber, Anne Sapin, Philippe Maincent, and Ariane Boudier. Plga in situ implants formed by phase inversion: Critical physicochemical parameters to modulate drug release. *J. Controlled Release*, 172(1):292–304, 2013.

[180] Hirenkumar K. Makadia and Steven J. Siegel. Poly lactic-co-glycolic acid (plga) as biodegradable controlled drug delivery carrier. *Polymers*, 3(3):1377–1397, 2011.

[181] Yihan Xu, Donghun Koo, Emily A. Gerstein, and Chang-Soo Kim. Multiscale modeling of polymer–drug interactions and their impact on the structural evolutions in plga-tetracycline films. *Polymer*, 84:121–131, 2016.

[182] Kemei Pei, Yidai Ying, and Chihchang Chu. Molecular dynamic simulations of a new family of synthetic biodegradable amino acid-based poly(ester amide) biomaterials: Glass transition temperature and adhesion behavior. *Mater. Today Chem.*, 4:90–96, 2017.

[183] Martina Pannuzzo, Bruno A. C. Horta, Carmelo La Rosa, and Paolo Decuzzi. Predicting the miscibility and rigidity of poly(lactic-co-glycolic acid)/polyethylene glycol blends via molecular dynamics simulations. *Macromolecules*, 53(10):3643–3654, 2020.

[184] James Andrews and Estela Blaisten-Barojas. Exploring with molecular dynamics the structural fate of plga oligomers in various solvents. *J. Phys. Chem. B*, 123(48):10233–10244, 2019.

[185] Marcus D Hanwell, Donald E Curtis, David C Lonie, Tim Vandermeersch, Eva Zurek, and Geoffrey R Hutchison. Avogadro: an advanced semantic chemical editor, visualization, and analysis platform. *J. Cheminf.*, 4(1):1–17, 2012.

[186] Avogadro: an open-source molecular builder and visualization tool. version 1.xx. http://avogadro.cc/.

[187] J. L. F. Abascal and C. Vega. A general purpose model for the condensed phases of water: Tip4p/2005. *J. Chem. Phys.*, 123(23):234505, 2005.

[188] H. J. C. Berendsen, J. R. Grigera, and T. P. Straatsma. The missing term in effective pair potentials. *J. Phys. Chem.*, 91(24):6269–6271, 1987.

[189] In-Chul Yeh and Max L. Berkowitz. Ewald summation for systems with slab geometry. *J. Chem. Phys.*, 111(7):3155–3162, 1999.

[190] Jmol: an open-source java viewer for chemical structures in 3d. http://www.jmol.org/.

[191] Paolo Cignoni, Marco Callieri, Massimiliano Corsini, Matteo Dellepiane, Fabio Ganovelli, and Guido Ranzuglia. MeshLab: an Open-Source Mesh Processing Tool. In Vittorio Scarano, Rosario De Chiara, and Ugo Erra, editors, *Eurographics Italian Chapter Conference*. The Eurographics Association.

[192] David Nečas and Petr Klapetek. Gwyddion: an open-source software for SPM data analysis. *Cent. Eur. J. Phys.*, 10:181–188, 2012.

[193] John G. Kirkwood and Frank P. Buff. The statistical mechanical theory of surface tension. *J. Chem. Phys.*, 17(3):338–343, 1949.

[194] Francesco Maria Bellussi, Otello Maria Roscioni, Annalisa Cardellini, Marina Provenzano, and Matteo Fasano. Wettability of soft PLGA surfaces predicted by experimentally-augmented atomistic models, June 2022.

[195] Chemical & physical properties of select polymers. https://www.absorbables.com/technical/properties/.

[196] Piergiorgio Gentile, Valeria Chiono, Irene Carmagnola, and Paul V. Hatton. An overview of poly(lactic-co-glycolic) acid (plga)-based biomaterials for bone tissue engineering. *Int. J. Mol. Sci.*, 15(3):3640–3659, 2014.

[197] Dana L Sedin and Kathy L Rowlen. Influence of tip size on AFM roughness measurements. *Applied Surface Science*, 182(1):40–48, 2001.

[198] Deepak N Kapoor, Amit Bhatia, Ripandeep Kaur, Ruchi Sharma, Gurvinder Kaur, and Sanju Dhawan. Plga: a unique polymer for drug delivery. *Therapeutic delivery*, 6(1):41–58, 2015.

[199] James Andrews, Robert A. Handler, and Estela Blaisten-Barojas. Structure, energetics and thermodynamics of plga condensed phases from molecular dynamics. *Polymer*, 206:122903, 2020.

[200] Ali Khodayari, Matteo Fasano, Masoud Bozorg Bigdeli, Shahin Mohammadnejad, Eliodoro Chiavazzo, and Pietro Asinari. Effect of interfacial thermal resistance and nanolayer on estimates of effective thermal conductivity of nanofluids. *Case Stud. Therm. Eng.*, 12:454–461, 2018.

[201] de la Luz A Perez, Mendez-Maldonado G Arlette, E Nunez-Rojas, F Bresme, and J Alejandre. A new force field of formamide and the effect of the dielectric constant on miscibility. *J. Chem. Theory Comput.*, 11:2792–2800, 2015.

[202] Carl Caleman, Paul J. van Maaren, Minyan Hong, Jochen S. Hub, Luciano T. Costa, and David van der Spoel. Force field benchmark of organic liquids: Density, enthalpy of vaporization, heat capacities, surface tension, isothermal compressibility, volumetric expansion coefficient, and dielectric constant. *J. Chem. Theory Comput.*, 8(1):61–74, 2012.

[203] Rafael A. Zubillaga, Ariana Labastida, Bibiana Cruz, Juan Carlos Martínez, Enrique Sánchez, and José Alejandre. Surface tension of organic liquids using the opls/aa force field. *J. Chem. Theory Comput.*, 9(3):1611–1615, 2013.

[204] C. Vega and E. de Miguel. Surface tension of the most popular models of water by using the test-area simulation method. *J. Chem. Phys.*, 126(15):154707, 2007.

[205] Dortmund data bank. surface tension of hexane. http://www.ddbst.com/en/EED/PCP/SFT_C89.php.

[206] Yong Chae Jung and Bharat Bhushan. Contact angle, adhesion and friction properties of micro-and nanopatterned polymers for superhydrophobicity. *Nanotechnology*, 17(19):4970–4980, 2006.

[207] T. T. Chau, W. J. Bruckard, P. T.L. Koh, and A. V. Nguyen. A review of factors that affect contact angle and implications for flotation practice. *Adv. Colloid Interface Sci.*, 150(2):106–115, sep 2009.

[208] Dortmund data bank. density of hexane. http://www.ddbst.com/en/EED/PCP/DEN_C89.php.

[209] Zongrui Zhang, Xinyu Wang, Rong Zhu, Yiyu Wang, Binbin Li, Yanxu Ma, and Yixia Yin. Synthesis and characterization of serial random and block-copolymers based on lactide and glycolide. *Polym. Sci., Ser. B*, 58:720–729, 11 2016.

[210] Wilfred F. van Gunsteren, Xavier Daura, Niels Hansen, Alan E. Mark, Chris Oostenbrink, Sereina Riniker, and Lorna J. Smith. Validation of molecular simulation: An overview of issues. *Angew. Chem. Int. Ed.*, 57(4):884–902, 2018.

[211] Guo Hong-Kai and Fang Hai-Ping. Drop size dependence of the contact angle of nanodroplets. *Chin. Phys. Lett.*, 22(4):787, 2005.

[212] Jun Zhang, Matthew K Borg, Khellil Sefiane, and Jason M Reese. Wetting and evaporation of salt-water nanodroplets: A molecular dynamics investigation. *Phys. Rev. E*, 92(5):052403, 2015.

[213] Md Masuduzzaman and BoHung Kim. Effects of dissimilar molecular interface and ion-concentration on wetting characteristics of nanodroplets. *Microfluid. Nanofluid.*, 25(6):1–14, 2021.

[214] Suryoday Prodhan, Jing Qiu, Matteo Ricci, Otello M. Roscioni, Linjun Wang, and David Beljonne. Design rules to maximize charge-carrier mobility along conjugated polymer chains. *J. Phys. Chem. Lett.*, 11(16):6519–6525, 2020.

[215] H. Gokberk Ozcelik, Ezgi Satiroglu, and Murat Barisik. Size dependent influence of contact line pinning on wetting of nano-textured/patterned silica surfaces. *Nanoscale*, 12(41):21376–21391, oct 2020.

[216] European Committee for Standardization. CEN Workshop Agreement CWA 17284: Materials modelling - Terminology, classification and metadata, 2018. https://emmc.info/wp-content/uploads/2018/05/CWA_17284.pdf.

[217] European Committee for Standardization. CEN Workshop Agreement CWA 17815: Materials characterisation - Terminology, metadata and classification, 2021. https://www.cencenelec.eu/media/CEN-CENELEC/CWAs/ICT/cwa17815.pdf.

[218] New feature compute fep/ta. https://github.com/lammps/lammps/pull/3192.

[219] Yujie Wu, Harald L Tepper, and Gregory A Voth. Flexible simple point-charge water model with improved liquid-state properties. *The Journal of chemical physics*, 124(2):024503, 2006.

[220] William Humphrey, Andrew Dalke, and Klaus Schulten. Vmd: visual molecular dynamics. *Journal of Molecular Graphics*, 14(1):33–38, 1996.

[221] Guy J Gloor, George Jackson, Felipe J Blas, and Enrique de Miguel. Test-area simulation method for the direct determination of the interfacial tension of systems with continuous or discontinuous potentials. *The Journal of chemical physics*, 123(13):134703, 2005.

[222] Anjan R Nair and Sarith P Sathian. A molecular dynamics study to determine the solid-liquid interfacial tension using test area simulation method (tasm). *The Journal of Chemical Physics*, 137(8):084702, 2012.

[223] Erich A Muller, Åsmund Ervik, and Andrés Mejía. A guide to computing interfacial properties of fluids from molecular simulations [article v1. 0]. *Living Journal of Computational Molecular Science*, 2(1):21385–21385, 2020.

[224] Frédéric Leroy and Florian Muller-Plathe. Dry-surface simulation method for the determination of the work of adhesion of solid–liquid interfaces. *Langmuir*, 31(30):8335–8345, 2015.

[225] Ruifei Wang, Jin Chai, Bobo Luo, Xiong Liu, Jianting Zhang, Min Wu, Mingdan Wei, and Zhuanyue Ma. A review on slip boundary conditions at the nanoscale: recent development and applications. *Beilstein Journal of Nanotechnology*, 12(1):1237–1251, 2021.

[226] David Parobek and Haitao Liu. Wettability of graphene. *2D Materials*, 2(3):032001, 2015.

[227] Rishi Raj, Shalabh C Maroo, and Evelyn N Wang. Wettability of graphene. *Nano letters*, 13(4):1509–1515, 2013.

[228] Jacob N Israelachvili. *Intermolecular and surface forces*. Academic press, 2011.

[229] Gabriele Tocci, Laurent Joly, and Angelos Michaelides. Friction of water on graphene and hexagonal boron nitride from ab initio methods: very different slippage despite very similar interface structures. *Nano letters*, 14(12):6872–6877, 2014.

[230] Jean-Paul Ryckaert, Giovanni Ciccotti, and Herman J.C Berendsen. Numerical integration of the cartesian equations of motion of a system with constraints: molecular dynamics of n-alkanes. *J. Comput. Phys.*, 23(3):327–341, 1977.

[231] Hans C Andersen. Rattle: A velocity version of the shake algorithm for molecular dynamics calculations. *J. Comput. Phys.*, 52(1):24–34, 1983.

[232] Backmap: an open-source program to reverse map coarse-grained trajectories to atomic coordinates. https://github.com/matteoeghirotta/backmap_legacy.

[233] Daniel J. Price and Charles L. Brooks 3rd. A modified tip3p water potential for simulation with ewald summation. *J. Chem. Phys.*, 121:10096–103, 2004.

[234] Miguel Angel González and José L. F. Abascal. The shear viscosity of rigid water models. *J. Chem. Phys.*, 132(9):096101, 2010.

[235] Gabriela Guevara-Carrion, Jadran Vrabec, and Hans Hasse. Prediction of self-diffusion coefficient and shear viscosity of water and its binary mixtures with methanol and ethanol by molecular simulation. *J. Chem. Phys.*, 134(7):074508, 2011.

[236] Yong Zhang, Akihito Otani, and Edward J. Maginn. Reliable viscosity calculation from equilibrium molecular dynamics simulations: A time decomposition method. *J. Chem. Theory Comput.*, 11(8):3537–3546, 2015. PMID: 26574439.

[237] GUANG-JUN GUO and YI-GANG ZHANG. Equilibrium molecular dynamics calculation of the bulk viscosity of liquid water. *Mol. Phys.*, 99(4):283–289, 2001.

[238] Ioannis N. Tsimpanogiannis, Othonas A. Moultos, Luís F. M. Franco, Marcelle B. de M. Spera, Máté Erd os, and Ioannis G. Economou. Self-diffusion coefficient of bulk and confined water: a critical review of classical molecular simulation studies. *Mol. Simul.*, 45(4-5):425–453, 2019.

[239] C. Vega, J. L. F. Abascal, M. M. Conde, and J. L. Aragones. What ice can teach us about water interactions: a critical comparison of the performance of different water models. *Faraday Discuss.*, 141:251–276, 2009.

[240] Junmei Wang and Tingjun Hou. Application of molecular dynamics simulations in molecular property prediction. 1. density and heat of vaporization. *J. Chem. Theory Comput.*, 7(7):2151–2165, 2011. PMID: 21857814.

[241] In-Chul Yeh and Gerhard Hummer. System-size dependence of diffusion coefficients and viscosities from molecular dynamics simulations with periodic boundary conditions. *J. Phys. Chem. B*, 108(40):15873–15879, 2004.

[242] M.P. Allen and D.J. Tildesley. *Computer Simulation of Liquids*. Oxford: Clarendon Pr, 1987.

[243] Manfred Holz, Stefan R. Heil, and Antonio Sacco. Temperature-dependent self-diffusion coefficients of water and six selected molecular liquids for calibration in accurate 1h nmr pfg measurements. *Phys. Chem. Chem. Phys.*, 2:4740–4742, 2000.

[244] N. B. Vargaftik, B. N. Volkov, and L. D. Voljak. International tables of the surface tension of water. *J. Phys. Chem. Ref. Data*, 12(3):817–820, 1983.

[245] Jibao Lu, Charusita Chakravarty, and Valeria Molinero. Relationship between the line of density anomaly and the lines of melting, crystallization, cavitation, and liquid spinodal in coarse-grained water models. *J. Chem. Phys.*, 144(23):234507, 2016.

[246] Carlos Vega and Jose L. F. Abascal. Simulating water with rigid non-polarizable models: a general perspective. *Phys. Chem. Chem. Phys.*, 13:19663–19688, 2011.

[247] Levi C.T. Pierce, Romelia Salomon-Ferrer, Cesar Augusto F. de Oliveira, J. Andrew McCammon, and Ross C. Walker. Routine access to millisecond time scale events with accelerated molecular dynamics. *J. Chem. Theory Comput.*, 8(9):2997–3002, 2012. PMID: 22984356.

[248] Jordi Juárez-Jiménez, Arun A. Gupta, Gogulan Karunanithy, Antonia S. J. S. Mey, Charis Georgiou, Harris Ioannidis, Alessio De Simone, Paul N. Barlow, Alison N. Hulme, Malcolm D. Walkinshaw, Andrew J. Baldwin, and Julien Michel. Dynamic design: manipulation of millisecond timescale motions on the energy landscape of cyclophilin a. *Chem. Sci.*, 11:2670–2680, 2020.

[249] Mario Orsi and Jonathan W. Essex. The elba force field for coarse-grain modeling of lipid membranes. *PLoS One*, 6(12):1–22, 12 2011.

[250] Victor Cruces Chamorro, Carmelo Tempra, and Pavel Jungwirth. Heavy water models for classical molecular dynamics: Effective inclusion of nuclear quantum effects. *J. Phys. Chem. B*, 125(17):4514–4519, 2021. PMID: 33904303.

[251] Xibing He, Wataru Shinoda, Russell DeVane, and Michael L. Klein. Exploring the utility of coarse-grained water models for computational studies of interfacial systems. *Mol. Phys.*, 108(15):2007–2020, 2010.

[252] Min Li, WenCai Lu, and John ZengHui Zhang. A three-point coarse-grained model of five-water cluster with permanent dipoles and quadrupoles. *Phys. Chem. Chem. Phys.*, 22:26289–26298, 2020.

[253] Min Li, WenCai Lu, and John ZengHui Zhang. Ultra-coarse-graining modeling of liquid water. *J. Chem. Phys.*, 154(22):224506, 2021.

[254] S Goossens, David Seveno, R Rioboo, A Vaillant, J Conti, and J De Coninck. Can we predict the spreading of a two-liquid system from the spreading of the corresponding liquid–air systems? *Langmuir*, 27(16):9866–9872, 2011.

[255] Matteo Fasano, Gabriele Falciani, Vincenza Brancato, Valeria Palomba, Pietro Asinari, Eliodoro Chiavazzo, and Andrea Frazzica. Atomistic modelling of water transport and adsorption mechanisms in silicoaluminophosphate for thermal energy storage. *Appl. Therm. Eng.*, 160:114075, 2019.

[256] E. Chiavazzo, M. Fasano, P. Asinari, and P. Decuzzi. Scaling behaviour for the water transport in nanoconfined geometries. *Nat. Commun.*, 3565, 2014.

[257] Anna Sofia Tascini, Jeff Armstrong, Eliodoro Chiavazzo, Matteo Fasano, Pietro Asinari, and Fernando Bresme. Thermal transport across nanoparticle–fluid interfaces: the interplay of interfacial curvature and nanoparticle–fluid interactions. *Phys. Chem. Chem. Phys.*, 19(4):3244–3253, 2017.

[258] Sumith Yd and Shalabh C Maroo. Surface-heating algorithm for water at nanoscale. *J. Phys. Chem. Lett.*, 6(18):3765–3769, 2015.

[259] Mark James Abraham, Teemu Murtola, Roland Schulz, Szilárd Páll, Jeremy C Smith, Berk Hess, and Erik Lindahl. Gromacs: High performance molecular simulations through multi-level parallelism from laptops to supercomputers. *SoftwareX*, 1:19–25, 2015.

[260] James C Phillips, David J Hardy, Julio DC Maia, John E Stone, João V Ribeiro, Rafael C Bernardi, Ronak Buch, Giacomo Fiorin, Jérôme Hénin, Wei Jiang, et al. Scalable molecular dynamics on cpu and gpu architectures with namd. *The Journal of chemical physics*, 153(4), 2020.

[261] Amber 2023 reference manual. http://ambermd.org/doc12/Amber23.pdf.

[262] Peter Wirnsberger, Daniel Frenkel, and C Dellago. An enhanced version of the heat exchange algorithm with excellent energy conservation properties. *The Journal of chemical physics*, 143(12):124104, 2015.

[263] SM Lebedev, OS Gefle, ET Amitov, D Yu Berchuk, and DV Zhuravlev. Poly (lactic acid)-based polymer composites with high electric and thermal conductivity and their characterization. *Polymer Testing*, 58:241–248, 2017.

[264] Rui Guo, Zechun Ren, Hongjie Bi, Min Xu, and Liping Cai. Electrical and thermal conductivity of polylactic acid (pla)-based biocomposites by incorporation of nano-graphite fabricated with fused deposition modeling. *Polymers*, 11(3):549, 2019.

[265] Florian Müller-Plathe. A simple nonequilibrium molecular dynamics method for calculating the thermal conductivity. *The Journal of chemical physics*, 106(14):6082–6085, 1997.

[266] Behzad Damadzadeh, Hamideh Jabari, Mikael Skrifvars, Karri Airola, Niko Moritz, and Pekka K Vallittu. Effect of ceramic filler content on the mechanical and thermal behaviour of poly-l-lactic acid and poly-l-lactic-co-glycolic acid composites for medical applications. *Journal of Materials Science: Materials in Medicine*, 21:2523–2531, 2010.

[267] Ville Liimatainen, Maja Vuckovac, Ville Jokinen, Veikko Sariola, Matti J Hokkanen, Quan Zhou, and Robin HA Ras. Mapping microscale wetting variations on biological and synthetic water-repellent surfaces. *Nature communications*, 8(1):1798, 2017.

[268] Samantha Sbarra, Louis Waquier, Stephan Suffit, Aristide Lemaître, and Ivan Favero. Optomechanical measurement of single nanodroplet evaporation with millisecond time-resolution. *Nature Communications*, 13(1):6462, 2022.

[269] Alberto Giacomello, Simone Meloni, Mauro Chinappi, and Carlo Massimo Casciola. Cassie–baxter and wenzel states on a nanostructured surface: phase diagram, metastabilities, and transition mechanism by atomistic free energy calculations. *Langmuir*, 28(29):10764–10772, 2012.

[270] Enhancing lammps capabilities enhancing lammps capabilities. https://www.lammps.org/workshops/Aug11/Kloss/kloss_abq_2011_final.pdf.

[271] Overview of the atoms-to-continuum package for lammps. https://www.lammps.org/workshops/Aug11/Templeton/Templeton_LWS.pdf.